TOPICAL REVIEW • OPEN ACCESS

Interfacing quantum emitters with propagating surface acoustic waves

To cite this article: Matthias Weiß and Hubert J Krenner 2018 *J. Phys. D: Appl. Phys.* **51** 373001

OPEN ACCESS
IOP Publishing
Journal of Physics D: Applied Physics
J. Phys. D: Appl. Phys. **51** (2018) 373001 (33pp)
https://doi.org/10.1088/1361-6463/aace3c

Topical Review

Interfacing quantum emitters with propagating surface acoustic waves

Matthias Weiß[1,2] **and Hubert J Krenner**[1,2,3]

[1] Lehrstuhl für Experimentalphysik 1 and Augsburg Centre for Innovative Technologies (ACIT), Universität Augsburg, Universitätsstraße 1, 86159 Augsburg, Germany
[2] Nanosystems Initiative Munich (NIM), Schellingstraße 4, 80339 München, Germany
[3] Center for Nanoscience (CeNS), Ludwig-Maximilians-Universität München, Geschwister-Scholl-Platz 1, 80539 München, Germany

E-mail: hubert.krenner@physik.uni-augsburg.de

Received 19 March 2018, revised 24 May 2018
Accepted for publication 21 June 2018
Published 2 August 2018

Abstract

In this topical review, we report on recent advances on the coupling of single semiconductor quantum emitters, quantum dots, to the dynamic strain and electric fields of surface acoustic waves. Quantum dots are atom-like optically addressable two-level systems embedded in semiconductor matrices. On the one hand, the occupancy states of these 'artificial atoms' can be programmed by spatio-temporal carrier dynamics driven by sound waves. On the other hand, the quantized energy levels of electrons and holes couple strongly to the mechanical strain of these waves. We present an overview of the fundamental coupling mechanisms, experimental techniques to probe these systems in the time domain, and recent hallmark experiments. We discuss emerging research themes including hybrid architectures comprising advanced $LiNbO_3$ SAW devices and single quantum dot devices of nanowire-based quantum emitters, and sound-driven control of light–matter interaction between single photons in nanophotonic resonators and two-level quantum dot systems.

Keywords: surface acoustic waves, quantum dots, optomechanics, phononics, elastic waves

(Some figures may appear in colour only in the online journal)

1. Introduction

Today, physicists control a broad variety of quantum states with unprecedented precision [1–5]. However, no individual, isolated approach on its own meets all the stringent criteria for application in future quantum technologies. Hybrid quantum systems aim to combine the complementary strengths of diverse systems, while at the same time avoiding their individual shortcomings [6]. For the realization of hybrid quantum architectures, dynamic mechanical excitations exhibit two unique advantages: (i) they interact strongly with literally any other quantum system [7–10] and most excitingly, (ii) they can be routed in the form of a surface acoustic wave (SAW) over millimeter distances with extremely low dissipation. These surface confined acoustic modes are of the highest technological importance and the major phononic technology of industrial relevance. Engineers have perfected SAW devices over recent decades [11–13], and microacoustic devices constitute an integral part of the backbone of wireless communication at radio frequencies. Such a mature technological platform is also highly desirable for fundamental research, because it provides highly optimized and advanced devices ready for hybridization with exploratory classical or quantum mechanical systems.

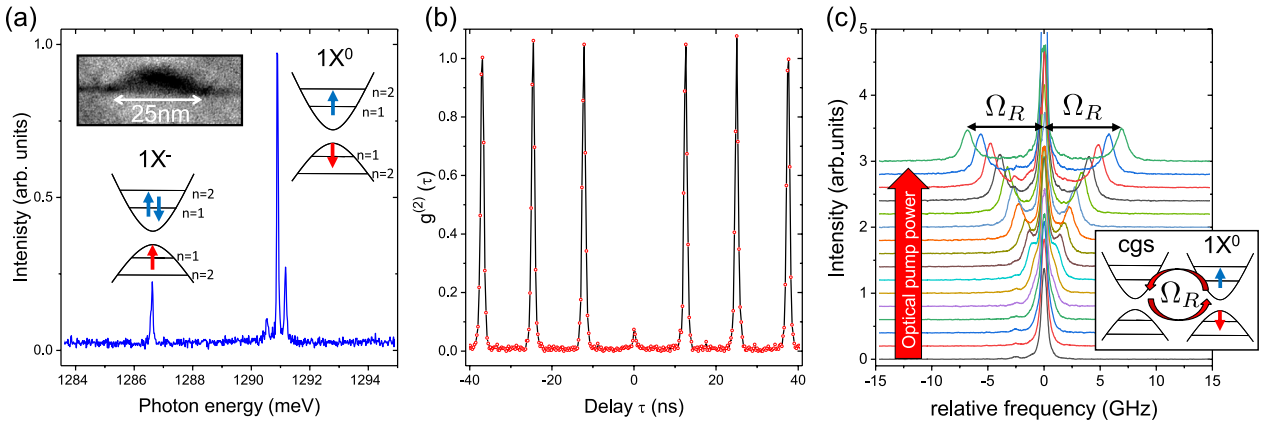

Figure 1. Single QDs. (a) Emission spectrum of a single In(Ga)As QD under non-resonant optical transition. In the spectrum, sharp emission lines can be identified and attributed to the recombination of different excitonic configurations. Inset: TEM image of a single In(Ga)As QD. (b) Second order autocorrelation function $g^{(2)}(\tau)$ of the excitonic emission of a single QD. Photon anti-bunching, the suppression of coincidence counts at $\tau = 0$, is a characteristic fingerprint of single photon emission. (c) Emission of a single resonantly driven QD as a function of optical pump power. The resonant optical drive induces Rabi oscillations between the upper ($1X^0$) and lower level (cgs) of the optically active QD two-level-system. The Rabi oscillations of the dressed states manifest as the splitting in the observed Mollow-Triplet.

In this Topical Review, we review recent advances in the dynamic control of optically active quantum emitters by SAWs. We focus in particular on quantum dots (QDs) in compound semiconductors, which can be addressed by near infrared light. The concepts reviewed here also apply to other types of quantum emitter, in particular nitrogen vacancy centers in diamond, which have been interfaced with SAWs in recent experiments [14, 15]. Electrostatic QDs, formed for instance by electrically gating 2D electron systems, are not in the scope of this Topical Review, and the reader is referred to recent key publications and review articles [16–24].

2. Optically active quantum dots

Semiconductor QDs are the semiconductor realization of a particle in a box. In these nanostructures, the motion of carriers is confined in all three spatial directions. This gives rise to a discrete energy spectrum and thus density of electronic states. Moreover, electrons and holes are confined to the small volume of the dot; their mutual few-particle interactions strongly depend on the number of confined electrons and holes. Consequently, each occupancy state exhibits a well-defined and distinct energy. These properties are fully analogous to the energy level scheme of atoms, and QDs are therefore often referred to as 'artificial atoms'. This analogy is most striking for optically active QDs: here, few-particle interactions of excitons lead to discrete, narrow linewidth optical transitions [25]. For a comprehensive introduction to the fundamentals of optically active QDs, the reader is referred to [26].

2.1. Properties of optically active quantum dots

To date, QDs have been realized via a broad variety of approaches using semiconductor heteroepitaxy. The most widely studied highly optically active QD system comprises self-assembled QDs grown in the so-called Stranski–Krastanov growth mode of semiconductor epitaxy in the In(Ga)As material system [27]. These QDs realize nearly ideal optically active two-level systems in a solid. Figure 1(a) shows the photoluminescence (PL) emission spectrum of a single In(Ga)As QD embedded in a GaAs matrix. The spectrum consists of discrete emission lines which can be attributed to distinct occupancy states. The dominant emission line stems from the recombination of the neutral single exciton $1X^0$ formed by one electron and one hole confined in the QD. In this convention, MX^k, M denotes the number of electron–hole pairs and k the excess charge. Just adding a single electron to the QD shifts the optical transition and the emission of the negatively charged trion ($1X^{1-}$) consisting of two electrons and one hole, is detected to be shifted approximately 5 meV to lower energies. This shift corresponds to approximately 1000 times the linewidth of these transitions, emphasizing the highly nonlinear optical properties of the system. Because each excitonic occupancy state exhibits a well-defined and distinct energy, the recombination process reflects this discrete nature and light is emitted as single photons. This quantum light emission can be verified experimentally by measuring the second order correlation function $g^{(2)}(\tau)$ in a Hanbury Brown and Twiss experiment [28]. Figure 1(b) shows the measured $g^{(2)}(\tau)$ of a single periodically pumped QD. Clearly, $g^{(2)}(0) \approx 0$, proving a close to ideal single photon emission [29, 30]. In recent experiments, the single photon emission of single QDs has been dramatically improved using optical microcavities and resonant optical excitation. High-purity emission of single and indistinguishable photons has been reported [31–34] using devices which can outperform alternative sources.

Since each occupancy state of the QD can be optically addressed via its discrete and unique transition energy, resonant spectroscopy can be performed. One example of an optically addressable two-level system is shown as an inset in figure 1(c). It is formed by the crystal ground state of the QD (cgs) and the neutral exciton $1X^0$. This two-level system is the fundamental excitation of the QD. As indicated in the schematic, it undergoes Rabi oscillations when excited

by a resonant laser. These Rabi oscillations have first been observed under pulsed excitation [35, 36] as Rabi flops, and excitonic two-level systems have been controlled fully coherently in subsequent experiments by sequences of laser pulses [37–40]. Later, employing resonant excitation by continuous wave (cw) lasers, optically dressed states have been detected in absorption via the Autler–Townes splitting [41, 42] or in resonant fluorescence as the Mollow triplet [43–46]. The latter is shown in figure 1(c): the emission spectra of a single QD exciton transition filtered by a tunable etalon are plotted against resonant optical excitation power increasing from bottom to top spectra. The frequency of the detected photons is given relative to that of the resonant laser. As the optical pump power increases, the emission splits into the three characteristic lines of the Mollow triplet, which are separated by the Rabi frequency, Ω_R.

Epitaxial QDs exhibit numerous beneficial properties. Since these QDs are grown using semiconductor epitaxy, their integration in advanced devices is very feasible. First of all, QDs can be embedded in electrically active diode or field effect devices. This enables a large number of applications, such as the control of the dot's occupancy state via Coulomb blockade [47, 48] or excitonic transitions via the quantum confined Stark effect (QCSE) [49]. From the doped contacts, carriers can be injected for the read out of spins [50] or to electrically generate single [51] or entangled pairs of photons [52, 53]. These devices can be also operated as photodetectors, which in turn enables photocurrent spectroscopy of excitons [36, 54, 55] or spins [56, 57]. Furthermore, the strain-driven nature of the Stranski–Krastanov growth modes allows the creation of vertically aligned pairs of QDs [58] forming an 'artificial molecule' [59]. These QD-molecules can again be controlled by static electric fields to control their exciton and spin states [60–65]. In parallel, laterally ordered structures have been realized to deterministically control the nucleation site of the QDs [66–68] or to couple adjacent QDs [69–71].

Finally, QDs can be embedded in tailored photonic environments. The engineered photonic density of states allows enhancement or suppression of the radiative recombination via the Purcell effect [72, 73], and single photon operations, even in the strong coupling regime of quantum electrodynamics, have been reported [74–77].

2.2. Quantum dot-phonon coupling

The investigation of the coupling of single QDs to phonons has a long-standing tradition. Probably the most prominent example is the so-called phonon bottleneck, which was predicted before the first experiments on optically active QDs were conducted [78, 79]. The discrete energy levels of a QD were expected to lead to a low relaxation rate of carriers into the electronic groundstate, thus significantly limiting the performance of QD-optoelectronic devices—in particular, lasers [80]. Experiments, however, showed that the phonon bottleneck is typically lifted [81–84] due to a finite yet sufficient coupling to acoustic phonons or alternative relaxation pathways and clear evidence of a phonon bottleneck was obtained under selected conditions [85–89].

In the solid state, phonons are also known as an important source of decoherence. In QDs, dephasing of excitons due to phonons has been widely studied [90–92] and strategies have been implemented to employ phonons in advanced coherent operations [93–95], even replacing microwave photons in the emerging fields of quantum acoustodynamics and quantum acoustics [96–99]. Phonons additionally couple to the spin degree of freedom, also inducing relaxation and dephasing [50, 100–102]. In picosecond acoustics, broadband pulses of gigahertz–terahertz phonons can control solid-state materials and nanosystems [103–107], including the modulation of QD lasers [108, 109].

2.3. SAW interacting with semiconductor QDs

Elastic waves propagating on the surface of a solid were first investigated by Lord Rayleigh [110] is his seminal work on seismic waves. The SAWs in focus here are one particular surface confined elastic mode, referred to as the Rayleigh wave. Typical phase velocities of Rayleigh SAWs are approximately $c_{SAW} \approx 2000$–$5000\,\mathrm{m\,s^{-1}}$. This speed of propagation, five orders of magnitude slower than that of electromagnetic radiation (light), enables the integration of radio frequency devices on a chip. This property is precisely employed in a myriad of SAW and microacoustic devices.

In figure 2, the results of finite element modelling (FEM) of the main characteristics of a Rayleigh-type SAW propagating along the [1 1 0] crystal direction (x) of a (0 0 1)-oriented GaAs surface (z) are presented. We evaluate the main mechanical (left panel) and electrical (right panel) characteristics of the SAW as a function of position, given in units of the SAW wavelength (λ_{SAW}). All mechanical and electrical characteristics scale linearly with the amplitude of the SAW. Therefore, all extracted quantities are normalized to a fixed SAW amplitude (or maximum vertical displacement at the surface) of $A_z = u_{z,max}|_{z=0} = 1\,\mathrm{nm}$. A_z can be determined, for instance, by means of optical interferometry [111], and the measured absolute value can be used to quantify the SAW's characteristics.

The color code of the mechanical wave displacement profile u_x and u_z (left main panel) is the local hydrostatic pressure given by

$$p\,(x,z) = -E_Y\left(\frac{\partial u_x}{\partial x} + \frac{\partial u_z}{\partial z}\right). \qquad (1)$$

Since the hydrostatic pressure is connected to the strain, i.e. the derivative of the displacement, it additionally scales linearly with the frequency of the SAW. Thus, the extracted values of $p\,(x,z)$ are normalized to a frequency of $f_{SAW} = 1\,\mathrm{GHz}$.

In the lower panel, the normalized longitudinal (u_x, black line) and transverse (u_z, red line) displacements and the resulting hydrostatic pressure (blue line) are evaluated along the propagation direction. The characteristic elliptical ('rolling') motion of the Rayleigh wave is reflected in the $\pi/2$-phase shift between the two displacements and their different amplitudes. Since Rayleigh waves are surface confined phonon

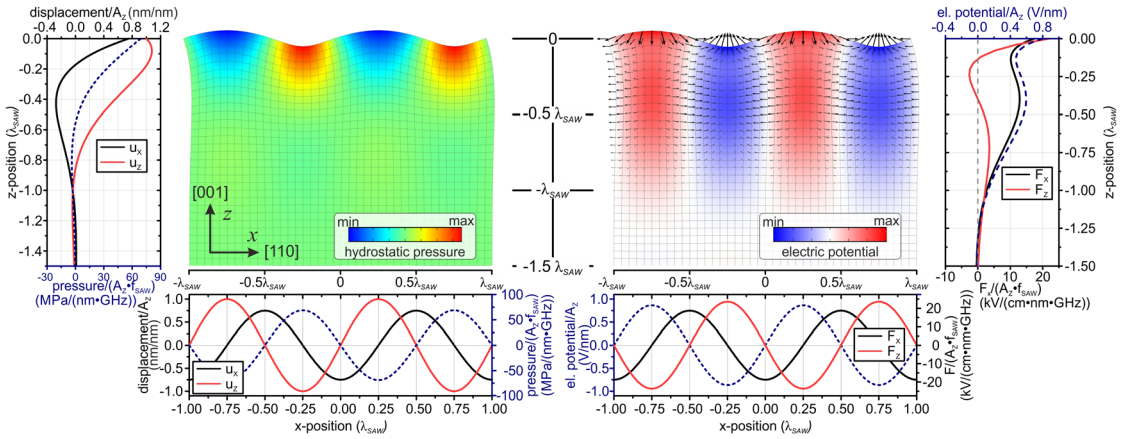

Figure 2. Characteristics of a Rayleigh SAW propagating along the [1 1 0]-direction on a (0 0 1) GaAs surface. Left center panel: displacement (u_x, u_z) profile with the local hydrostatic pressure (p) overlaid as colorscale. Lower left panel: extracted displacement components at the surface u_x (black line) and u_z, (red line), and resulting hydrostatic pressure (p, blue line). Left panel: depth (z)-dependence of the amplitude of u_x (black line), u_z, (red line) and p (blue line). Right center panel: displacement profile with the local electric potential overlaid as colorscale. Lower right panel: extracted electric potential ϕ at the surface (blue line), and resulting transverse $\mathcal{E}_z$, (red line) and longitudinal $\mathcal{E}_x$, (black line) electric field components. Right panel: depth (z)-dependence of the amplitude of ϕ (blue line), $\mathcal{E}_z$, (red line) and $\mathcal{E}_x$ (black line). All given values scale linearly with the SAW amplitude and are normalized to $A_z = 1\,\mathrm{nm}$. In addition, $\mathcal{E}$ and p scale linearly with the SAW frequency and given values are normalized to $f_{SAW} = 1\,\mathrm{GHz}$.

modes, they exhibit a characteristic depth dependence. The results of analogous analyses of the maximum of $u_{x,max}(z)$, $u_{z,max}(z)$ and $p_{max}(z)$ is presented in the left panel. All three quantities rapidly decay into the substrate over a length scale of approximately $0.8 \cdot \lambda_{SAW}$.

GaAs is a piezoelectric, and the considered here [1 1 0]-propagating SAW on a (0 0 1) surface is accompanied by the mechanically induced piezoelectric potential (ϕ). The color code overlaid on the displacement field on the right side of figure 2 is the calculated profile of ϕ. Since this potential is not constant in space and time, a gyrating electric field is induced, which is indicated by arrows in the wave profile. The electric potential (blue line) and transverse ($\mathcal{E}_z$, red line) and longitudinal ($\mathcal{E}_x$, black line) components of the electric field are shown in the right lower panel along the SAW propagation direction. All quantities are again in reference to $A_z = 1\,\mathrm{nm}$ and the electric field component in addition to $f_{SAW} = 1\,\mathrm{GHz}$. The gyrating electric field vector is again nicely reflected in the $\pi/2$-phase shift between the longitudinal and transverse components. The decay of the maximum of these electrical characteristics is shown in the right panel, further confirming the tight surface confinement.

The piezoelectric coupling can be employed to elegantly generate SAWs using so-called interdigital transducers (IDTs). A schematic of a typical sample is shown in figure 3(a). As a radio frequency voltage is applied to the interdigitating comb of electrodes, the material is periodically deformed underneath the fingers. The SAW wavelength, λ_{SAW}, is determined by the periodicity of the IDT as illustrated in the inset. It can be generated simply by applying the correct radio frequency matching the Rayleigh wave dispersion relation $f_{SAW} = c_{SAW}/\lambda_{SAW}$. Since IDTs are patterned by lithographic techniques, typical λ_{SAW} ranges between 100s of nanometers up to several tens of microns. Thus, radio frequencies spanning from 10s of megahertz up to the low gigahertz domain can be achieved.

When interfacing single QDs with these coherent elastic waves, the relative sizes have to be compared. This is illustrated in in figure 3(b). Typical QD size is on the order of 10s of nanometers and thus more than a factor of 10 smaller than typical SAW wavelengths. Therefore, QDs can be considered as point-like objects, and the key characteristics of the SAW coupling to the QD—strain and electric fields—can be assumed to be constant across the volume of the dot.

For a full, comprehensive overview of the elastic and piezoelectric properties of SAWs and electromechanical phenomena, we refer the reader to [107, 112, 113].

3. Methodologies

When probing the coupling of a SAW to QDs (or other types of optically active nanosystems), the optical response can be detected simply with long integration times, averaging over many acoustic cycles. Thus, in such experiments, no temporal information about the SAW-driven processes can be directly deduced. For the direct observation of any SAW-driven process in the time domain, advanced spectroscopic techniques are a key requirement.

Figure 4 illustrates two key techniques employed in experiments presented in the following parts of this Topical Review. For *stroboscopy* shown in figure 4(a), a pulsed laser source is employed and a stable phase relation between the laser pulse (red) and the oscillating SAW field (blue) is established. Under these conditions, the SAW frequency is an integer multiple of the laser repetition rate: $f_{SAW} = n \cdot f_{laser}$. This phase lock ensures that the laser pulses excite the system at a *precisely defined and tunable time during the acoustic cycle*. The signal from the sample is detected and time-integrated as a function of excitation time during the acoustic cycle (i.e. the relative phase between the laser pulse and the electrical signal exciting the SAW). For processes completed after $\lesssim T_{SAW}/4$,

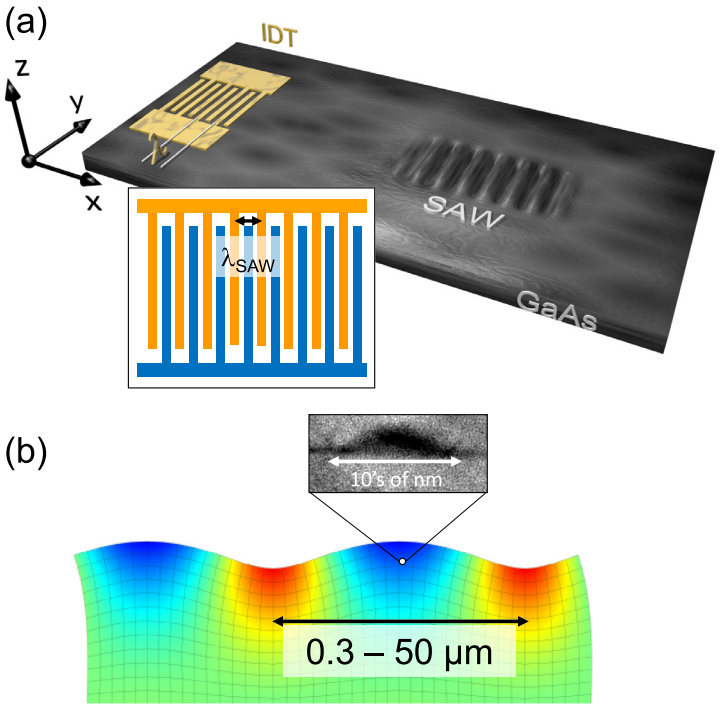

Figure 3. SAW excitation and length scales. (a) Schematic of a SAW-device monolithically defined on a GaAs-based semiconductor heterostructure. A resonant rf voltage applied to the interdigital transducer (IDT) generates the SAW. The lithographically defined periodicity of the IDT determines the wavelength of the generated SAW (inset). (b) Size comparision between SAWs generated using lithographically defined IDTs and a QD. Due to the comparably small size of the QD, the dot can be considered as a point-like object and consequently, the acoustic and electric fields can be assumed to be constant at its position.

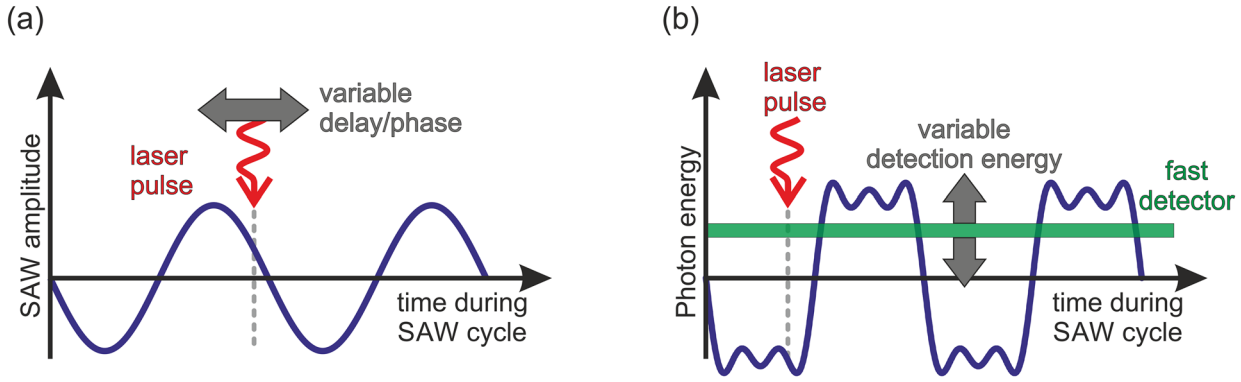

Figure 4. Experimental techniques. (a) In laser-based stroboscopy, the time of the optical excitation during the acoustic cycle is tuned. (b) In phase-locked time-domain spectroscopy, the optical signal is analyzed by fast detectors in the time domain. This technique can be extended to the spectral domain: as shown, for an example of a square wave spectral modulation, tuning the detection energy maps the time-dependent signal as a function of photon energy and time.

stroboscopic spectroscopy faithfully detects the SAW-driven dynamics. This is particularly the case for fast decaying optical signals, for example short decay time emitters. For experiments on low-dimensional semiconductor systems—often pulsed—externally triggered diode lasers, emitting pulses with durations ranging from $\approx$ 50–100 ps can be employed. The electrical pulses triggering the emission of the laser can be elegantly locked to the electrical rf signal generating the SAW [114, 115]. The time during the acoustic cycle can be easily scanned by tuning the relative phase between the two electrical signals. For mode-locked lasers, the fixed repetition rate requires a more elaborate scheme [116–118]. First, precisely designed IDTs are required, which ensure that $f_{SAW} = n \cdot f_{laser}$ can be established. Second, the relative phase between the SAW and the laser pulses has to be tuned by electrical or optical delays. We note that stroboscopic techniques to probe e.g. semiconductors are not limited to laser sources at optical or near-IR wavelengths. These techniques have also been employed for x-ray scattering e.g. using pulsed synchrotron sources to monitor the structural dynamics of crystals and biological membranes induced by SAWs [119–122]. A further recent experiment reported stroboscopic x-ray and photoemission electron microscopy of magnetic nanosystems [123].

For dynamics occurring on timescales comparable to or longer than $\gtrsim T_{SAW}/4$, time-domain detection schemes are imperative. As depicted in figure 4(b), this type of scheme

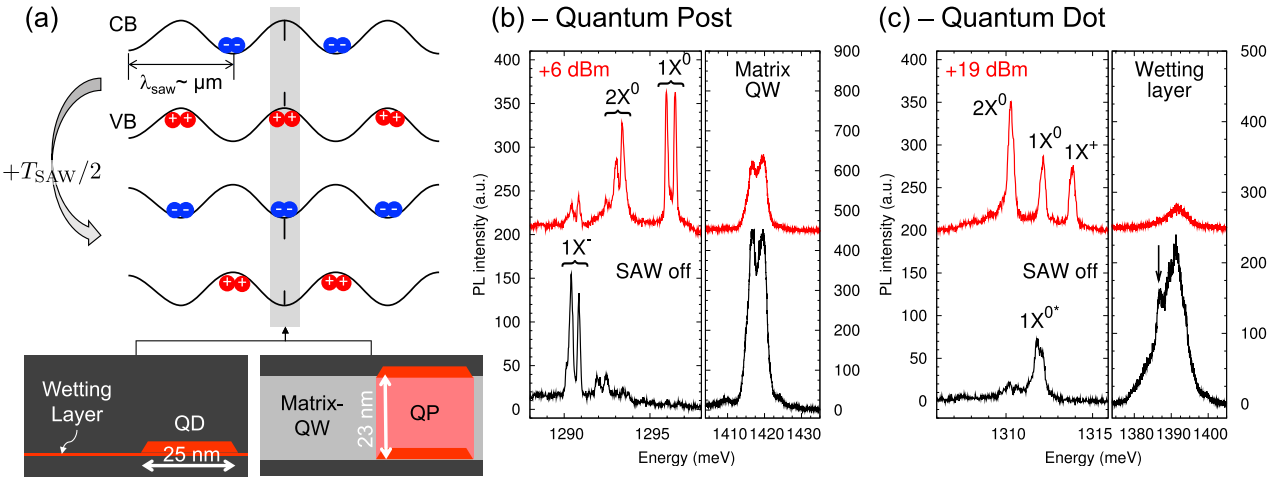

Figure 5. Switching the charge state of a single QD or QP by SAW. (a) The piezoelectric potential of the SAW is superimposed onto the semiconductor's band structure. Self-assembled QDs or columnar QPs are coupled to SAW-modulated 2D systems: a thin wetting layer or thin matrix-QW respectively. Schematics of both types of quantum emitters are shown in the lower part. The resulting type-II band edge modulation leads to a spatial separation of electrons and holes by $\lambda_{SAW}/2$. As shown in the schematic, at one time during the SAW cycle, holes are predominantly present at the position of the QD/QP. The situation is reversed $T_{SAW}/2$, later, after the SAW has propagated by $\lambda_{SAW}/2$. (b), (c) Emission spectra of a single QP and its matrix-QW (b) and a single QD and its wetting layer (c), with (red) and without (black) a SAW applied. Reprinted with permission from [143]. Copyright 2010 American Chemical Society.

again requires a stable phase-locked excitation. The optical signal is then analyzed in the time domain, for instance by time-correlated single photon counting (TCSPC) using fast photodetectors (e.g. single photon counting modules). Time-transients can be acquired as a function of photon energy to monitor the full time and spectral evolutions of the signal [124] as shown for the example of a square wave spectral modulation. Moreover, this scheme can be readily extended to record photon correlations to resolve SAW-modulated modifications of photon statistics [125, 126]. Alternatively, multi-channel detection can be performed using a synchronized streak camera [116, 127]. For processes which are nearly independent of the time of photoexcitation during the acoustic cycles, excitation by cw laser simplifies this scheme and has been performed in several recent works [128–132].

4. Acoustically regulated carrier injection

The impact of a SAW's gyrating piezoelectric fields on carrier dynamics in semiconductors has been studied for several decades: as early as 1996, the acoustoelectric effect was observed in the limit of a single electron in a quantum point contact [133, 134]. This first type of interaction is also the dominant contribution for the control of QDs coupled to a continuum of states in the case of non-resonant generation of charge carriers. In the field of low-dimensional quantum confined semiconductor heterostructures, Rocke *et al* showed in their groundbreaking experiments [135, 136] that photogenerated excitons can be ionized, the electrons and holes thus dissociated being transported by the SAW along its propagation direction in the plane of a quantum well (QW) over distances limited only by the size of the sample. The underlying mechanisms have been the focus of extensive research by Santos *et al* shedding light on the dynamic spatio-temporal charge carrier dynamics induced by the SAW [127, 137–140]. The long-range ambipolar charge carrier transport was recognized by Wiele *et al* in their concept of a precise, acoustically triggered QD-based single photon source [141]—put forward even before single photon emission of single QDs was demonstrated experimentally [28, 142].

4.1. Time integrated and phase-averaged spectroscopy

As shown in figure 5(a), the SAW's piezoelectric potential is superimposed onto the initially flat band structure of the semiconductor. The resulting type-II band edge modulation generates stable points for electrons and holes in the conduction (CB) and valence (VB) bands, respectively. These stability points are spatially separated by approximately $\lambda_{SAW}/2$, which is typically in the range of a few microns. This spatial separation not only leads to the suppression of the optical emission of a QW and long-range ambipolar charge transport as observed by Rocke *et al* [135]. It also dynamically regulates the carrier injection into a QD, which acts as a local deep trap for electrons and holes. Figure 5(a) shows the resulting sequential modulation of the carrier species, which leads to a $T_{SAW}/2$-periodic switching between electrons and holes at the position of the QD. In the lower panel, two types of self-assembled QD systems are introduced: self-assembled QDs, grown in Stranski–Krastanov growth mode [27, 144] and columnar quantum posts (QPs) [145, 146]. Both types of nanostructure can be fabricated in the In(Ga)As material system, and are both established high quality semiconductor single photon emitters [28, 30, 147, 148]. In addition to these self-assembled systems, interface fluctuation, 'natural' QDs on unpatterned [149, 150] or patterned [151] growth substrates, and strain induced QDs [152] have been studied by using SAWs [125, 153]. All four QD systems have in common that they are coupled to a continuous 2D system at higher energies, which acts as the transport channel

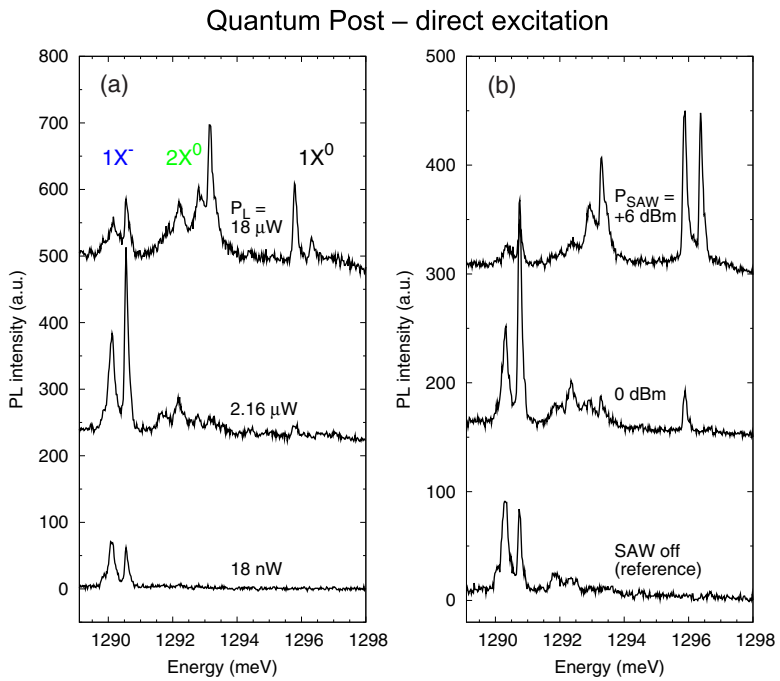

Figure 6. Optical pump power series versus SAW-enhanced carrier capture. (a) Laser power dependent emission of a single Q-Post showing the emergence of biexciton at high pump power. (b) SAW power dependent spectra recorded at low optical pump intensities showing an overall increase of the integrated intensity and switching from charged to neutral exciton complexes at high SAW power. Spectra are offset vertically for clarity. [157] John Wiley & Sons. Copyright © 2012 WILEY-VCH Verlag GmbH & Co. KGaA, Weinheim.

in which the SAW induces spatio-temporal carrier dynamics (STCDs). Because these STCDs are largely dependent on the transport mobility of electrons and holes [139, 154], disorder—particularly thickness fluctuations—in the QW is of pivotal importance. In the case of self-assembled QDs and QPs, these 2D systems differ significantly. The wetting layer on which self-assembled QDs nucleate is a few-monolayer thin, disordered QW highly susceptible to interface fluctuations [155, 156], while the wide matrix QW in which QPs are embedded is only weakly affected by disorder. These largely dissimilar transport properties have a pronounced impact on SAW-regulated carrier injection. Figures 5(b) and (c) compare the emission of a single QP (nominal height $h_{QP} = 23$ nm) and its h_{QP}-wide matrix QW (b) without (black) and with (red) a SAW applied to the emission of a single self-assembled QD and its wetting layer (c) [143]. In both experiments, electrons and holes were photogenerated above the GaAs bandgap, directly at the position of the quantum emitter. Both the matrix QW and the wetting layer exhibit the established quenching behavior [135] as the SAW is switched on and STCDs set in. In strong contrast, QPs and QDs show a largely dissimilar response of their occupancy state to electrons (e) and holes (h). QPs (see figure 5(b)) shows a clean switching from negatively charged excitons $1X^- = 2e + 1h$ to neutral species, exciton $1X^0 = 1e + 1h$ and biexciton $2X^0 = 2e + 2h$. This observation is remarkable, since for random quasi-simultaneous capture of e and h carriers, the QP tends to be occupied by more e than h. Changing the nature of the carrier capture by driving efficient STCDs in the wide QW, charge neutral occupancy states are almost exclusively generated. This means that a QP occupied by n h is more likely to capture n e (and vice versa) only if the SAW provides both carrier species in a highly regulated, periodic manner. Moreover, the formation of a small fraction of biexcitons points to an overall yet moderate increase of the capture efficiency under SAW perturbation.

In contrast, for a self-assembled QD (see figure 5(c)), the neutral exciton $1X^0$ is detected with and without a SAW applied. Strikingly, not only are additional neutral and charged excitons species, $2X^0$ and $1X^+$, observed as a SAW is applied, the overall emission intensity is also greatly increased. This points towards a dramatic enhancement of the overall carrier capture efficiency of a QD when perturbed by a SAW. These observations can be attributed to the abovementioned different carrier transport properties in the 2D systems (matrix QW and wetting layer) in which STCDs are driven by the SAW. While the matrix QW is a near-perfect transport channel, the disordered wetting layer and its large density of trapping sites inhibits efficient STCD. Once the piezoelectric field of the SAW overcomes a critical level, these traps are emptied and the released carriers can be injected into the QD. This effect gives rise to the observed clear overall increase of emission intensity, which is most pronounced for the QD.

This qualitative model is further corroborated in two supporting experiments. Figure 6 compares a series of PL spectra recorded from the same QP. In figure 6(a), the optical excitation power (P_L) is increased. For the two lowest power levels, the spectra are dominated by $1X^-$, consistent with the data in figure 5(b). For the highest power level ($P_L = 18\,\mu$W), the generation of biexcitonic species is favored. In particular, the neutral $2X^0$ is clearly identified and, consequently, $1X^0$ is also detected as this occupancy state is the intermediate level of the

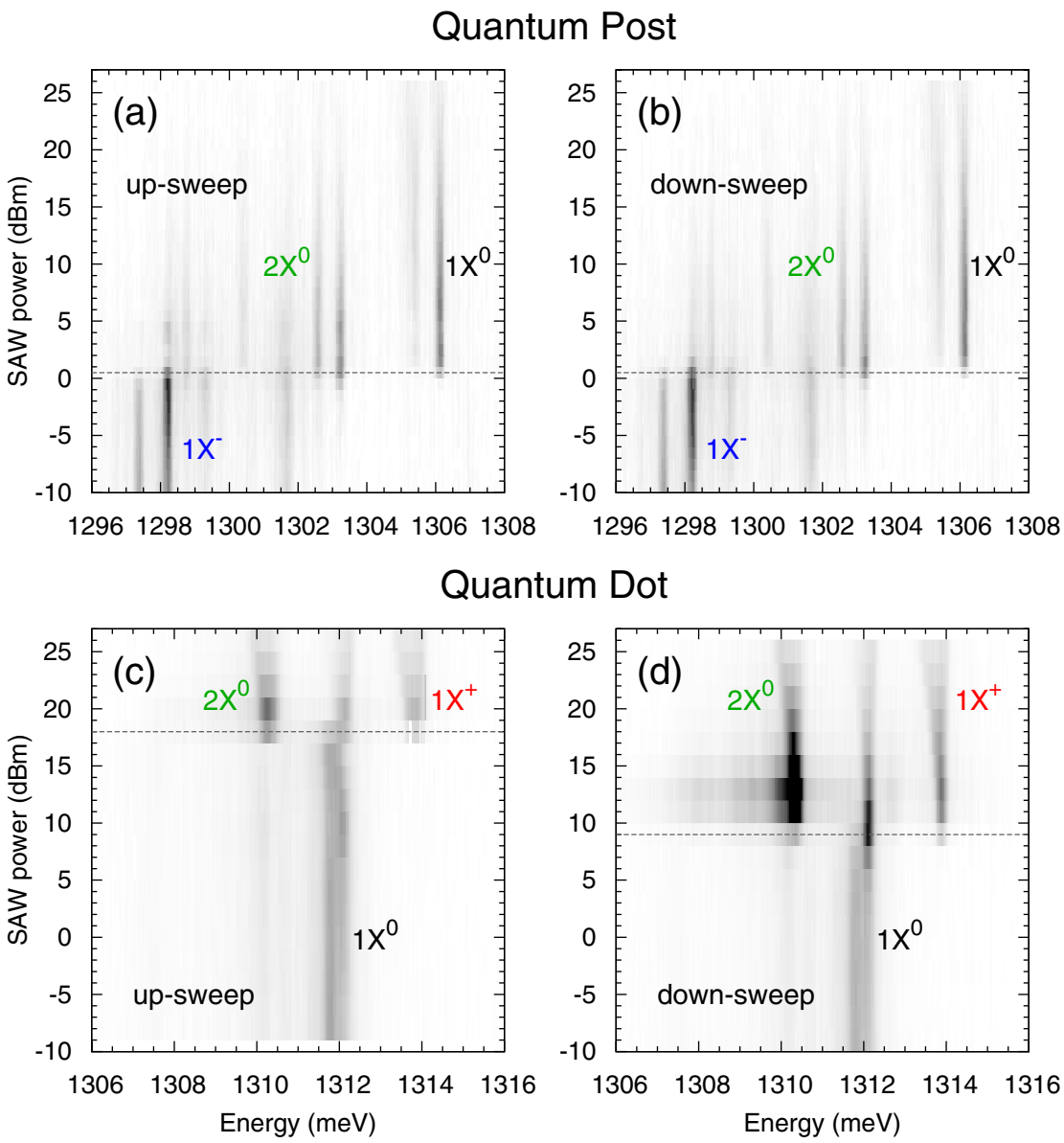

Figure 7. SAW power scans of a single QP (a) and (b) and QD (c) and (d) for increasing (decreasing) P_{SAW}. Both systems show a clear switching at the onset of charge conveyance, which is hysteretic for the QD. [157] John Wiley & Sons. Copyright © 2012 WILEY-VCH Verlag GmbH & Co. KGaA, Weinheim.

biexciton–exciton emission cascade [158–160]. In figure 6(b), $P_L \approx 500\,\mathrm{nW}$ is kept constant and the rf power level generating a SAW is varied. The reference spectrum without SAW perturbation agrees well with the P_L-dependent spectrum in figure 6(a). As the amplitude of the SAW is increased, the emission spectra in (b) exhibit an almost identical evolution as in the optical power series in (a). For the data in (a), the observed increase of the QP occupancy arises from the increase in the photogeneration rate of carriers. For the data in (b), this generation rate is constant; consequently, the observed increase in the QP occupancy is directly related to an increase of the carrier capture efficiency due to the induced STCDs.

In figure 7, we compare the optical emission of the same QP (figures 7(a) and (b)) and a QD (figures 7(c) and (d)) as the rf power applied to the IDT is swept up (figures 7(a) and (c)) and down (figures 7(b) and (d)). The emission intensity is encoded in grayscale with black (white) being high (low) intensity and plotted as a function of photon energy (horizontal axis) and applied rf power (vertical axis). For the QP, the observed evolution of the emission spectrum is almost independent of the sweep direction. A clear switching at precisely the same rf power level $P_{rf} = +0.5\,\mathrm{dBm}$ is observed for both the up- and down-sweep. This indicates that at this power level, the piezoelectric field reaches a critical value, from which point onwards excitons are dissociated and STCDs set in. In contrast, the switching behavior of the QD differs significantly for the up- and downsweep: as P_{rf} is increased, switching occurs at a significantly higher level $P_{rf} = +18\,\mathrm{dBm}$ than for the down-sweep $P_{rf} = +9\,\mathrm{dBm}$. This approximately eight-times higher power level for the up-sweep compared to the downsweep corresponds to a four-fold increase in the critical piezoelectric field inducing STCDs in the wetting layer. In

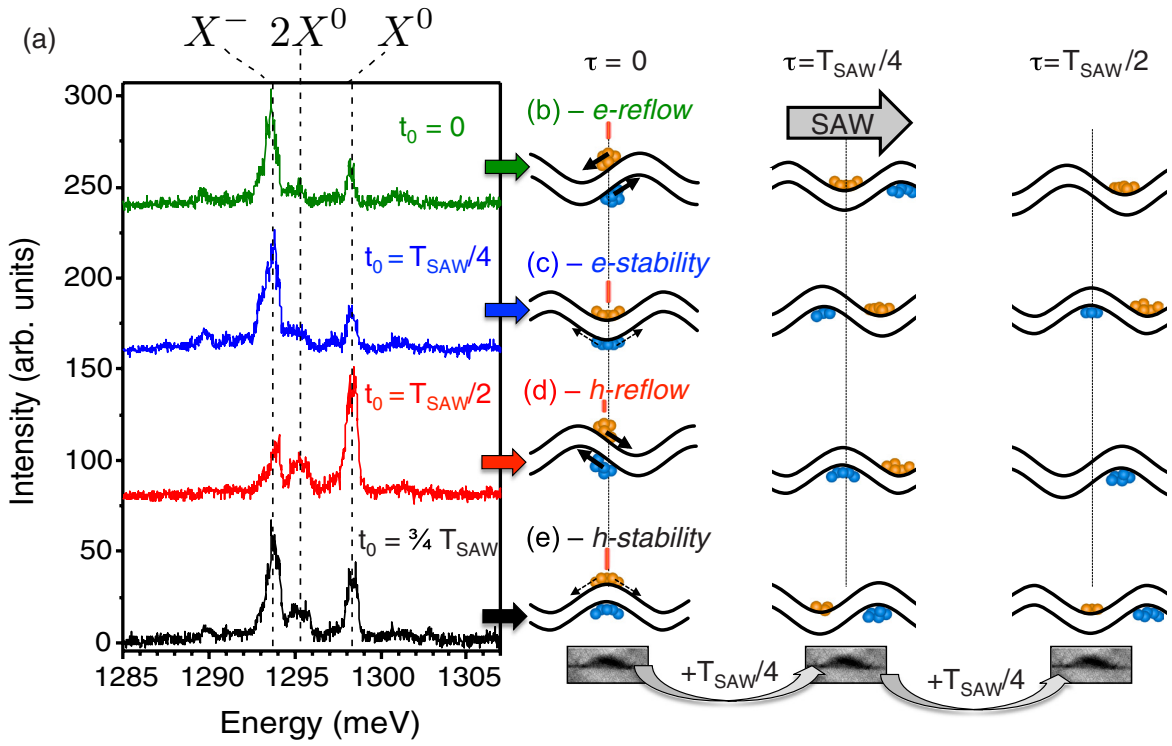

Figure 8. Stroboscopic, time-integrated PL spectra of a single QD (a) when optically generating carriers at four distinct times during the SAW cycle. (b)–(e) Schematic of the corresponding excitation conditions and motion of *e* (orange) and *h* (blue) carriers in the Type-II band edge modulation. The center and right panels show the time evolution in steps of $T_{SAW}/4$ for a SAW propagating from left to right. Reprinted figure with permission from [161], Copyright 2013 by the American Physical Society.

other words, once a large amplitude SAW is applied, STCDs sustain significantly lower electric fields compared to the non-preconditioned case. These experimental findings can be qualitatively understood as a SAW-induced untrapping of localized carriers in the disordered wetting layer. Once these traps are emptied, the lowest lying states, i.e. the QDs, are preferentially capture dissociated carriers. The driving STCDs persist at significantly lower power levels because the stationary charge of localized, trapped carriers does not screen the piezoelectric fields [143].

4.2. Direct observation of SAW-driven occupancy state control of an individual QD

We now switch back to the dynamics of the SAW-driven control of a QD's occupancy state. This effect was studied in detail by Schülein *et al* [161], on a single, isolated self-assembled In(Ga)As QD. In contrast to the previously discussed experiments, charge carriers were selectively photogenerated within the surrounding 2D wetting layer and not within the GaAs matrix. This excitation scheme ensures that STCDs are limited entirely to the 2D wetting layer. Figure 8(a) the shows stroboscopic emission spectra of a QD excited at four distinct times during the acoustic cycle. The corresponding bandstructure modulations are shown in the left column in figures 8(b)–(e). The excitation conditions under which carriers are generated at the maximum electric field are referred to as *e-reflow* (b) and *h-reflow* (d), respectively. Here, either *e* (b) or *h* (d) initially drift against the SAW propagation direction and are transported back, i.e. reflow to the QD position. The opposite carrier species drifts with the SAW, and is transported away from the dot. The excitation conditions in (c) and (e) are referred to as *e-stability* (c) and *h-stability* (e). Here, the respective carrier species are generated at their stable point in the CB and VB, while the opposite charge carrier species are generated at the unstable point.

In these spectra, three dominant emission lines are identified as corresponding to the recombination of the neutral exciton $1X^0 = 1e + 1h$ and biexciton $2X^0 = 2e + 2h$, and the negative trion $1X^- = 2e + 1h$. As the time of photoexcitaton is tuned across one SAW-cycle, the time-averaged emission of the QD can be nicely programmed from predominantly $1X^-$ for *e*-reflow and *e*-stability to predominantly $1X^0$ for *h*-reflow to balanced $1X^0$ and $1X^-$ for *h*-stability. However, these data were recorded using time-integrated detection and thus the temporal evolution of the observed emission, shown in figures 8(b)–(e), cannot be deduced. This knowledge is particularly important, since the QD accommodates a well-defined number of electrons and holes at any given time. This in turn implies that the observed occupancy states do not coexist. To reveal the full dynamics, phase-locked time-domain spectroscopy is required.

Figure 9 demonstrates fully fledge phase-locked time domain spectroscopy of the two occupancy states of a single QD. Figure 9(a) shows the time integrated emission spectrum of the QD recorded under phase-locked excitation at *h*-stability, i.e. *h* and *e* carriers being generated at stable and unstable points in the bandstructure, respectively. Figure 9(b) compares the two time-transients of the PL emission of the $1X^0$ (blue line) and $1X^-$ (red line). At time $t = 0$

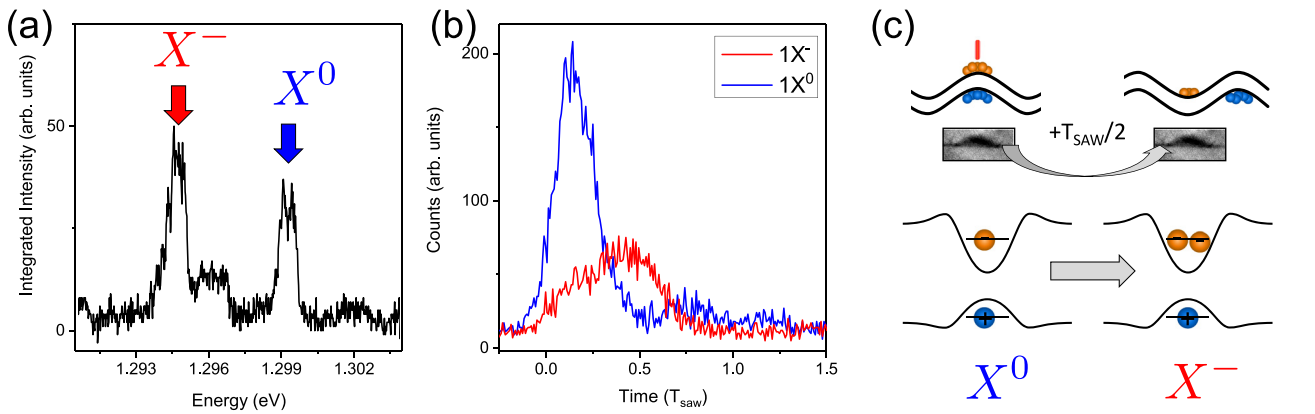

Figure 9. Dynamic charge state programming. (a) Emission spectrum of a single QD for photoexcitation at hole stability showing emission of $1X^0$ (blue arrow) and $1X^-$ (red arrow) lines. (b) Time-resolved emission of $1X^0$ (blue line) and $1X^-$ (red line) demonstrating conversion of a neutral to a negatively charged exciton at $t = T_{\mathrm{SAW}}/2$ after photoexcitation. (c) Schematic of time-delayed conversion of $1X^0$ to $1X^-$ by SAW-driven electron injection.

of photoexcitation, the $1X^0$ instantly rises, indicating preferential generation of this neutral exciton species due to preferential capture of e–h pairs on a timescale of a few tens of picoseconds [84]. The emission signal then rapidly decays and quenches at $t \approx T_{SAW}/2$ after the pump. The emission of $1X^-$ shows a nice anti-correlated behavior compared to $1X^0$: only a weak signal is detected shortly after photoexcitation and is followed by a pronounced increase with a clear peak at $t \approx T_{SAW}/2$, the time at which the $1X^0$ signal disappears. This clear anti-correlation is a direct consequence of a SAW-driven conversion of $1X^0$ to $1X^-$. This process is shown schematically in figure 9(c). For photoexcitation at h-stability, the e (orange) in the conduction band are generated at an unstable point, while the h (blue) are formed at their stable maximum of the valance band. In parallel, $1X^0$ is formed in the QD and the e quickly redistribute to the two adjacent stable minima in the conduction band. At $t \approx T_{SAW}/2$, a single e, which initially moved in the direction opposite to the SAW propagation, is transported by the SAW to the QD position and injected into its confined energy levels. Thus, the initial neutral exciton $1X^0$ is converted into the negatively charged trion $1X^-$. This explanation, albeit qualitative, nicely links the dynamic SAW-driven STCDs and the observed dynamic programming of the QD's occupancy state.

The full physical picture can be derived from combined phase-resolved time-domain spectroscopy combined with numerical simulations of the STCDs within the 2D wetting layer. Figure 10 shows the results of a combined study for of (a) $1X^0$ and (b) $1X^-$. For the full physical picture, the reader is referred to [161]. In each panel, the individual time-transients are plotted as lines for different phase-locked excitation conditions. The highlighted transients correspond to the four characteristic excitation times e-reflow (blue), e-stability (green), h-reflow (red) and h-stability (purple). Each panel also shows results of numerical simulations of the SAW-driven STCDs by solving the semi-classical drift- and diffusion dynamics of e and h carriers in the SAW-induced potential. Using the model [139, 162], the trajectories of electrons and holes within the 2D wetting layer can be calculated. As shown in [161], the time of arrival of each carrier species can be determined. From the simulation data in [161], the temporal evolutions of the electron (orange) and hole (blue) densities *at the position of the QD* can be extracted. These are plotted in color (electron (orange) and hole (blue)) in the background as a function of time during the SAW cycle (vertical direction) and time after photoexcitation. The offset of the measured time transients (lines) is set such that it matches the vertical time axis of the simulation data (color code). Comparing these calculated evolutions to the measured PL transients reveals striking correlations. (i) For $1X^0$, time-delayed enhancement of the emission coincides with a large hole density at the position of the QD. Conversely, and confirming the previous qualitative picture, a pronounced suppression is resolved at times when a large electron density is present at the QD position. (ii) For $1X^-$, no enhancement of the emission is observed for large hole densities (blue), which is expected for a net negatively charged state. Furthermore, and confirming the qualitative picture developed, an increase of the emission intensity is observed for large electron density (orange) at the position of the QD.

4.3. Long range carrier transport and injection into single QD for single photon generation

The second approach to the control of the occupancy state of single QDs with a SAW relies on ambipolar acousto-electric transport [141]. This scheme is depicted schematically in figure 11(a). Here, the position of the laser generating e–h pairs is separated by several acoustic wavelengths from the QD. The SAW's electric field dissociates excitons and the thus separated e and h carriers are transported along its propagation direction. The QD acts as a deep trap for these 'surfing' carriers, which are injected again in an inherently sequential scheme. Initial experiments towards the implementation of this unique type of single photon source were reported by Bödefeld *et al* [153], followed by the observation of photon anti-bunching by Couto *et al* [125]: figure 11(a) shows the schematic of the actual sample used for this experiment. The QDs pumped by the SAW form randomly at interface fluctuations along the

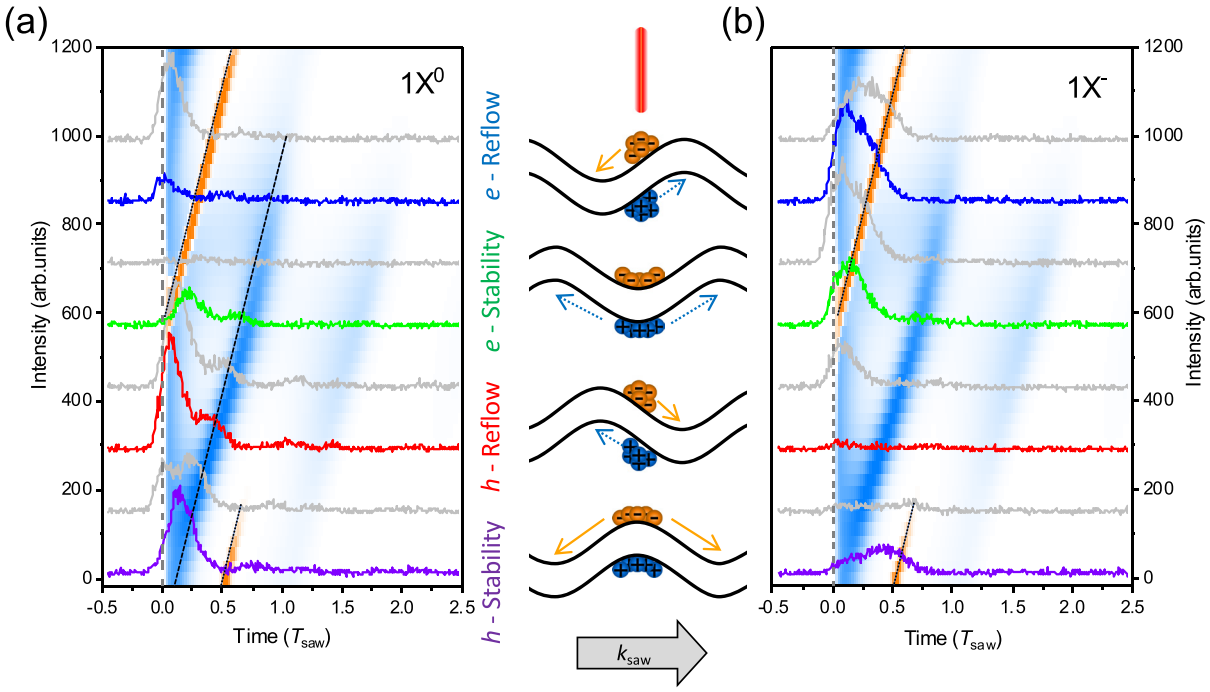

Figure 10. Time-resolved PL emission of (a) $1X^0$ and (b) $1X^-$ recorded at different times during the acoustic cycle. Data for the four characteristic excitations (schematics) are highlighted. In the background, the temporal evolutions of the calculated electron (orange) and hole (blue) densities at the position of the QD are plotted as a function of time during the acoustic cycle (vertical direction). The offset of the experimental data (lines) is chosen such that it matches the vertical time axis of the color-coded simulation data.

edges of short quantum wires (SQWRs), an array of which is located in the SAWs propagation path. The emission of these natural QDs was analyzed by a Hanbury Brown and Twiss (HBT) intensity interferometer, measuring the second order correlation function $g^{(2)}(\tau)$. Data from these experiments are shown in figure 11(b). The upper two traces compare $g^{(2)}(\tau)$ from the same position for two different SAW amplitudes, and the lower trace shows equivalent data from a second reference position. All data reveal distinct modulations corresponding to all frequencies involved in the experiment, which are marked in the figure. Most importantly, the fastest modulation corresponds to that of the SAW, directly reflecting its period T_{SAW}. In this modulation the signal at $\tau = 0$, stemming from both detectors registering a single photon at the same time, is significantly suppressed. This photon anti-bunching is a clear fingerprint of non-classical light emission and the emission of single photons [163]. Similar photon correlation spectroscopy was performed on QDs formed in nanowires (NWs) [164], demonstrating the applicability of this scheme on this emerging 1D platform; this is discussed in more detail in section 6.1.2.

Furthermore, established self-assembled columnar QPs have been proven to be ideally suited to SAW-based remote injection schemes [165]. Figure 12(a) shows the far-field emission of a remotely pumped single QP isolated by a narrow band optical filter, which also suppresses the signal from the pump laser. In this diagram, the strong emission of the QP is clearly resolved, and its pattern precisely matches the Airy-function expected for the far-field of a point-like emitter. Also, the characteristic charge state control [114, 143] is preserved under remote excitation. Figures 12(b)–(d) compare the emission (intensity color coded) of the same QP as a function of position x and photon energy. The excitation laser is located at $x = 0$. The emission of the QP shows the characteristic switching when comparing the unperturbed QP in (b) to the case with the SAW applied in figures 12(c) and (d). In the latter cases, the QP is displaced from the position of the excitation laser and its emission is found shifted in the $-x$- and $+x$-directions for the case of a downward (c) and upward (d) propagating SAW, respectively.

5. Acousto-optic spectral control

5.1. Quantum dots as high sensitivity nanoscale pressure sensors

The impact of SAW's strain fields represents the second type of interaction to control the optical emission of single QDs. In contrast to the large type-II band edge modulation due to piezoelectric potential, the underlying coupling to the deformation potential is comparably weak. Moreover, the associated type-I bandedge modulation does not lead to a spatial separation of e–h pairs and the induction of STCDs. For moderate SAW amplitudes, the magnitude of the bandgap—and thus the spectral modulation—can be well approximated by the local hydrostatic pressure p given by equation (1). The Lorentzian emission line of a single QD dynamically strained by Rayleigh-type SAW maps its dynamic pressure field, $p(t) = p_{max} \cdot \sin(\omega_{SAW} t)$. The dynamic spectral shift is given by

$$\Delta E\,(t) = \frac{dE_{gap}}{dp} \cdot p\,(t)\,, \tag{2}$$

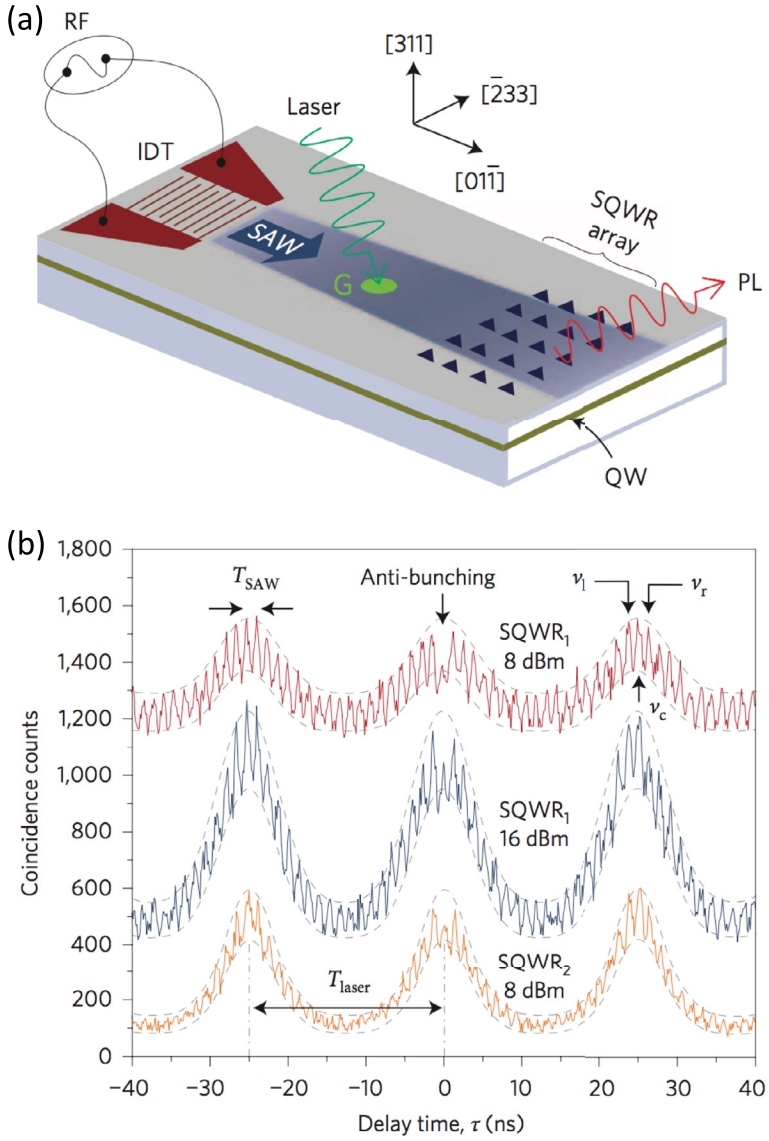

Figure 11. Photon anti-bunching from an acoustically pumped QD. (a) Schematic of sample for SAW-pumping of a remote array of short quantum wires (SQWRs) containing interface fluctuation QDs. Electrons and holes are generated by a laser pulse at position G and transported to the SQWR array triggering non-classical light emission. (b) Auto-correlation histograms recorded from a single QD at two different P_{rf} (upper and center trace) and a second QD (lower trace). All histograms show photon anti-bunching at $\tau = 0$, indicative of non-classical light generation. Reprinted by permission from Macmillan Publishers Ltd: Nature Photonics [125], Copyright 2009.

with $\frac{dE_{gap}}{dp}$ being the strength of the deformation potential coupling. This parameter depends on the material of the quantum emitter and for GaAs, this parameter amounts to $\frac{dE_{gap}}{dp} = 115\ \mu\text{eV MPa}^{-1}$ [166]. In a time- and phase-integrated experiment, this dynamic modulation is averaged and the emission lines broadens. Its lineshape is given by the integral of the time modulated Lorentzian line over one acoustic cycle:

$$I(E) = I_0 + f_{rf}\frac{2A}{\pi}\int_0^{1/f_{rf}} \frac{w}{4\cdot\left(E-\left(\Delta E\cdot\sin\left(2\pi\cdot f_{rf}\cdot t\right)\right)\right)^2 + w^2}dt. \quad (3)$$

Figure 13 demonstrates dynamic spectral tuning of a single QD by the dynamic strain field of a SAW. Figure 13(a) shows the expected sinusoidal modulation of the Lorentzian emission line of a single QD (grey) and the resulting time-integrated emission spectrum (green). From this time-integrated spectrum, given by equation (3), the tuning amplitude, labeled $2\Delta E$, can be obtained. Figure 13(c) shows the time- and phase-averaged emission spectrum of a QD modulated by a SAW as a function of the amplitude of the wave [128, 167]. The intensity is color-coded and plotted as a function of energy and P_{rf}. In these spectra, the described broadening of the emission line is clearly visible as P_{rf} applied to the transducer is increased. Obviously, the measured broadening, labeled $2\Delta E_{DP}$, is not linear on this logarithmic power scale. In fact, $2\Delta E_{DP} \propto p_{\max}$, the amplitude of the time modulated hydrostatic pressure of the SAW. Since $p_{\max} \propto u_z$, which in turn scales like $u_z \propto \sqrt{P_{rf}}$, a linear dependence $2\Delta E_{DP} \propto \sqrt{P_{rf}}$ is expected. This scaling is nicely confirmed in figure 13(d), in which $2\Delta E_{DP}$ extracted from the data in (a) is plotted in double-logarithmic representation as symbols as a function of $\sqrt{P_{rf}}$ to verify the (linear)

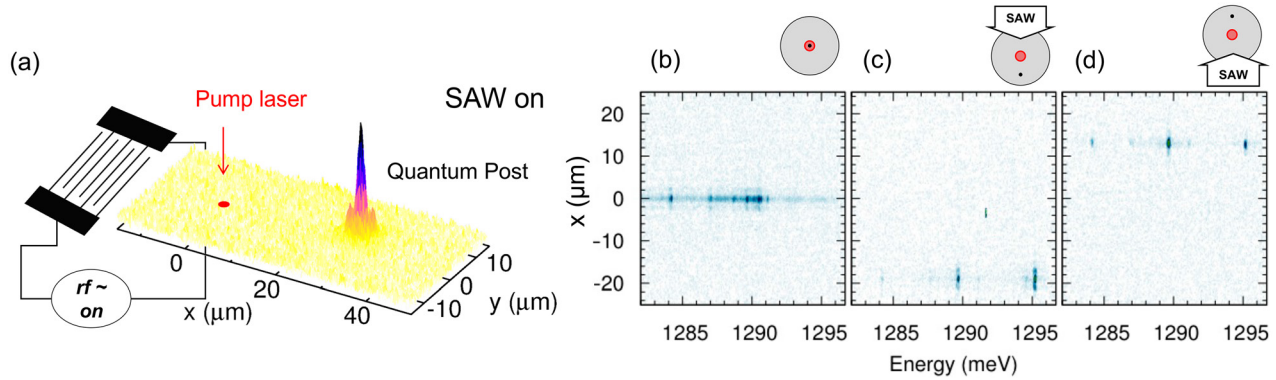

Figure 12. Remote acoustic carrier injection into a single QP. (a) PL image of the emission of a acoustically pumped single QP. The pump laser spot is located at the origin, and carriers are transported to and injected into a single QP. A diffraction limited emission is observed with the SAW applied due to acousto-electric charge transport over a distance of approximately 30 μm ($2\lambda_{SAW}$) and subsequent injection into a single QP. (b)–(d) Spatially resolved PL spectra of the same QP under direct optical excitation with no SAW applied (b) and remote injection with SAW propagating downwards (c) or upwards (d) and the QP spatially translated into the respective direction as indicated in the schematics. Reproduced from [165]

power-law dependence. In this analysis, the best fit to the data yields an exponent of $m = 0.9 \pm 0.1$ of the anticipated power law $2\Delta E_{DP} \propto \left(\sqrt{P_{rf}}\right)^m$. We note that $m = 2$ is expected for electric field-driven Stark-effect tuning. No contribution from the vertical or in-plane field component [168] is resolved in these data. Clear evidence has been obtained, however, for NW-based quantum emitters [169], which will be discussed in section 6.1.2.

As highlighted in the previous section, the spectral broadening of QD emission lines arises from the pressure at the dot's position. Since the geometric size of the QD (<50 nm) is significantly smaller than the wavelength of typical SAWs (100s of nm to μm), the dot can act as a *local, nanoscale* sensor of the acoustic pressure field. On the one hand, the time-dependence of $p(t)$ can be directly monitored as demonstrated in figures 13(b) and (c). On the other hand, the observed spectral broadening serves as direct evidence of the presence of a dynamic strain field modulating the QD. These capabilities of sensing nanomechanical fields can be combined with routine SAW spectroscopy techniques. Figure 14(a) illustrates our combined approach based on a SAW delay line. For this device, two IDTs are patterned on a piezoelectric substrate. One IDT is connected to an rf voltage source and acts as a sender. If a SAW is generated, the wave propagates across the chip and the acoustic power is reconverted into the electrical domain by the receiving IDT and detected by an oscilloscope. This measurement scheme monitors the devices global transmission properties in the electrical domain. In contrast, strain sensing by a QD is a local method of probing an acoustic field in the optomechanical domain. Figure 14(b) shows the emission of a single QD as a function of the radio frequency (f_{rf}) applied at a constant power level of $P_{rf} = +28$ dBm to a multi-harmonics transducer. The emission intensity is color coded and plotted as a function of f_{rf} (horizontal axis) and photon energy relative to the unperturbed emission. As f_{rf} is tuned, a pronounced broadening is observed at three distinct frequencies, corresponding to the first, second and third overtones of this particular IDT [170]. The modulation amplitude ΔE, extracted by fitting equation (3) to the data, is plotted as symbols in figure 14(c). In the same panel, the SAW transmission of the delay line used, measured in the electrical domain, is plotted as a solid red line. Clearly, all resonances detected acousto-optically by the QD faithfully reproduce those detected acousto-electrically via the delay line. In addition, we note that the different evolutions of the amplitudes of the acousto-optically and acousto-electrically detected peaks make it possible to deduce the frequency dependence of the optomechancial coupling parameter γ_{om} [170].

The single semiconductor QDs exhibit extremely narrow optical linewidths [171] below 1 GHz. Using high-resolution optical spectroscopy, Metcalfe *et al* [129] demonstrated that the dynamically broadened emission line in fact consists of a series of acoustic sidebands.

Figure 15(a) shows the high-resolution spectrum of a single InAs QD dynamically strained by a ≈ 1 GHz SAW with low (blue dashed spectrum) or moderate amplitude (red spectrum). The resolved sideband regime is required to establish parametric coupling schemes to transduce excitations from the optical to the mechanical domain. Parametric driving is demonstrated in figure 15(b): here the resonant laser driving the QD transition is tuned to the low energy sideband. Under these conditions, the QD is excited parametrically via a Stokes process and for moderate SAW amplitudes (red spectrum) dominant emission is detected at the resonance of the QD's Rayleigh line. This scheme is equivalent to the cooling of a mechanical oscillator mode in cavity optomechanics [172].

5.2. Time-dependent deformation potential coupling

The dynamic modulation of the QD emission can be detected in the time domain using either stroboscopy or phase-locked time domain spectroscopy [173]. Time-domain spectroscopy is very useful in monitoring complex local acoustic fields, for instance those synthesized by superimposing SAWs.

One fundamental example is the formation of an interference pattern between two counterpropagating SAWs of identical frequency at the fixed position of a QD. This is

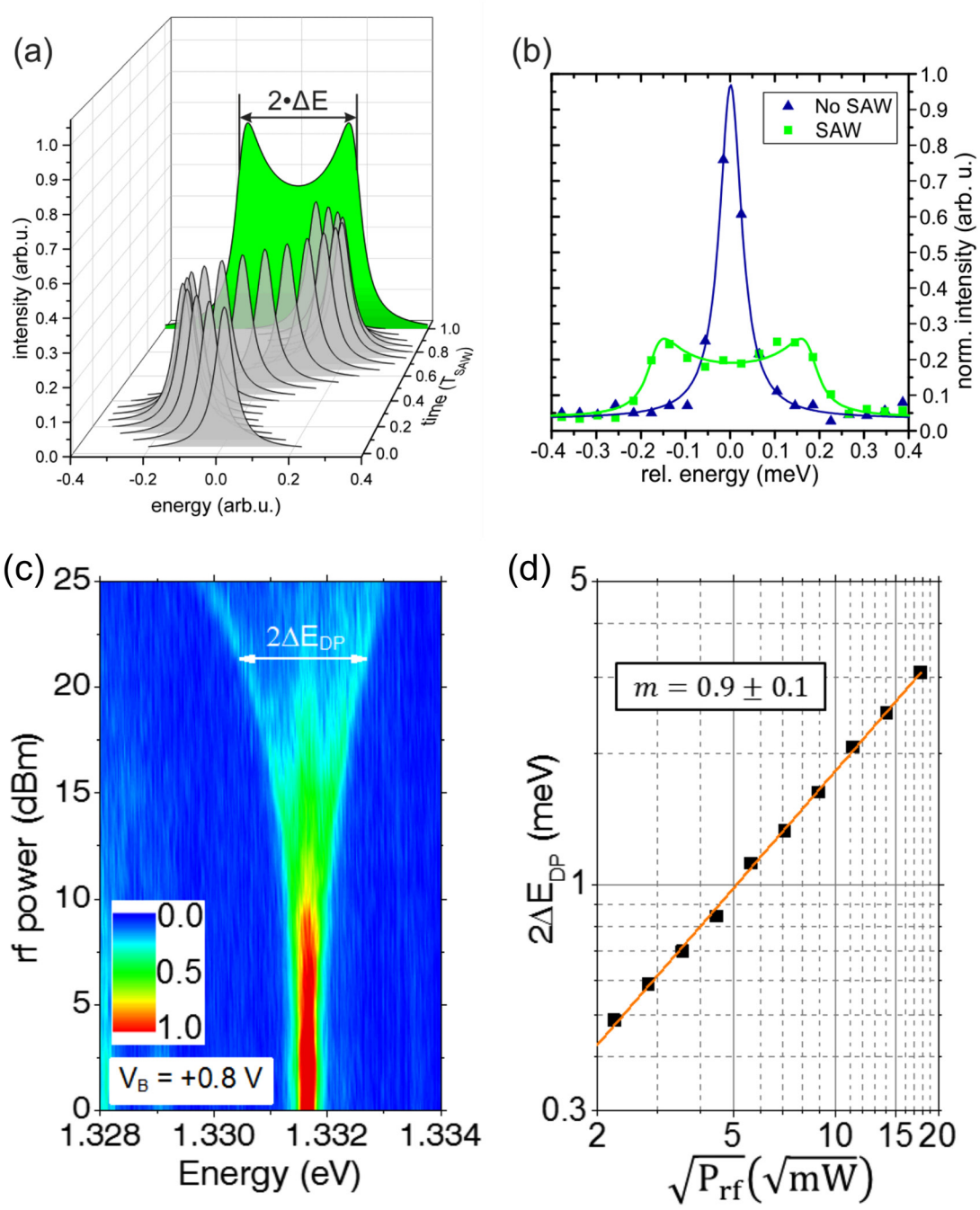

Figure 13. QD strain modulation. Modeled dynamic sinusoidal spectral tuning of a Lorentzian emission line (grey) over one acoustic cycle induced by the SAW's strain field. Integration over all times during the full cycle results in the green averaged spectrum. From fitting equation (3) to the data, the amplitude of the dynamic broadening (ΔE) can be extracted. (b) Emission of a single QD without a SAW applied (blue symbols) and strained by an 801 MHz SAW (green symbols). Solid lines are best fits of equation (3) to the experimental data. (a), (b) Reproduced from [118]. CC BY 4.0. (c) False-color plot of a single QD emission line as a function of P_{rf} exhibiting a pronounced spectral broadening. (b) Extracted spectral shift ΔE_{DP} (symbols) due to deformation potential couping as a function of $\sqrt{P_{rf}} \propto A_{SAW}$ in double logarithmic representation. Best fit to the data (line) proves the anticipated linear scaling. (c), (d) Reprinted with permission from [167]. Copyright 2015, AIP Publishing LLC.

demonstrated in figure 16. In figure 16(a), the stroboscopic emission of a single QD is plotted color-coded as a function of photon energy and the relative phase $\Delta\varphi$ of two counter-propagating SAWs. This can, for instance, be achieved by exciting the counterpropagating SAWs with two independent signal generators. As illustrated in figure 16(b), tuneable interference between a right-propagating (red) and left-propagating (blue) SAW is achieved by keeping the phase of one generator fixed and tuning the phase at the output of the second generator. As seen in the data of figure 16(a), a pattern similar to that of a standing wave is resolved as $\Delta\varphi$ is tuned: at two distinct values, destructive interference of the two SAWs occurs, and the QD emission remains unaffected. Figure 16(c) shows the underlying

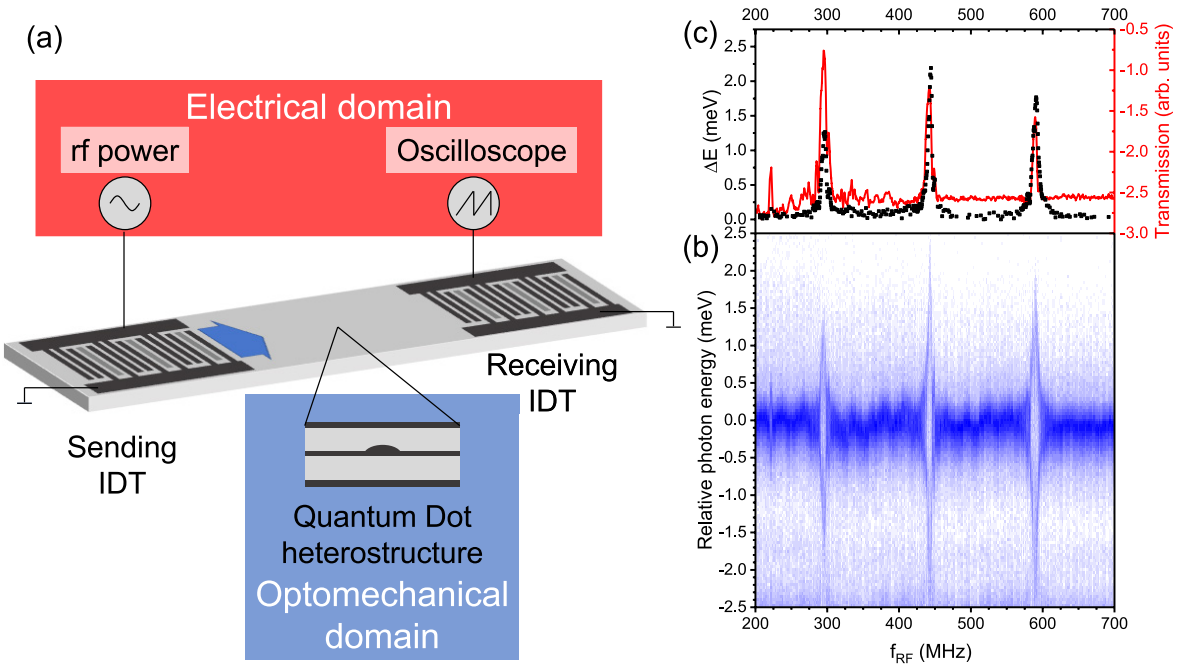

Figure 14. QD strain sensing. (a) Schematic of SAW spectroscopy using a delay line configuration: In electrical domain spectroscopy, a rf voltage signal is applied to the sending transducer (left). The transmitted SAW is converted to an electrical signal by the receiving IDT (right) and detected. In the optomechanical domain, the propagating acoustic field is detected locally via the strain response of a single QD. (b) PL emission of a single QD as a function of radio frequency applied to the IDT (horizontal axis) and photon energy relative to the unperturbed QD emission line (vertical axis). The intensity is color coded. In the data, three distinct resonances are resolved, corresponding to the 1st, 2nd and 3rd overtone of a Split5-2 multiharmonic IDT. (c) Spectral broadening of the QD emission line (black symbols) extracted from the data in (b) and transmitted SAW intensity (red line) detected by the receiving IDT faithfully reproducing the optomechanical data.

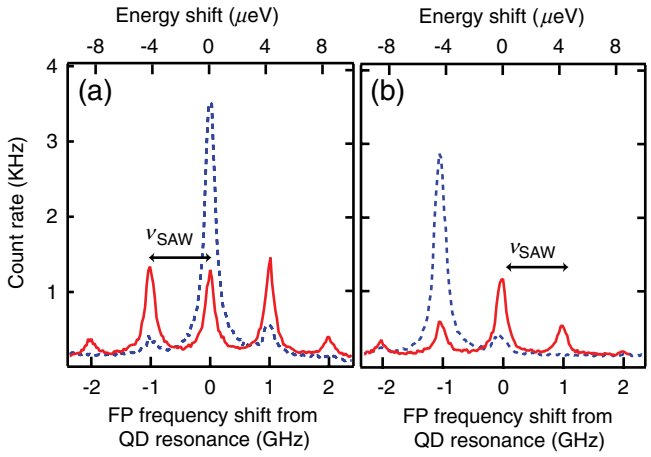

Figure 15. (a) Emission of a single QD. Resolved sideband emission of a single QD dynamically modulated by a ≈ 1 GHz SAW of low (blue dashed line) and intermediate SAW amplitude (red). (b) Same data as in (a) but with the driving laser tuned to the first lower energy sideband. The asymmetry of the spectrum under intermediate SAW excitation demonstrates parametric coupling between the sound wave and the optically excited QD. Reprinted figure with permission from [129], Copyright 2010 by the American Physical Society.

mechanism. Here, at the position of the QD, the maximum of the right-propagating and the minimum of the left-propagating SAW are superimposed. This superposition is periodic with $\Delta\varphi = 360°$. This is precisely observed in the experiment: the QD emission energy oscillates with maximum amplitude, which leads to the observation of the envelope of a standing wave pattern.

The underlying superposition principle is fundamental and can be extended to generate tailored acoustic fields. Recently, Schülein *et al* [173] demonstrated fully-fledged Fourier synthesis of acoustic waveforms from a fundamental SAW and its higher harmonics generated using multi-harmonic transducer geometries. Figure 17 shows an example of a square waveform generated by additive Fourier synthesis. The acoustic fields are designed such that the modulation of a sensor QD precisely follows the programmed square wave in the time domain. The key characteristics of the driving waveform are presented in figure 17(a). The lower panel shows the programmed profile of the hydrostatic pressure $p(t)$ being synthesized from the fundamental SAW with $f_{SAW,1} = 183$ MHz and the required second and fourth overtones at $3 \cdot f_{SAW,1} = 549$ MHz and $5 \cdot f_{SAW,1} = 915$ MHz. From this $p(t)$, the displacement at the surface and the electrical potential can be derived; these are plotted in black and red respectively in the center panel. The full displacement field and piezoelectric field of this waveform are plotted in the upper panel. The successful excitation of a square waveform acoustic field is confirmed by stroboscopy performed on a single sensor QD located in the propagation path of the waveform. Figure 17(b) shows a representative stroboscopy of a single QD recorded over two acoustic periods. The emission intensity is plotted color-coded

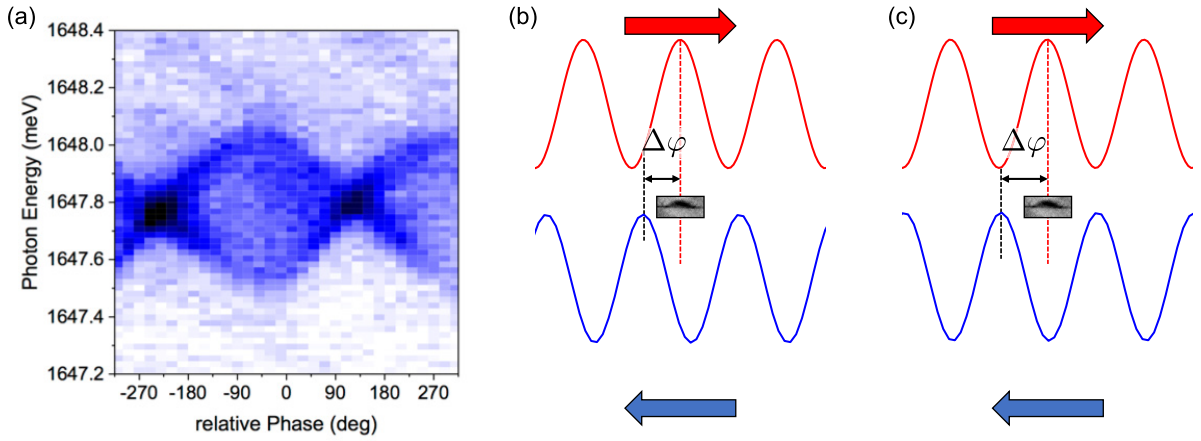

Figure 16. SAW superposition detected by a single QD. (a) Stroboscopic scan of a single QD strained by two counterpropagating SAWs with identical amplitude. Emission intensity is color-coded and plotted as a function of photon energy and phase difference $\Delta\varphi$ at the QD position. (b) Tuning the relative phase of the two SAW gives rise to the observed standing wave pattern. (c) Example of destructive interference of the two waves at the position of the QD corresponding to the nodes observed in the experimental data in (a).

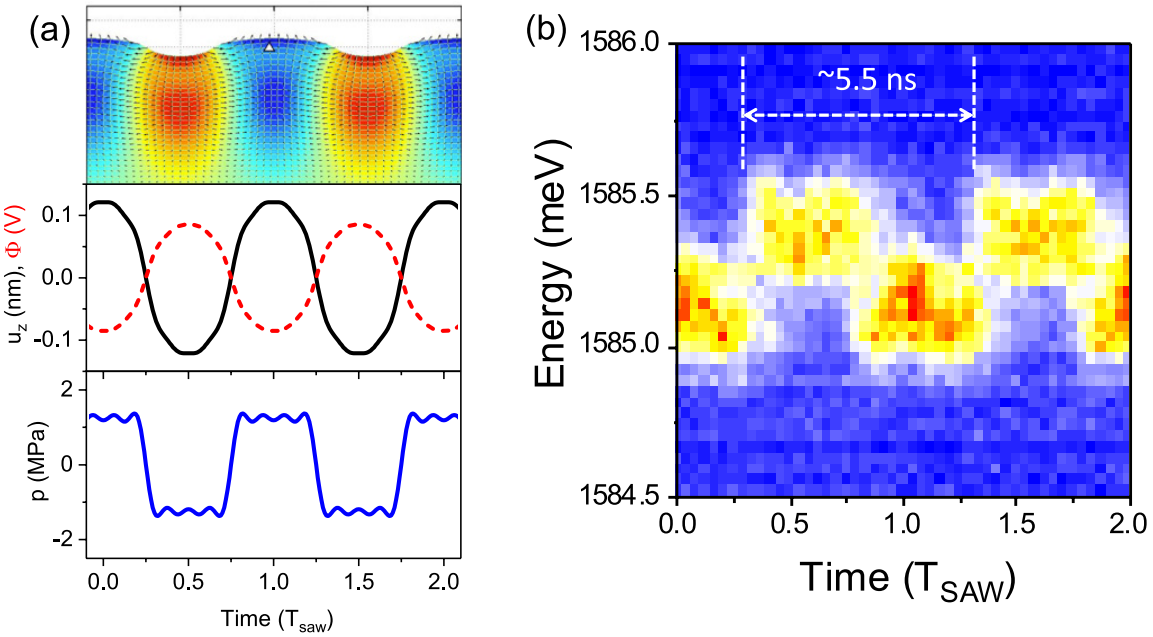

Figure 17. Fourier synthesis. (a) Waveform for square wave modulation of a QD (upper panel) as full wave profile with color-coded electric potential, (center panel) extracted surface displacement (solid black line) and electric potential (dashed red line) and (lower panel) hydrostatic pressure at the position of the QD. (b) Stroboscopy scan of a single QD modulated by a square wave with a fundamental period of ≈ 5.5 ns.

and as a function of time during the acoustic cycle and photon energy. The data clearly shows a square wave modulation of the QD emission energy as programmed via the nanomechanical waveform. This scheme can in principle be implemented for arbitrary waveforms, which marks the transfer of the paradigm of pulse shaping to the nanomechanical domain. This paradigm is employed in the electromagnetic domain on timescales spanning more than 12 orders of magnitude from rf pulses in nuclear magnetic resonance to ultrashort femtosecond optical pulses.

6. Perspectives

6.1. Hybrid devices

Although compound semiconductors condensing in zinc-blende and wurtzite crystal phases are natively piezoelectric, generation of SAWs may be hindered: the small physical size of bottom-up synthesized nanostructures—particularly semiconductor NWs—does not allow fabrication of transducers directly on the object. Also, the high electrical conductivity of doped layers or low dimensional carrier systems, for example

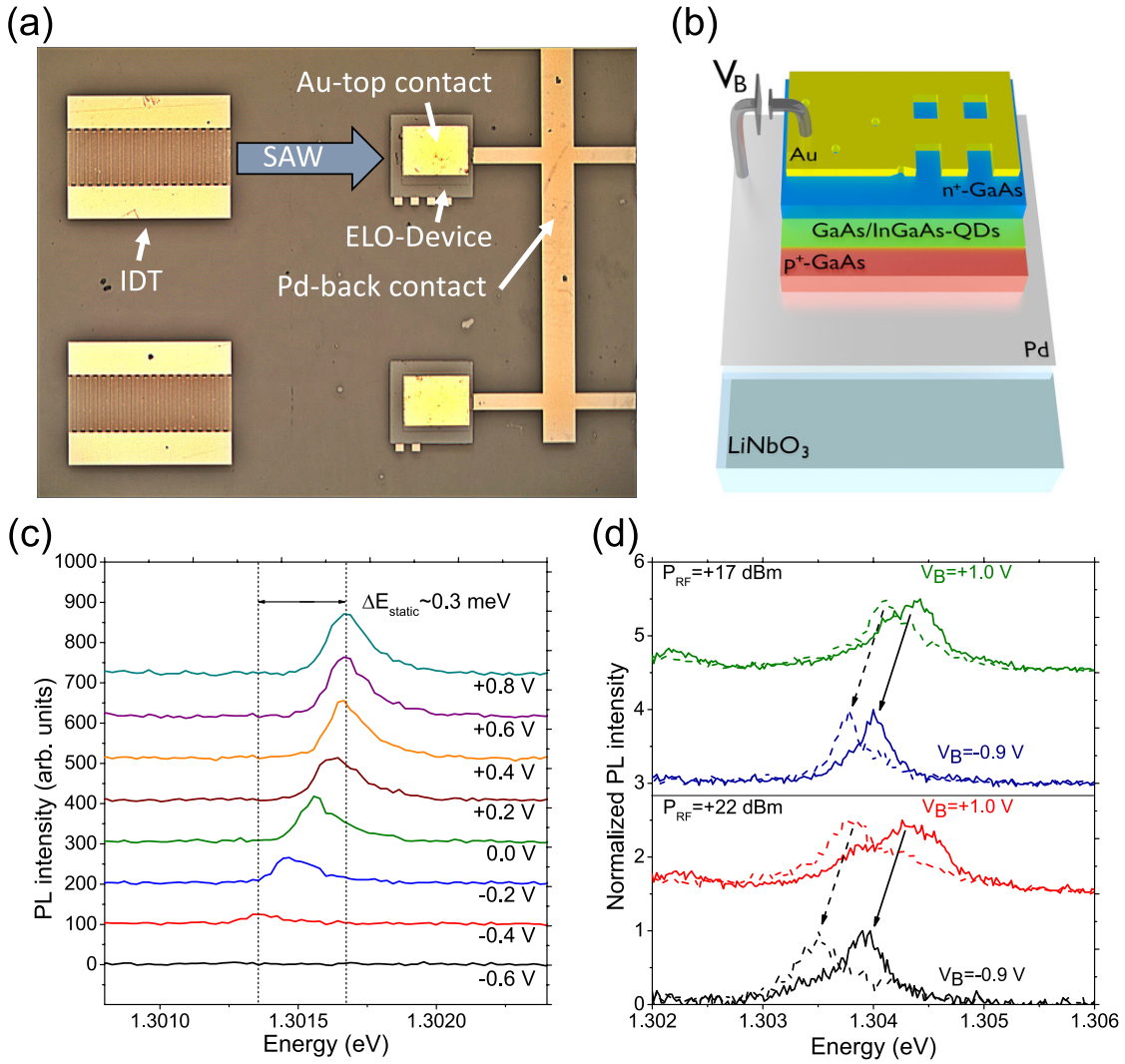

Figure 18. Hybrid QD-photodiode and $LiNbO_3$ SAW-device. (a) Microscope image of a hybrid device comprising of IDTs for SAW excitation on the LiNbO3 substrate and single QD photodiodes patterned on an ELO film. (b) Schematic of fused $LiNbO_3$-semiconductor hybrid device. (c) Static tuning the of the QD emission line by the QCSE tuned via the bias voltage applied to the photodiode. (d) Stroboscopic spectra recorded for maximum red (dashed lines) and blue (solid lines) SAW tuning for two distinct bias voltages at intermediate (upper panel) and high SAW amplitude (lower panel). The data clearly demonstrate independent static QCSE and dynamic SAW tuning.

2D electron gases, screens the rf voltage applied to an IDT, strongly reducing or even completely suppressing the conversion efficiency between the electrical and mechanical domain. For advanced applications, the low electromechanical coupling factor of III–V and II–VI compound semiconductors becomes a limiting factor. To tackle these challenges, hybrid approaches have been pursued to combine efficient SAW excitation and its coupling to particular nanosystems while at the same time overcoming the individual shortcomings of the system under study. In the following, we discuss two specific approaches in which QDs in electrically active photodiodes and quantum emitters in semiconductor NWs are manipulated by a SAW in hybrid $LiNbO_3$-semiconductor devices.

6.1.1. Epitaxial lift-off and transfer. A particular versatile approach to the hybridization of epitaxially grown layers with arbitrary host substrate is the technique of epitaxial lift-off (ELO) and subsequent transfer [174, 175]. This technique is ideally suited to the transfer of III–V and II–VI epilayers onto $LiNbO_3$ [176–181]. Recently, hybrid devices comprising a $LiNbO_3$ SAW chip and QD devices have been reported [167, 170].

Figures 18(a) and (b) show an example of a combined electrically and acoustically active hybrid device: as seen in the microscope image in figure 18(a), IDTs are patterned on a $LiNbO_3$ host chip used for SAW generation. GaAs-based *p–i–n* diodes equipped with common Pd *p*-back contacts and individual Au *n*-front contacts are patterned on the ELO film spatially separated from the IDTs. Thus, in this hybrid device, the inefficiency of generating the SAW directly on the semiconductor due to the requirement for highly doped *n*- and *p*-layers is elegantly overcome. We note that the Pd-layer also guarantees a rigid mechanical bond between the semiconductor ELO film and the SAW-chip [182]—imperative in ensuring maximum optomechanical coupling. A schematic of the cross-section through the hybrid device is shown in figure 18(b). This device combines dynamic control via a SAW with the most

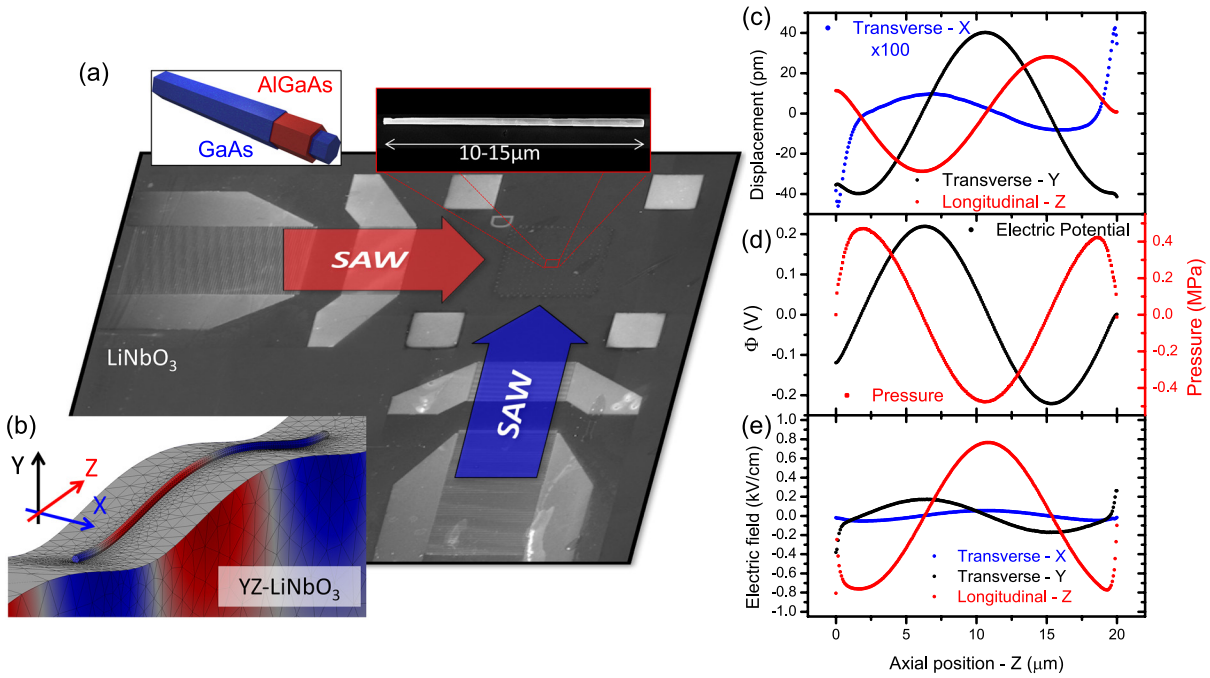

Figure 19. $LiNbO_3$-NW hybrid device. (a) SEM image of a $LiNbO_3$ SAW chip patterned with two sets of IDTs of different frequencies with perpendicular emission directions. In the 'active' region in the top right area, individual NWs (inset) can be investigated by acousto-optoelectronic spectroscopy. (b) Finite element modelling of the SAW coupling to a GaAs-based NW. The electric potential is color coded. Amplitude is not to scale. (c) Calculated displacement components, (d) electrical potential (black) hydrostatic pressure (red) and (e) components of the electric field along the axis of the NW.

established device for static control of QD nanoarchitectures. Diodes of such or similar types are routinely used e.g. to control the charge state of QDs [47, 48], tune their optical transitions via the QCSE [49], control the coupling in QD molecules [60, 61] or gate QD-based spin and charge memories [50, 183]. In figure 18(c), the emission of a single QD is shown as a function of the bias voltage (V_B) applied to the photodiode. As V_B is reduced, the electric field across the intrinsic layer of the photodiode and the QD increases. This gives rise to a shift of the emission line due to the QCSE [49]. This QCSE provides an *electro-static* tuning mechanism for the QD's optical transition. The combined *electro-static* and *acousto-optic* control is demonstrated in figure 18(d). Here, stroboscopic emission spectra at the maximum (solid lines) and minimum (dashed lines) of the SAW are compared for two different amplitudes of the SAW (upper and lower panels) and two selected values of V_B. The presented data nicely demonstrates the independence of the two tuning mechanisms employed: on the one hand, a comparison of the upper and lower panels shows that the amplitude of the acousto-optic tuning is in fact set by the amplitude of the SAW—i.e. the applied P_{rf}. On the other hand, the center of the dynamic acousto-optic modulation shifts to lower photon energies as V_B decreases. The dynamic SAW-tuning and the static tuning by the applied bias voltage are mutually independent. Therefore, this hybrid device combines inherently fast acousto-optic control via a SAW with the broad palette of static tunings and spectroscopy techniques [39, 54, 184–186] enabled by the diode structure.

6.1.2. Quantum emitters in NWs. Semiconductor NWs represent a vibrant field of fundamental and applied research. The 1D nature of these filamentary crystals promises confinement of charge carriers, phonons and photons. In this highly active field, SAWs have been successfully employed e.g. to drive an acousto-electric current [187, 188], induce charge carrier dynamics [130, 154, 189] or to study quantum emitters. All approaches require a hybrid approach. Figure 19(a) shows an electron micrograph of a $LiNbO_3$ SAW-chip designed for SAW experiments on single NWs. Two sets of IDTs are arranged such that the SAW beams emitted by each set are perpendicular and intersect in an 'active region' in which individual NWs can be studied optically. A SEM image and a schematic of a GaAs/(Al)GaAs core–shell NW are shown in the figure. The coupling of the mechanical and piezoelectric fields from the $LiNbO_3$ substrate into the semiconductor NW can be quantified by FEM. A typical result is shown in figure 19(b) for a Rayleigh-SAW propagating along the Z-direction of a Y-cut $LiNbO_3$ substrate. The piezoelectric potential is color-coded, with red (blue) showing large positive (negative) values. Most importantly, this simulation shows that the piezoelectric potential inside the NW follows precisely that in $LiNbO_3$. A detailed analysis of key parameters along the axis of a [1 1 1]-oriented NW is compiled in figures 19(c)–(e) for a maximum vertical displacement $u_Y = 40\,\text{pm}$ at the center of the NW. The local displacement in the normal (transverse Y) and propagation (longitudinal Z) axes follows that of the Rayleigh-SAW on the underlying $LiNbO_3$. Remarkably, the simulations confirm the presence of a small but finite displacement along the X-direction. This deformation results from the piezoelectric properties of the GaAs NW itself. This piezoelectric effect, induced by the potential of the SAW, modulated the thickness of the NW in the normal direction.

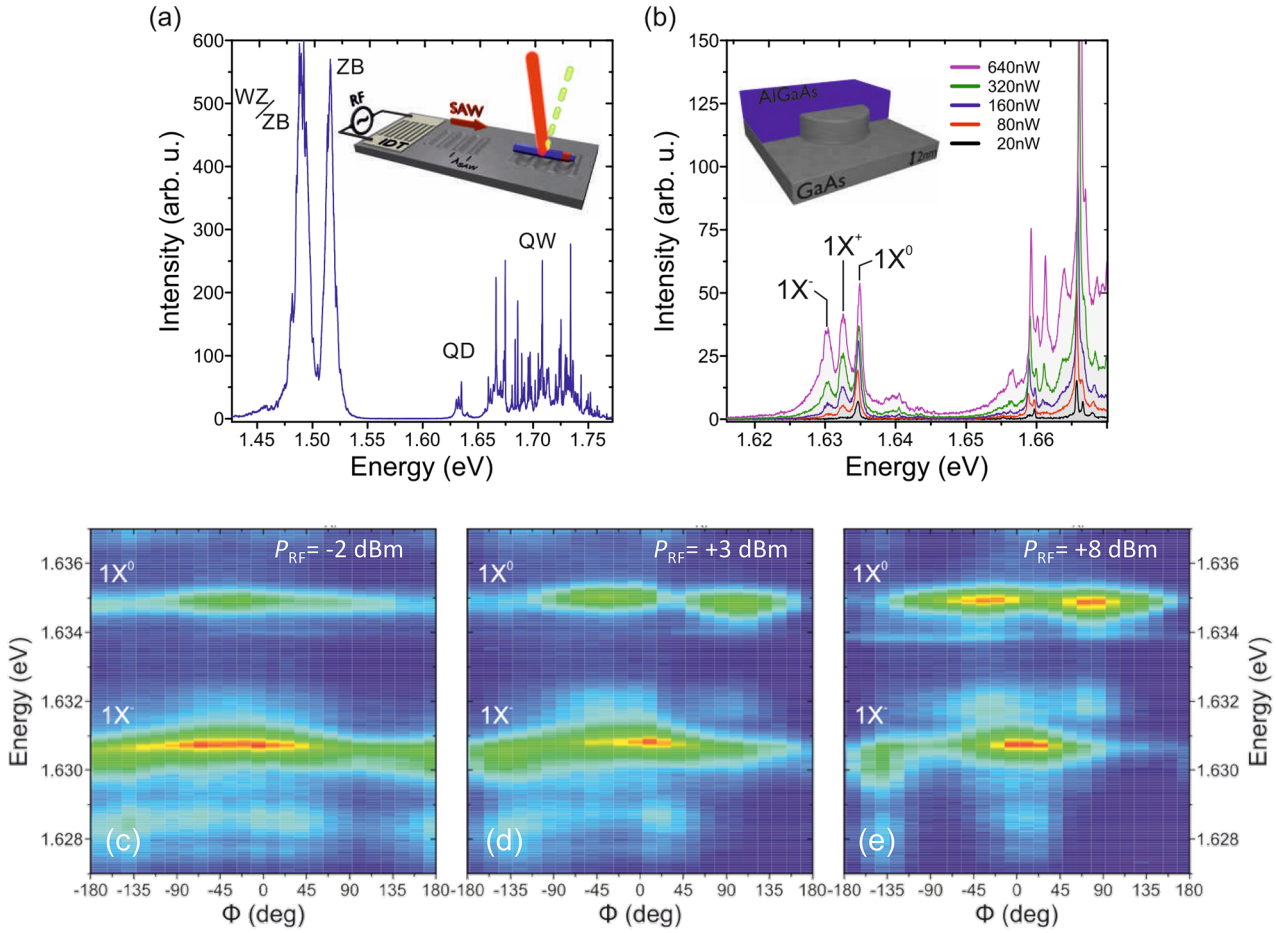

Figure 20. Acoustically regulated carrier injection in a single interface QD in a NW. (a) Overview spectrum exhibiting signatures of pure ZB and mixed WZ/ZB phases. The emission of a single interface fluctuation QD is detected in the low energy part of the emission band of the 2 nm QW. Inset: schematic of the experimental setup. (b) PL of a single interface fluctuation QD as a function of excitation power showing the emergence of charged excitons ($1X^+$, $1X^-$ in addition to the neutral exciton $1X^0$). Stroboscopic PL spectra in false color representation for (c) $P_{rf} = -2$ dBm, (d) +3 dBm, (e) +8 dBm: maximum $1X^-$ intensity is detected for $\varphi = 0$. The additional maximum of $1X^0$ develops for $\varphi \simeq 90°$. Reproduced with permission. All rights reserved. Reproduced from [190]. © IOP Publishing Ltd. All rights reserved.

This in turn gives rise to a plastic deformation in the perpendicular transverse direction. The resulting piezoelectric potential Φ and hydrostatic pressure p are plotted in figure 19(d). The potential exhibits the expected $\Phi \propto -u_Y$ dependence set by the substrate. In addition, the 90°-phase shift between the dominant displacement component u_Y and p is well reproduced. Finally, the electric field, $\vec{\mathcal{E}} = -\vec{\nabla}\Phi$, is shown in figure 19(e). The electric field can induce STCD, a QCSE or carrier tunnelling in the NW. Again, the longitudinal component $\mathcal{E}_Y$ dominates. This component induces STCD along the axis of the NW [130, 154]. In contrast, the two smaller transverse field components $\mathcal{E}_Z$ and $\mathcal{E}_X$ may only induce the motion of carriers at significantly shorter distances, perpendicular to the axis of the NW.

6.1.2.1.SAW-driven carrier injection in radial heterostructure QDs. First, we focus on a recent experiment performed on a radial heterostructure NW [190]. Here, the GaAs core of the NW was overgrown in the radial direction by a (Al)GaAs shell in which a thin, 2 nm wide GaAs QW was embedded. In the PL spectrum presented in figure 20(a), the emission of this QW is found at the high energy side, well separated from the zinc blende (ZB) and wurtzite/ZB (WZ/ZB) emission band of the GaAs core. Due to pronounced thickness fluctuations of this thin and disordered QW, the emission breaks up in a large series of discrete sharp emission lines. These stem from randomly forming 'natural' QDs, which have been studied for planar QWs since the 1990s [149, 191]. A schematic of such a 'natural' interface QD is shown in figure 20(b). At the low energy side of the QW band, the emission of single QD can be isolated. From excitation power dependent spectroscopy, shown in figure 20(b), different excitonic species can be identified [192]. Since these 'natural' QDs natively form inside of a QW, they are ideally suited to employ STCDs to control the charge state of the QD. This is demonstrated in figures 20(c)–(e) using stroboscopic spectroscopy for low, intermediate and high SAW amplitudes. In these data, dynamic programming fully analogous to that observed for self-assembled QDs in planar heterostructures is observed. We note that Hernandez-Minguez *et al* have demonstrated remote carrier injection and acoustically gated photon anti-bunching on a NW-platform [164] and Lazic *et al* showed SAW-control of III-N QDs in

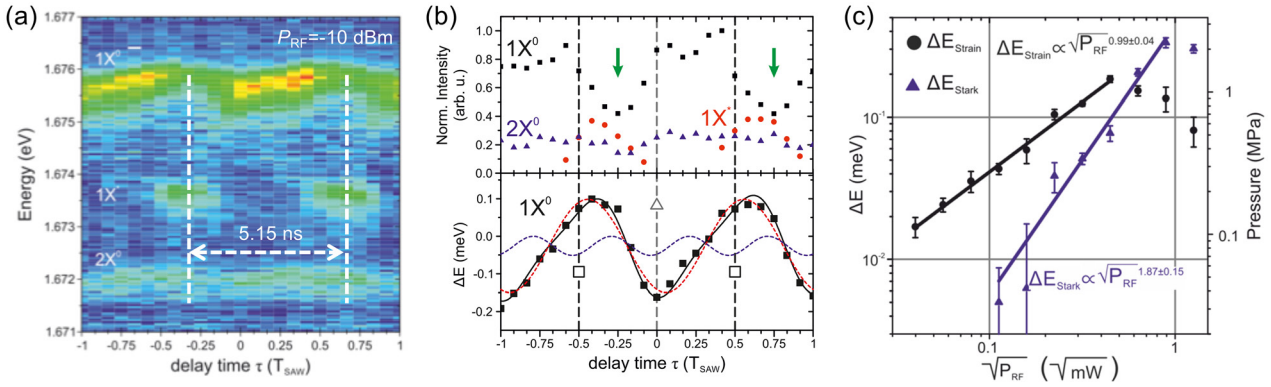

Figure 21. SAW control of a QD-like emission center in the high band shell of a GaAs-(Al)GaAs core–shell NW. (a) Stroboscopic scan showing non-sinusoidal spectral modulation of the $1X^0$ emission line and anti-correlated intensity oscillations between the $1X^0$ and $1X^*$ signals. (b) Extracted emission inensities of the the $1X^0$ (black squares), $1X^*$ (red bullets) and $2X^0$ (blue triangles) signals (upper panel) and spectral modulation of the $1X^0$ emission line (black squares) with fit of the strain (red dashed line) and QCSE (blue line) component of the full spectral oscillation (black solid line). (c) Amplitude of the strain and QCSE tuning as a function of amplitude of the SAW in double logarithmic representation. Both contributions exhibit the expected linear and quadratic dependences. The breakdown of the strain tuning at high $\sqrt{P_{rf}}$, i.e. SAW amplitudes, is attributed to detachment of the NW from the SAW-chip. Reprinted with permission from [169]. Copyright 2014 American Chemical Society.

NWs [131, 193]. These key findings clearly prove that all concepts devised for planar systems can be transferred to a NW architecture.

6.1.2.2.Combined acousto-electric and acousto-optic control. GaAs-based NWs are typically overgrown by a higher bandgap (Al)GaAs shell. This shell prevents carrier transfer to the surface of the NW. At the surface of GaAs, carriers are efficiently lost via non-radiative surface recombination. This dominant loss-channel for unpassivated GaAs NWs is suppressed by a thin (Al)GaAs blocking layer [194]. Within the ternary (Al)GaAs, random fluctuations of the Al-content are inevitable, which in turn lead to the formation of Ga-rich domains which act as QD-like emission centers (ECs) [195, 196]. Figure 21(a) shows a stroboscopy scan of a single EC, recorded over two acoustic cycles of $T_{SAW} = 5.15$ ns. In addition to a pronounced modulation of the emission intensities, displayed in the upper panel of figure 21(b) and discussed in more detail in the following section, the observed *spectral* modulation of the dominant emission line ($1X^0$) is clearly non-sinusoidal. This latter observation points towards an additional mechanism contributing to the spectral modulation. The observed spectral tuning of the $1X^0$ line is plotted in the lower panel of figure 21(b). The solid black line is a best fit to the experimental data, comprising two components: the first component (dashed red line) is the well-established modulation by the deformation potential, which scales linearly with amplitude and $\Delta E_{DP} \propto u_z \propto \sqrt{P_{rf}}$ as discussed in section 5. The second component (dashed blue line) arises from the QCSE. The QCSE gives rise to an energy shift given by $\Delta E_{Stark} \propto -\mathcal{E}^2 \propto u_z^2 \propto P_{rf}$, thus always reducing the energy of the transition [140, 197]. This is nicely confirmed by the fit. Moreover, from the phase relation of the two contributions, the observed modulation by the QCSE effect can be attributed to the longitudinal field component, pointing along the axis of the NW. This is consistent with the FEM in figure 19, which predict this component to be the largest. The different power laws of the two contributions, deformation potential $\propto \sqrt{P_{rf}}$ and QCSE $\propto \left(\sqrt{P_{rf}}\right)^2$ are nicely confirmed in a P_{rf}-scan. The modulation amplitudes obtained of the two contributions are plotted as a function of $\sqrt{P_{rf}}$ in figure 21(c). In this log-log representation, these two power laws are confirmed by linear fits (lines) to the experimentally obtained modulation amplitudes (symbols).

6.1.2.3.Dynamic charge state control: acoustically regulated carrier extraction. One peculiar property of the ECs studied in [169] is the energy hierarchy in this system. Since these emitters are Ga-rich regions within an (Al)GaAs-shell around a GaAs/(Al)GaAs core–shell NW [195, 196], their confined energy levels of electrons and holes are at *higher energies* compared to the bulk-like core of the NW or 2D GaAs QWs inside the (Al)GaAs shell. Thus, electrons in particular can rapidly tunnel from these 0D inclusions into the unpopulated continua of states extending to lower energies. This tunnel process of an electron from an emission center (EC) to the NW core or a QW is illustrated in figure 22(a). The transverse electric field component of the SAW dynamically raises (left schematic) or lowers (right schematic) the tunnel barrier compared to the field-free case (center schematic). The periodicity of this *directional* process is T_{SAW}, which is confirmed by the experimental data in figure 21: the dominant emission line $1X^0$ exhibits exactly one intensity minimum at precisely the same time during the acoustic cycle in which a second emission line $1X^*$ appears. In the upper panel of figure 21(b), the extracted emission intensities of $1X^0$ (black symbols) and $1X^*$ (red symbols) nicely confirm this anti-correlation and T_{SAW}-periodicity. Note that this modulation is phase-shifted compared to the spectral modulation by the QCSE in the lower panel. This is expected because the QCSE modulation is induced by the dominant longitudinal field component (denoted F_Y in the figure 22), while carrier tunneling is driven by the smaller yet still sizable transverse field. As

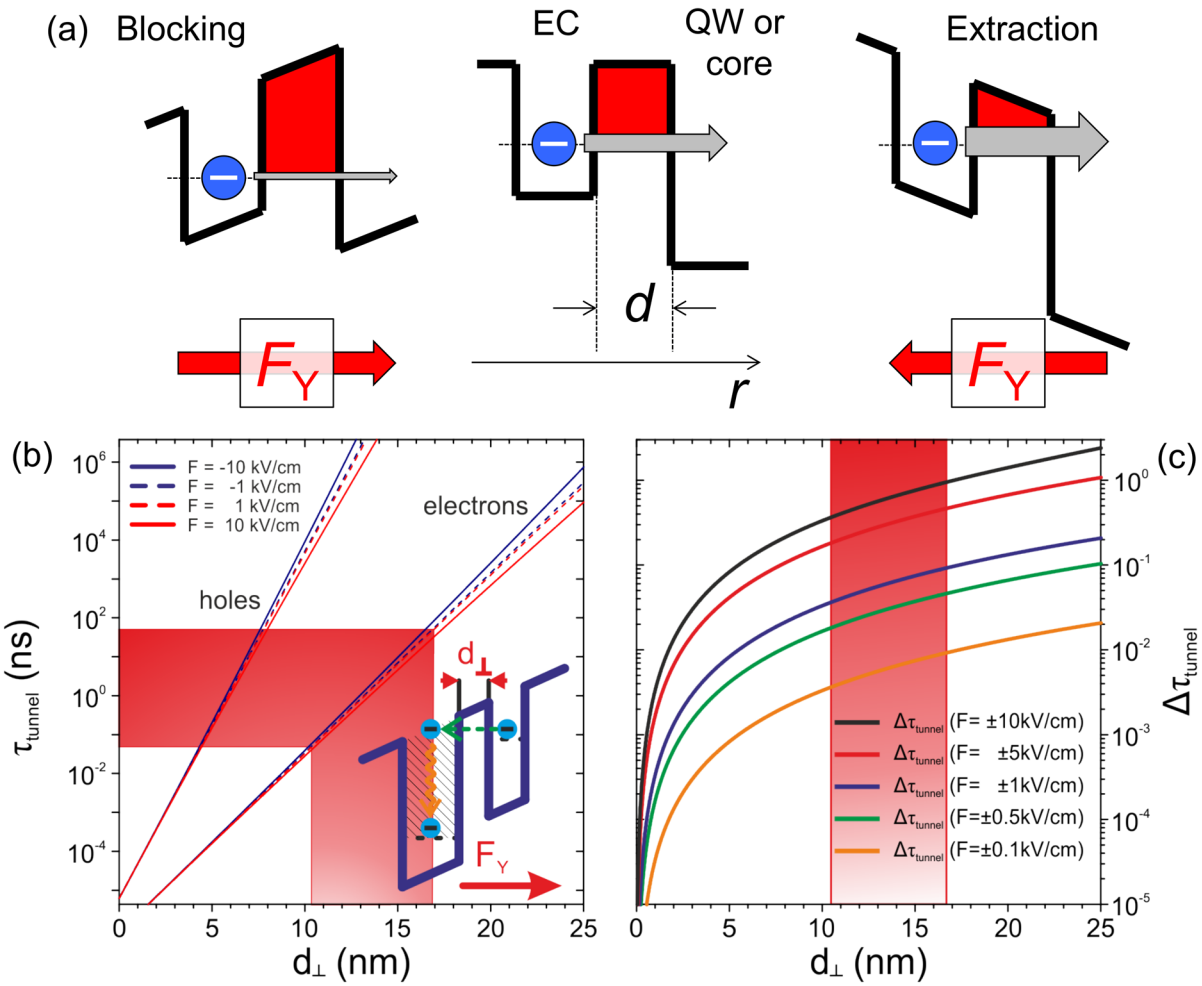

Figure 22. SAW regulated carrier extraction from a QD-like EC. (a) Schematic of the conduction band of a QD-like EC coupled to a continuum of states at lower energy in the field-free configuration (center) and for the electric field of the SAW raising (left) or lowering (right) the tunneling barrier. (b) Calculated tunneling time of electron and hole from the EC to the continuum for two different electric fields as a function of distance between the EC and the continuum. The red shaded area marks the realisitc range of distance derived from realistic PL decay times. (c) Calculated modulation of the tunneling time as a function of the distance between the emission center and the continuum, demonstrating tuning of the modulation of the tunneling time by the electric field of the SAW.

explained, this effect is based on SAW-regulation of the electron's tunneling time. It can be modeled using approaches well established for tunneling-induced gate-leakage in thin-oxide MOSFETs [198]. The tunneling times of electrons and holes derived from this model are plotted as a function of the barrier width $d_\perp$ in figure 22(b) for low $\left(\pm 1\,\mathrm{kV\,cm^{-1}}\right)$ and moderate $\left(\pm 10\,\mathrm{kV\,cm^{-1}}\right)$ transverse electric field. The horizontal red-shaded area indicates the range of tunneling times compatible with the observed emission decay times of these emitters [199]. The vertical red-shaded area marks the corresponding range of $d_\perp$ predicted by the model. This model is also capable of predicting the relative modulation of the tunneling time $\Delta\tau = \frac{|\tau(\mathcal{E}_{blocking}) - \tau(\mathcal{E}_{extraction})|}{\tau(\varepsilon=0)}$. The calculated $\Delta\tau$ as a function of $d_\perp$ is plotted in figure 22(c) for different transverse electric fields. The calculation predicts a pronounced increase of the modulation which increases with increasing transverse electric field. Moreover, the calculated $\Delta\tau$ is well developed for the range of $d_\perp$ derived from the absolute tunneling times, marked by the red-shaded area.

6.2. Coupled QD nanocavity systems: control of light matter-interactions by sound

In the work presented so far, QDs have been embedded in optically isotropic media. Thus, the excitonic two-level system couples to extended, 3D radiation modes. Over the past almost two decades, a wealth of research has been conducted with the aim of deliberately controlling the coupling between light and matter by embedding single QDs in tailored photonic environments, most prominently nanoscale photonic resonators. In the latter, the optical field is concentrated in small volumes in high quality (Q) factor optical modes with discrete frequencies. The optical field is dramatically enhanced on and strongly suppressed off resonance. This field enhancement (suppression) leads to an increase (reduction) of the spontaneous emission rate of an emitter at or away from a mode's resonance. This phenomenon is known as the Purcell effect [72] and can be derived from time-dependent perturbation theory by applying Fermi's Golden Rule [200]. In the idealized case of a single optical mode with Lorentzian line shape,

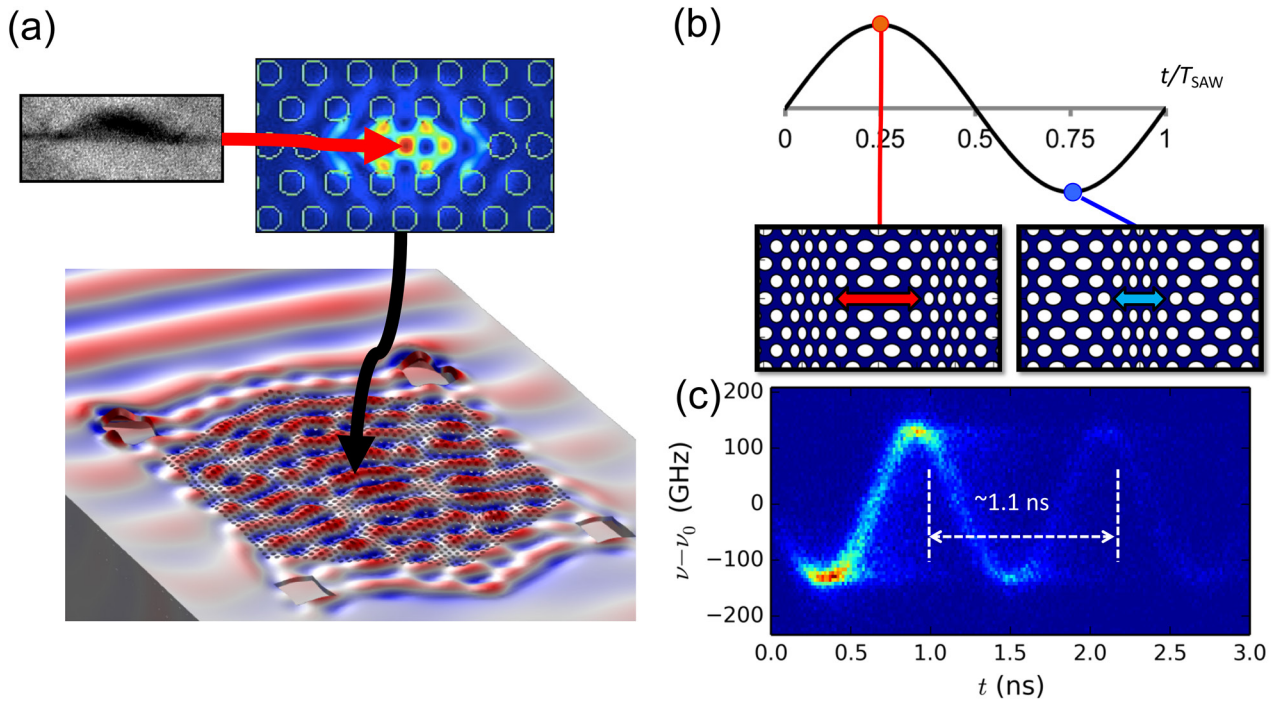

Figure 23. SAW tunable QD-nanocavity system. (a) FEM of a SAW modulated photonic crystal membrane. A L3-type nanocavity containing single QD is located in the center of the structure. The QD couples to the optical field localized in the cavity (image shows the calculated mode profile) forming a solid-state cQED system. (b) Schematic of SAW-driven nanocavity tuning: for the maximum (red) of the acoustic field located in the center of the cavity, the resonator is effectively stretched, which leads to a red shift of the mode. A blue shift is expected for the minimum at the center of the cavity. (c) Experimental observation of dynamic cavity tuning using phase-locked time-domain spectroscopy. Here, this effect is observed for a non-resonantly excited cavity driven by an ≈ 0.9 GHz acoustic wave.

the Purcell effect can be quantified by the so-called Purcell factor defined as:

$$F_p = \frac{W^{cav}}{W^{free}}. \tag{4}$$

In this expression W^{free} and W^{cav} denote the spontaneous emission rate of the emitter in an isotropic optical medium and inside the cavity, respectively. Thus, $F_p > 1$ corresponds to an enhancement, $F_p < 1$ to a suppression of the radiative emission. Using Fermi's golden rule and assuming a single mode cavity, the Purcell factor is given by

$$F_p = \frac{3Q(\lambda/n)^3}{4\pi^2 V_0} \cdot \left(\frac{\left|\vec{p} \cdot \vec{\mathcal{E}}\right|}{|\vec{p}| \cdot \left|\vec{\mathcal{E}}\right|} \right)^2 \cdot \frac{{\Delta E_{cavity}}^2}{4(E_{emitter} - E_{cavity})^2 + \Delta E_{cavity}^2}. \tag{5}$$

Here, E_{cavity} and $E_{emitter}$ denote the transition energy of the emitter. The properties of the cavity are quantified by its quality factor $Q = E_{cavity}/\Delta E_{cavity}$ and the modal volume in units of cubic optical wavelengths $V_0/(\lambda_{opt}/n)^3$. $\frac{\left|\vec{p} \cdot \vec{\mathcal{E}}\right|}{|\vec{p}| \cdot \left|\vec{\mathcal{E}}\right|}$ is the normalized projection of the optical dipole $\vec{p}$ on the electric field of the cavity $\vec{\mathcal{E}}$. We note that equation (5) does not depend on the modulus of the dipole moment of the emitter but only on its orientation with respect to the cavity's polarization axis. Most importantly for the experiments discussed in the following, F_p depends on the spectral detuning between emitter and cavity

$$\Delta E = E_{emitter} - E_{cavity} \tag{6}$$

and exhibits a maximum of $F_{p,max} = \frac{3Q(\lambda_{opt}/n)^3}{4\pi^2 V_0}$ for $\Delta E = 0$ and a perfectly aligned emitter, $\frac{\left|\vec{p} \cdot \vec{\mathcal{E}}\right|}{|\vec{p}| \cdot \left|\vec{\mathcal{E}}\right|} = 1$. Semiconductor QDs are ideally suited to the realization of a solid-state cavity quantum electrodynamic (cQED) system because they can be incorporated in a broad variety of cavity systems [201]. Ground breaking experiments demonstrating the Purcell effect have been conducted over the past 20 years by coupling QDs to localized modes of, for instance, whispering gallery disk resonators [202], pillar-type or aperture-type microresonators [73, 203–205] or photonic crystal defect cavities [206–208]. In fact, for all three architectures, the regime of strong light-matter interaction has also been entered [74–76, 209–211], in which excitons and photons form coherent polaritons split by the vacuum Rabi frequency. In this regime, coherent control of single optical excitations and single photons becomes feasible [212].

6.2.1. Dynamic acoustic modulation of photonic crystal nanocavities. In the following, we discuss the implementation of a dynamically tunable Purcell effect of a single QD inside a defect cavity in a photonic crystal membrane (PCM) driven by a SAW. This system is introduced in figure 23(a): a thin, typically 150–250 nm suspended membrane is perforated by a 2D periodic pattern of air holes. The imprinted static modulation of the dielectric properties in the plane of the membrane creates a photonic band structure. These structures are designed such that a photonic band gap opens for frequencies matching the optical transition of QDs located in the center of

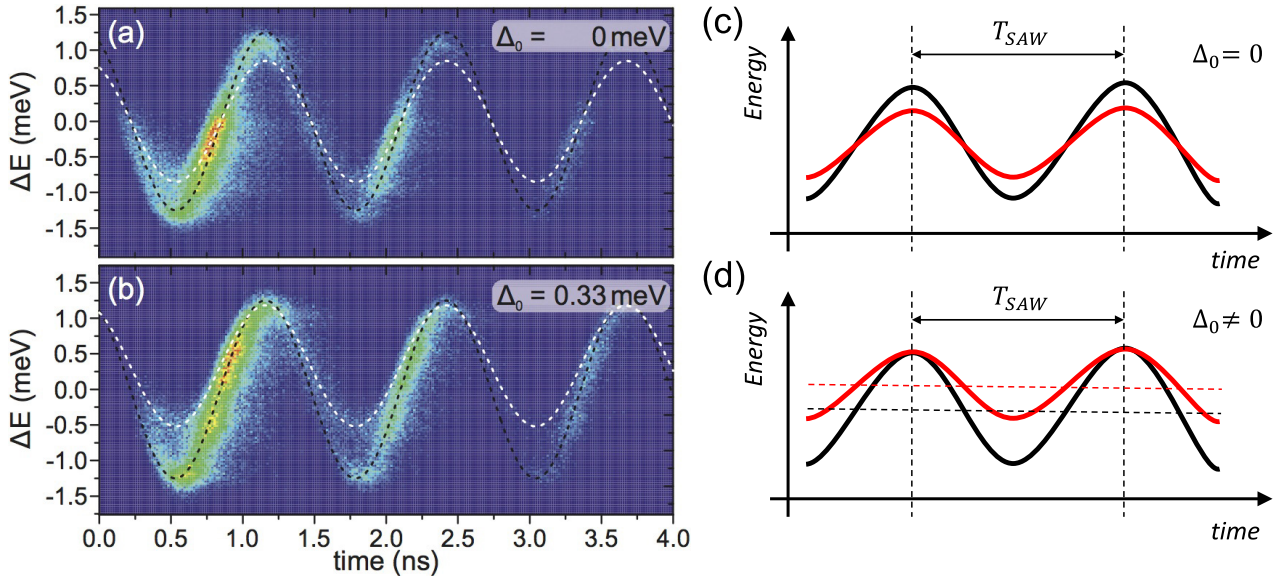

Figure 24. (a), (b) Temporal modulation of the normalized PL emission of the QD-cavity system for (a) $\Delta_0 = 0$ and (b) $\Delta_0 = 0.33$ meV. The dashed black and white lines are guides for the eye to the modulations of cavity and QD, respectively. Reprinted with permission from [126]. Copyright 2016, AIP Publishing LLC. (c), (d) Schematic of the QD and NC tuning corresponding to the setting in (a) and (b).

the PCM. This platform is particularly versatile as it allows the realization of a myriad of functional photonic elements (cavities, waveguides, splitters, etc) which can be combined to form large-scale circuits [213]. Here, we restrict ourselves to nanoscale optical cavities: by deliberately introducing a defect in the array, light can be localized to small volumes in high-Q modes within the photonic band gap. The calculated electric field pattern of an *L*3-type nanocavity is formed by a line of three missing holes [214]. As indicated in figure 23(a), for maximum light–matter coupling, a single QD has to be located in the center anti-node of the optical field of this solid state cQED system [76]. Since PCMs constitute a planar platform, they are ideally suited to interfacing with SAWs. A finite element model of a Rayleigh SAW coupling to a PCM is shown in the lower part of figure 23(a). The wavelength on the unsuspended (upper) part and the shape of the free-standing the PCM was assumed to be identical to that in our recent experiment [126]. Our simulation nicely confirms the coupling of the incident Rayleigh SAW into Lamb-modes propagating on the membrane. Since the phase velocity of these plate modes is reduced by a factor of approximately three, the acoustic wavelength reduces by the same factor. In addition, diffraction at the edges of the suspended PCM leads to a lateral modulation of the acoustic field in the membrane. Crucially, a clear harmonic modulation is predicted at the position of the defect in the center of the PCM. Thus, for this set of parameters, the SAW provides a global modulation of the membrane and the defect cavity. The dynamic spectral modulation of these nanocavities can be understood qualitatively based on a simple model [115], schematically shown in figure 23(b). The in-plane displacement of the acoustic field dynamically deforms the cavity. If a maximum is located in the center of the cavity, the resonator length is increased, and the mode is thus red-shifted to longer wavelengths, i.e. lower frequencies. When a minimum is in the center of the cavity, it detunes the resonance blue to smaller wavelengths. At the nodes of the oscillation, the cavity length remains unchanged. Figure 23(c) shows an experimental demonstration of dynamic cavity tuning driven by a $f_{SAW} \approx 0.9$ GHz SAW using phase-locked time-domain spectroscopy. In this experiment, the cavity was loaded with photons by non-resonant QDs. Since the decay rate of this process is independent of the emitter and its coupling to the optical mode, the unperturbed cavity modulation is probed in this experiment. The observed intensity profile shows pronounced enhancements at the maximum and minimum of the oscillation arising from the minimum tuning rate at these times.

The PCM architecture employed in these experiments is highly flexible. The interfacing with SAWs can be readily extended to complex coupled photonic elements. Kapfinger *et al* showed dynamic control of inter-cavity couplings in a photonic molecule formed by two adjacent *L*3 nanocavities [124]. We note that similar experiments have been conducted on AlN nanocavities. The high acoustic phase velocity of AlN enabled tuning by elastic waves with frequencies in the microwave K band [215, 216].

6.2.2. Acoustically regulated single photon emission from a coupled QD-nanocavity system. Next, we move on to a coupled QD-nanocavity system. In general, both QDs and nanocavity experience in-phase dynamic modulations, $\propto \sin \omega_{SAW} t$. Thus, the detuning becomes time dependent:

$$\Delta E_{QD-NC}(t) = E_{emitter}(t) - E_{cavity}(t) = \Delta_0 + \Delta \cdot \sin \omega_{SAW} t. \quad (7)$$

In this expression, Δ_0 and Δ are respectively a static detuning without the presence of the acoustic wave and the amplitude of the SAW-driven modulation of the detuning. Figures 24(a) and (b) depict phase-locked time-domain spectroscopy data for this type of coupled system. In (a), the system was prepared at resonance, $\Delta_0 = 0$, while in (b) the cavity was red detuned with respect to the cavity mode by $\Delta_0 = 0.33$ meV. Schematics

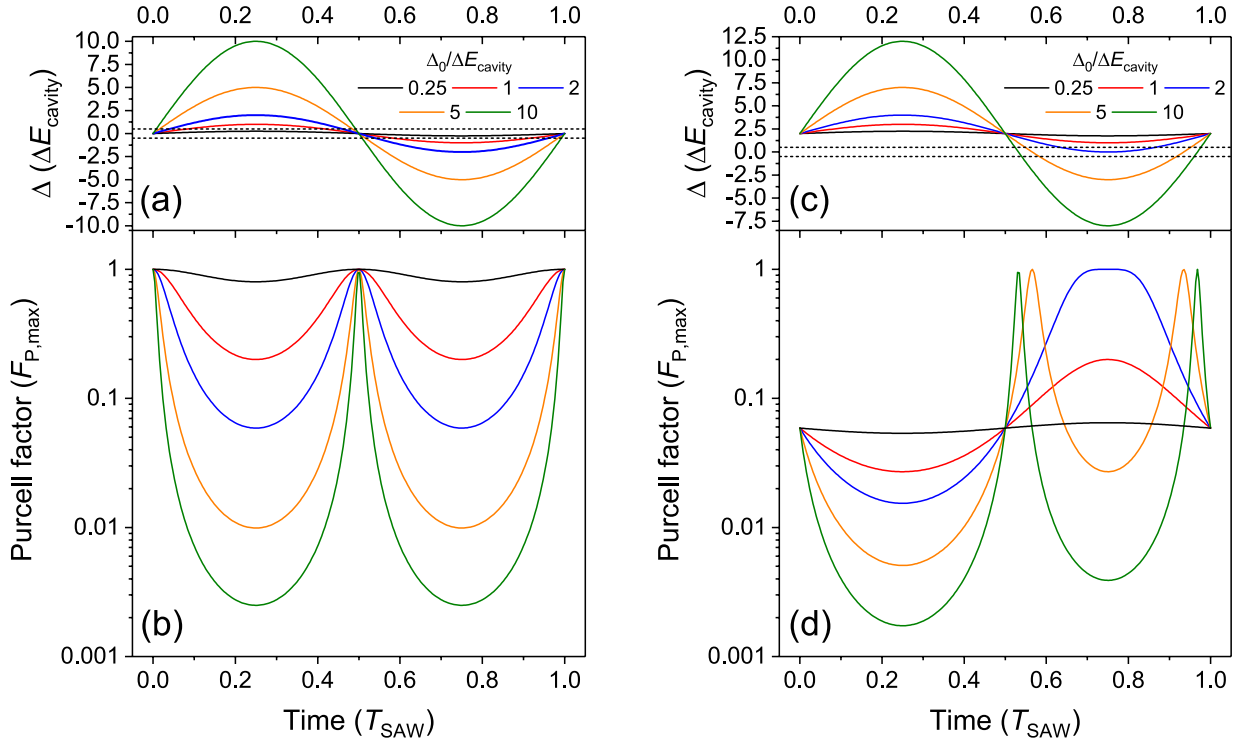

Figure 25. Calculated modulation of QD-cavity detuning and resulting modulation of the Purcell factor for $\Delta_0 = 0$ (a) and (b) and $\Delta_0 = 2\Delta E_{cavity}$ (c) and (d).

of the corresponding spectral modulations are plotted in figures 24(c) and (d). These schematics indicate that resonances are expected at well-defined times during the acoustic cycle. At these times, the emission from the system is expected to be enhanced by the Purcell-effect, while for all other times, a pronounced suppression should be observable. The predicted behavior is nicely reproduced in the experimental data [126]. Taking for instance the data in figure 24(a) at $\Delta_0 = 0$, pronounced maximum emission is observed close to the node of the oscillations of the QD (white dashed guide for the eye) and nanocavity (black dashed guide for the eye). This maximum is delayed in figure 24(b) and occurs close to the maximum of the modulation at which the dynamic component compensates the static detuning of $\Delta_0 = 0.33$ meV. A closer examination of the experimental data reveals deviations from this basic model: the maximum emission occurs at slightly earlier times compared to the expected resonance. In addition, only where the cavity is tuned into resonance from the low energy side, an enhancement of the emission is observed. Both effects are consistent with non-resonant coupling mechanisms studied in detail for quasi-statically tuned systems [217–220], and remain an area of active research.

The Purcell factor modulation of this acoustically driven QD-nanocavity system can be modeled by introducing the time dependent detuning of equation (7) into (5). The results of this model for $\Delta_0 = 0$ and $\Delta_0 = 2\Delta E_{cavity}$ are shown in figures 25(a) and (b), and 25(c) and (d), respectively. $\Delta E_{QD-NC}(t)$, normalized to the cavity linewidth ΔE_{cavity} for different tuning amplitudes Δ and two selected values of the static detuning are plotted in the upper panels (a) and (c). In these plots, the cavity FWHM, ΔE_{cavity}, is marked by a horizontal dashed line. The lower panels (b) and (d) summarize the expected dynamic modulation of the Purcell factor $F_P(t)$, normalized to $F_{p,max}$. These calculations nicely show the strong suppression of the emission by more than two orders of magnitude for moderate tuning amplitude of $\Delta = 10\Delta E_{cavity}$. For $\Delta_0 = 0$ the modulation arises from a suppression of the radiative rate for time intervals increasing with Δ. For $\Delta_0 = 2\Delta E_{cavity}$, the weakly modulated system $\Delta = \Delta E_{cavity}$, exhibits a moderate, yet modulated $F_p < F_{p,max}$. For $\Delta > 2\Delta E_{cavity}$, $F_{p,max}$ is reached and with increasing Δ, a pronounced modulation develops. In contrast to figure 25(b), the temporal modulation remains asymmetric due to the finite static detuning. We note that this basic model predicts two distinct maxima at which the Purcell effect triggers emission from the QD. Thus, it cannot explain the experimentally observed absence of the second emission.

Since the observed emission stems from a single QD, photon anti-bunching is expected. This generation of non-classical light can be confirmed by measuring the second order correlation function $g^{(2)}(\tau)$. The results of such an experiment are presented in figure 26. In figure 26(a), the measured $g^{(2)}(\tau)$ is plotted over a long time interval of $|\tau| > 6.5\mu$s. In this data, the repetition period of the applied acoustic pulses and the time interval in which the laser pulses are activated are clearly resolved. Figure 26(b) shows a zoom in to the central part $-42\,\text{ns} < \tau < 42\,\text{ns}$ around $\tau = 0$. On these short timescales, the periodicity of the individual laser pulses gives rise to the observed peaks of $g^{(2)}(\tau)$. Most importantly, the center peak at $\tau = 0$ is absent. This observation of $g^{(2)}(0) \approx 0$ is

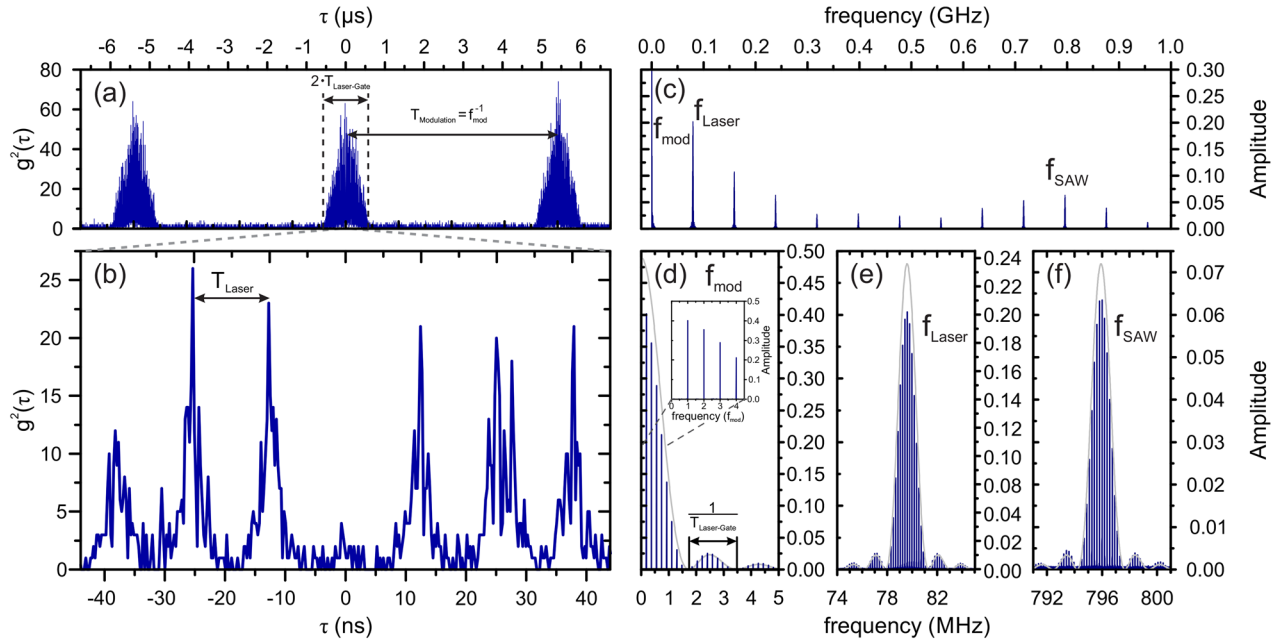

Figure 26. SAW regulated single photon emission. (a) Measured $g^{(2)}$ plotted over a $\geqslant 13\mu$s time interval demonstrating that correlations are in fact detected only when the laser is active. (b) Zoom to the center $\pm$ 13μs interval showing clear anti-bunching due to single photon emission and additional clear modulations. (c) Fourier transform of the measured $g^{(2)}$ in a frequency range 0–1 GHz. (d)–(f) Zoom to characteristic frequencies involved in the experiment. Reprinted with permission from [126]. Copyright 2016, AIP Publishing LLC.

a clear fingerprint of single photon emission. Furthermore, also on these short timescales, a further short period modulation of $g^{(2)}(\tau)$ is resolved. This modulation arises from the acoustic modulation. All frequency components involved in the experiment, can be identified in a Fourier analysis of the measured $g^{(2)}(\tau)$. Figure 26(c) depicts an overview spectrum. In this spectrum, the three distinct modulation frequencies, the acoustic and laser pulse rate and the SAW frequency can be identified. In figures 26(d)–(f), the spectrum around these characteristic frequencies (blue line) is compared to that expected from the electrical modulation (grey line). This good agreement and the clearly resolved frequency components confirm the high precision regulation of the single photon emission from our acoustically driven coupled QD-nanocavity system.

6.2.3. Acoustically-driven entangling quantum gate in a QD nanocavity system. All experimental work discussed so far has been restricted to the dissipation dominated regime of weak light–matter interaction, in which the photon loss is the dominant rate. In the regime of strong light–matter coupling, the vacuum Rabi frequency exceeds all loss mechanisms and dressed polariton states are formed between photon(s) and exciton. This coupling is described by the Jaynes–Cummings (JC) model [74–76, 200, 221–223].

Figure 27(a) depicts the solution of the energy eigenvalues as a function of detuning $(\Delta E_{QD-NC}(t))$ of the JC model for coupled QD–nanocavity system. To be more precise, the solution shown for the detuning being varied with a constant rate $\Delta E_{QD-NC}(t) = v \cdot t$. For small tuning rates $v, \hbar v \ll g^2$, the states evolve adiabatically, shown in solid lines in figure 27(a): as the system is swept through the avoided crossing, the state in which the QD is in its excited state and the cavity is not occupied by a photon ($|1_X, 0_\gamma\rangle$, red line) evolves into the state in which the QD is in its ground state and the cavity is occupied by a single photon ($|0_X, 1_\gamma\rangle$, black line) and vice versa. This type of coupled system can be also driven non-adiabatically thus inducing Landau–Zener (LZ) transitions [225–228] for sufficiently large tuning rates v. Here, the initial states remain partially occupied. The probability of this diabatic process is given by the famous LZ formula:

$$P_{LZ} = 1 - \exp\left(-2\pi g^2/\hbar v\right). \tag{8}$$

For $P_{LZ} \to 1$, i.e. $\hbar v \gg g^2$, the system is tuned along the diabatic states, preserving the occupation of the initial state. This process is shown in figure 27(b). For moderate v, $P_{LZ} = 0.5$ can be realized. In this regime, an initial product state can be transformed into a maximally entangled state. For instance, the product state $|1_X, 0_\gamma\rangle$ can be driven into the Bell state $\Psi^+ \frac{1}{\sqrt{2}} |1_X, 0_\gamma + 0_X, 1_\gamma\rangle$. This scheme was introduced in the field of solid state quantum information processing in a proposal for superconducting circuit quantum electrodynamics [229]. SAW and dynamic acoustic fields in general are also well suited to the implementation of dynamic tuning. For a sinusoidal SAW, $v = f_{SAW} \cdot A_{SAW}$. Blattmann *et al* conducted a theoretical study on entangling quantum gates driven by SAWs [224]. In their study, they assumed a PCM defect nanocavity and a strong QD coupling to its optical mode. Their model system builds on the experimental work discussed above [126] and the regime of strong light–matter interaction, established previously for adiabatically tuned systems [74, 76, 211, 223, 230]. Most importantly, they restrict their modeling exclusively to experimentally demonstrated system parameters. The generated entangled states persist on timescales limited by the fastest relaxation rate of the system, which is that of the

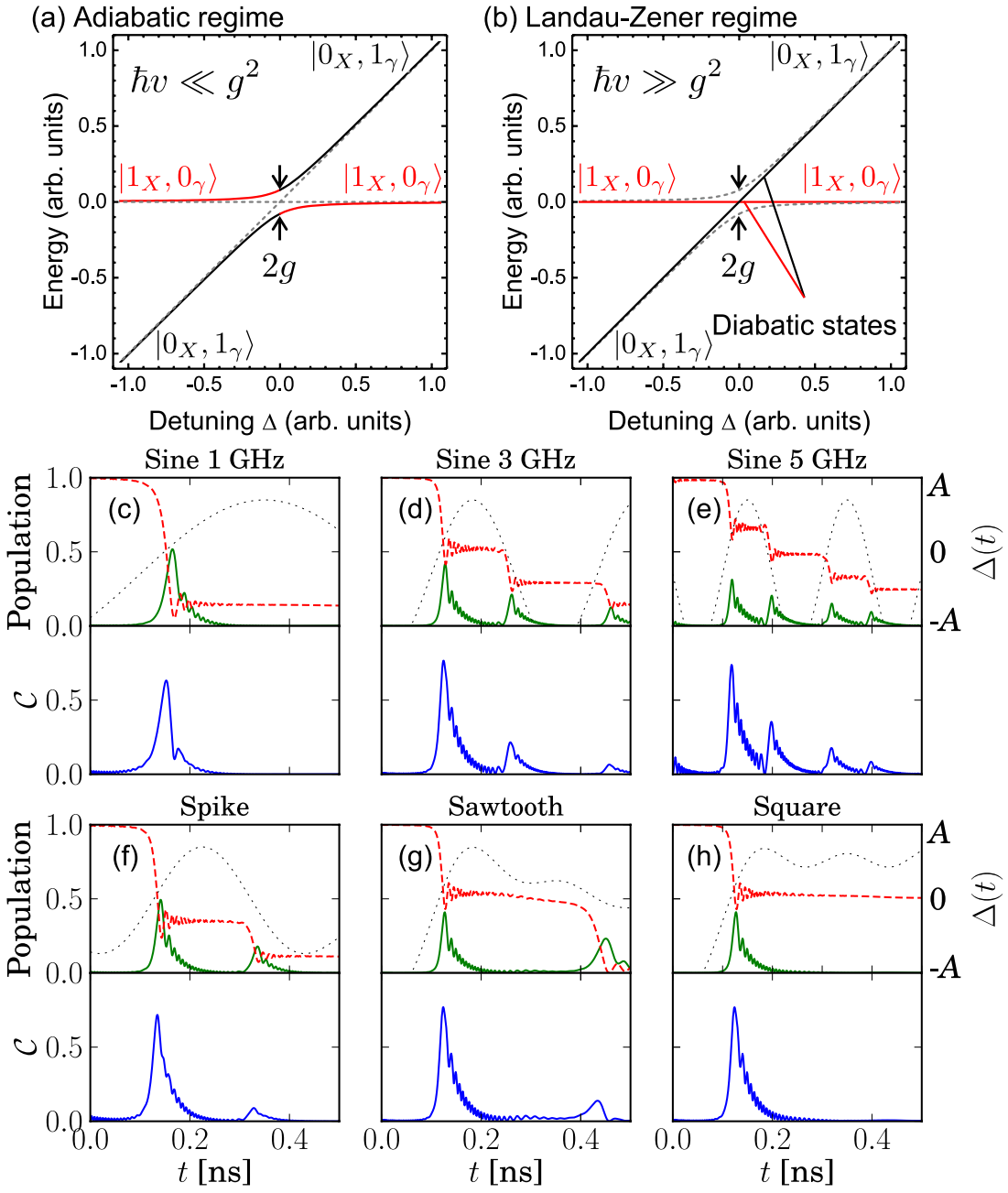

Figure 27. SAW-driven entanglement generation. (a) Energy spectrum of a coupled QD-nanocavity system under slow, adiabatic driving showing the characteristic avoided crossing between the exciton $|1_X, 0_\gamma\rangle$ and single photon $|0_X, 1_\gamma\rangle$ states. (b) Under fast driving, the time evolution occurs along the diabatic states giving rise to Landau–Zener tunneling. (c)–(h) LZ entanglement dynamics for sine wave SAWs with frequencies 1 GHz (c), 3 GHz (d), and 5 GHz (e), as well as for a spike (f), a sawtooth (g), and a square (h), each with fundamental frequency 1 GHz. The cavity–dot coupling is g = 35 μeV, while the static detuning $\Delta_0 = 0.3$ meV is modulated with an amplitude A = 1 meV. Upper panels: population of the states $|1_X, 0_\gamma\rangle$ (red solid line) and $|0_X, 1_\gamma\rangle$ (green dashed line). The dotted line visualizes the course of the detuning $\Delta E_{QD-NC} = \Delta_0 + \Delta \cdot \sin \omega_{SAW} t$. Lower panels: cavity–dot entanglement in terms of the concurrence $\mathcal{C}$. Reprinted figure with permission from [224], Copyright 2014 by the American Physical Society.

photon loss from the cavity. The performance of the proposed entangling quantum gate can be improved by employing the Fourier-synthesized acoustic waves realized experimentally by Schülein *et al* shortly after [173]. Figures 27(c)–(h) show key results of Blattmann *et al* [224]. In the upper panels, the calculated time evolutions of the populations of states $|1_X, 0_\gamma\rangle$ (red line) and $|0_X, 1_\gamma\rangle$ (green line) are plotted for a static detuning of $\Delta_0 = 0.3$ meV and a tuning amplitude of $\Delta = 1$ meV. $\Delta(t)$ is plotted as a reference (grey dashed line). The system evolution starts in initial state $|1_X, 0_\gamma\rangle$ and is tuned into resonance at $t_0 = 0.5$ ns. At resonance, the population is transferred from state $|1_X, 0_\gamma\rangle$ to state $|0_X, 1_\gamma\rangle$. As expected, this transfer clearly depends on the chosen frequency and waveform. Moreover, the population of state $|0_X, 1_\gamma\rangle$ rapidly decays, since the underlying photon loss is the dominant loss channel of the system. This rapid decay has a pronounced impact on the generated entanglement. The lower panels of figures 27(c)–(h) show the concurrence $\mathcal{C}$, the entanglement measure employed.

$\mathcal{C} > 0.8$ are predicted from these calculations, particularly for Fourier-synthesized waveforms. For all frequencies and waveforms, the persistence time of $\mathcal{C}$ is again limited by the photon loss rate. For a full analysis of various system parameters, the reader is referred to the original article [224]. As noted above, this theoretical work is exclusively based on experimentally demonstrated system parameters. These calculations show that entangled exciton–photon states can in fact be generated by their scheme for f_{SAW} in the low gigahertz regime.

6.3. Future directions

The membranes used in the experiments discussed above have been optimized with regard to their photonic properties. In the field of integrated optomechanics, membrane-based optomechanical or phoXonic crystals are widely studied and controlled down to the single phonon regime [231–237]. Also, initial experiments have demonstrated the mutual coupling of coherent elastic and optical waves in these devices [238, 239]. By deliberately enhancing or suppressing the interactions between light (photons), sound (phonons) and matter (excitons), fully fledged coherent hybrid optomechanics can be established [240, 241]. This tripartite system enables coupling between the three 'elementary excitations' in condensed matter, electrons, photons and phonons, ultimately in the resolved sideband regime.

Thus, interfacing QDs or other quantum emitters on this platform is an extremely tantalizing goal within and beyond the emerging fields of nanophononics and optomechanics [242, 243], nano-opto-electro-mechanics [244] and SAW quantum acoustics [97]. We note that the concepts presented here are at the heart of a myriad of activities researching hybrid mechanical quantum systems. Even in the field of SAWs alone, strong coupling regime of cavity quantum acoustodynamics [245, 246] has been reported. In addition, recent preprints have appeared on the quantum control of a SAW resonator using a superconducting artificial atom [247], and coherent mechanical control of a single spin of a quantum emitter in a phononic resonator [248]. These potentially landmark works, reported over just a couple of months, underline the large momentum in this dynamic field of research.

Acknowledgments

We wish to thank Achim Wixforth for his continuous support. The work in Augsburg has been conducted by a team of highly motivated students (in alphabetical order), Daniel Fuhrmann, Michael Heigl, Stephan Kapfinger, Florian Knall, Emeline Nysten, Jens Pustiowski, Florian Schülein and Stefan Völk, who all made invaluable contributions to the experimental work presented here. For all this work, we were able to build on excellent sample material provided by Gerhard Abstreiter, Max Bichler, Jonathan Finley, Michael Kaniber, Gregor Koblmüller and Kai Müller, Dirk Reuter and Andreas Wieck, Dirk Bouwmeester and Pierre Petroff, and Paola Atkinson, Armando Rastelli, Oliver Schmidt and Eugenio Zallo. We acknowledge invaluable theoretical support by Peter Hänggi, Sigmund Kohler and Ralf Blattmann.

Funding

This work was supported by the Deutsche Forschungsgemeinschaft (DFG) via the Emmy Noether Program (KR3790/2-1) and Sonderforschungsbereich SFB 631, the Bavaria-California Techology Center (BaCaTeC), the Bayerische Forschungsstiftung and the Cluster of Excellence 'Nanosystems Initiative Munich' (NIM).

ORCID iDs

Hubert J Krenner https://orcid.org/0000-0002-0696-456X

References

[1] Ladd T D, Jelezko F, Laflamme R, Nakamura Y, Monroe C and O'Brien J L 2010 Quantum computers *Nature* **464** 45–53
[2] Awschalom D D, Bassett L C, Dzurak A S, Hu E L and Petta J R 2013 Quantum spintronics: engineering and manipulating atom-like spins in semiconductors *Science* **339** 1174–9
[3] Tillmann M, Dakić B, Heilmann R, Nolte S, Szameit A and Walther P 2013 Experimental boson sampling *Nat. Photonics.* **7** 540–4
[4] Georgescu I M, Ashhab S and Nori F 2014 Quantum simulation *Rev. Mod. Phys.* **86** 153–85
[5] Hensen B *et al* 2015 Loophole-free Bell inequality violation using electron spins separated by 1.3 kilometres *Nature* **526** 682–6
[6] Kurizki G, Bertet P, Kubo Y, Mølmer K, Petrosyan D, Rabl P and Schmiedmayer J 2015 Quantum technologies with hybrid systems *Proc. Natl Acad. Sci. USA* **112** 3866–73
[7] Cirac J I and Zoller P 1995 Quantum computations with cold trapped ions *Phys. Rev. Lett.* **74** 4091–4
[8] Yeo I *et al* 2013 Strain-mediated coupling in a quantum dot–mechanical oscillator hybrid system *Nat. Nanotechnol.* **9** 106–10
[9] Pigeau B, Rohr S, Mercier de Lépinay L, Gloppe A, Jacques V and Arcizet O 2015 Observation of a phononic Mollow triplet in a multimode hybrid spin-nanomechanical system *Nat. Commun.* **6** 8603
[10] Barfuss A, Teissier J, Neu E, Nunnenkamp A and Maletinsky P 2015 Strong mechanical driving of a single electron spin *Nat. Phys.* **11** 820–4
[11] Bell D L T and Li R C M 1976 Surface-acoustic-wave resonators *Proc. IEEE* **64** 711–21
[12] Datta S 1986 *Surface Acoustic Wave Devices* (Englewood Cliffs, NJ: Prentice Hall)
[13] Campbell C 1989 *Surface Acoustic Wave Devices and Their Signal Processing Applications* (Amsterdam: Elsevier)
[14] Golter D A, Oo T, Amezcua M, Stewart K A and Wang H 2016 Optomechanical quantum control of a nitrogen-vacancy center in diamond *Phys. Rev. Lett.* **116** 143602
[15] Golter D A, Oo T, Amezcua M, Lekavicius I, Stewart K A and Wang H 2016 Coupling a surface acoustic wave to an electron spin in diamond via a dark state *Phys. Rev.* X **6** 041060
[16] Fletcher N E, Ebbecke J, Janssen T J B M, Ahlers F J, Pepper M, Beere H E and Ritchie D A 2003 Quantized acoustoelectric current transport through a static quantum dot using a surface acoustic wave *Phys. Rev.* B **68** 245310
[17] Naber W J M, Fujisawa T, Liu H W and van der Wiel W G 2006 Surface-acoustic-wave-induced transport in a double quantum dot *Phys. Rev. Lett.* **96** 136807

[18] Giavaras G 2010 Two-electron correlations and the acoustoelectric current through a quantum dot *Phys. Rev.* B **81** 073302

[19] McNeil R P G, Kataoka M, Ford C J B, Barnes C H W, Anderson D, Jones G A C, Farrer I and Ritchie D A 2011 On-demand single-electron transfer between distant quantum dots *Nature* **477** 439–42

[20] Hermelin S, Takada S, Yamamoto M, Tarucha S, Wieck A D, Saminadayar L, Bäuerle C and Meunier T 2011 Electrons surfing on a sound wave as a platform for quantum optics with flying electrons *Nature* **477** 435–8

[21] Guo Y-N *et al* 2013 Phase separation induced by Au catalysts in ternary InGaAs nanowires *Nano Lett.* **13** 643–50

[22] Bertrand B, Hermelin S, Takada S, Yamamoto M, Tarucha S, Ludwig A, Wieck A D, Bäuerle C and Meunier T 2016 Fast spin information transfer between distant quantum dots using individual electrons *Nat. Nanotechnol.* **11** 672–6

[23] Bäuerle C, Christian Glattli D, Meunier T, Portier F, Roche P, Roulleau P, Takada S and Waintal X 2018 Coherent control of single electrons: a review of current progress *Rep. Prog. Phys.* **81** 056503

[24] Ford C J B 2017 Transporting and manipulating single electrons in surface-acoustic-wave minima *Phys. Status Solidi* **254** 1600658

[25] Bayer M, Stern O, Hawrylak P, Fafard S and Forchel A 2000 Hidden symmetries in the energy levels of excitonic 'artificial atoms' *Nature* **405** 923–6

[26] Gywat O, Krenner H J and Berezovsky J 2010 *Spins in Optically Active Quantum Dots: Concepts and Methods* (Berlin: Wiley)

[27] Leonard D, Krishnamurthy M, Reaves C M, Denbaars S P and Petroff P M 1993 Direct formation of quantum-sized dots from uniform coherent islands of InGaAs on GaAs surfaces *Appl. Phys. Lett.* **63** 3203–5

[28] Michler P, Kiraz A, Becher C, Schoenfeld W V, Petroff P M, Zhang L, Hu E and Imamoğlu A 2000 A quantum dot single-photon turnstile device *Science* **290** 2282–5

[29] Lounis B and Orrit M 2005 Single-photon sources *Rep. Prog. Phys.* **68** 1129–79

[30] Shields A J 2007 Semiconductor quantum light sources *Nat. Photonics* **1** 215–23

[31] He Y-M, He Y, Wei Y-J, Wu D, Atatüre M, Schneider C, Höfling S, Kamp M, Lu C-Y and Pan J-W 2013 On-demand semiconductor single-photon source with near-unity indistinguishability *Nat. Nanotechnol.* **8** 213–7

[32] Gschrey M *et al* 2015 Highly indistinguishable photons from deterministic quantum-dot microlenses utilizing three-dimensional *in situ* electron-beam lithography *Nat. Commun.* **6** 7662

[33] Somaschi N *et al* 2016 Near-optimal single-photon sources in the solid state *Nat. Photonics* **10** 340–5

[34] Senellart P, Solomon G and White A 2017 High-performance semiconductor quantum-dot single-photon sources *Nat. Nanotechnol.* **12** 1026–39

[35] Stievater T H, Li X, Steel D G, Gammon D, Katzer D S, Park D, Piermarocchi C and Sham L J 2001 Rabi oscillations of excitons in single quantum dots *Phys. Rev. Lett.* **87** 133603

[36] Zrenner A, Beham E, Stufler S, Findeis F, Bichler M and Abstreiter G 2002 Coherent properties of a two-level system based on a quantum-dot photodiode *Nature* **418** 612–4

[37] Bonadeo N H, Erland J, Gammon D, Park D, Katzer D S and Steel D G 1998 Coherent optical control of the quantum state of a single quantum dot *Science* **282** 1473–6

[38] Stufler S, Ester P, Zrenner A and Bichler M 2005 Quantum optical properties of a single $In_xGa_{1-x}As$-GaAs quantum dot two-level system *Phys. Rev.* B **72** 121301

[39] Krenner H J, Stufler S, Sabathil M, Clark E C, Ester P, Bichler M, Abstreiter G, Finley J J and Zrenner A 2005 Recent advances in exciton-based quantum information processing in quantum dot nanostructures *New J. Phys.* **7** 184

[40] Stufler S, Ester P, Zrenner A and Bichler M 2006 Ramsey fringes in an electric-field-tunable quantum dot system *Phys. Rev. Lett.* **96** 037402

[41] Autler S H and Townes C H 1955 Stark effect in rapidly varying fields *Phys. Rev.* **100** 703–22

[42] Xu X, Sun B, Berman P R, Steel D G, Bracker A S, Gammon D and Sham L J 2007 Coherent optical spectroscopy of a strongly driven quantum dot *Science* **317** 929–32

[43] Mollow B R 1969 Power spectrum of light scattered by two-level systems *Phys. Rev.* **188** 1969–75

[44] Ates S, Ulrich S M, Reitzenstein S, Löffler A, Forchel A and Michler P 2009 Post-selected indistinguishable photons from the resonance fluorescence of a single quantum dot in a microcavity *Phys. Rev. Lett.* **103** 167402

[45] Flagg E B, Muller A, Robertson J W, Founta S, Deppe D G, Xiao M, Ma W, Salamo G J and Shih C K 2009 Resonantly driven coherent oscillations in a solid-state quantum emitter *Nat. Phys.* **5** 203–7

[46] Nick Vamivakas A, Zhao Y, Lu C-Y and Atatüre M 2009 Spin-resolved quantum-dot resonance fluorescence *Nat. Phys.* **5** 198–202

[47] Drexler H, Leonard D, Hansen W, Kotthaus J P and Petroff P M 1994 Spectroscopy of quantum levels in charge-tunable InGaAs quantum dots *Phys. Rev. Lett.* **73** 2252–5

[48] Warburton R J, Schäflein C, Haft D, Bickel F, Lorke A, Karrai K, Garcia J M, Schoenfeld W and Petroff P M 2000 Optical emission from a charge-tunable quantum ring *Nature* **405** 926–9

[49] Fry P W *et al* 2000 Inverted electron-hole alignment in InAs-GaAs self-assembled quantum dots *Phys. Rev. Lett.* **84** 733–6

[50] Kroutvar M, Ducommun Y, Heiss D, Bichler M, Schuh D, Abstreiter G and Finley J J 2004 Optically programmable electron spin memory using semiconductor quantum dots *Nature* **432** 81–4

[51] Yuan Z, Kardynal B E, Stevenson R M, Shields A J, Lobo C J, Cooper K, Beattie N S, Ritchie D A and Pepper M 2002 Electrically driven single-photon source *Science* **295** 102–5

[52] Salter C L, Stevenson R M, Farrer I, Nicoll C A, Ritchie D A and Shields A J 2010 An entangled-light-emitting diode *Nature* **465** 594–7

[53] Zhang J, Wildmann J S, Ding F, Trotta R, Huo Y, Zallo E, Huber D, Rastelli A and Schmidt O G 2015 High yield and ultrafast sources of electrically triggered entangled-photon pairs based on strain-tunable quantum dots *Nat. Commun.* **6** 10067

[54] Findeis F, Baier M, Beham E, Zrenner A and Abstreiter G 2001 Photocurrent and photoluminescence of a single self-assembled quantum dot in electric fields *Appl. Phys. Lett.* **78** 2958–60

[55] Müller K, Kaldewey T, Ripszam R, Wildmann J S, Bechtold A, Bichler M, Koblmüller G, Abstreiter G and Finley J J 2013 All optical quantum control of a spin-quantum state and ultrafast transduction into an electric current *Sci. Rep.* **3** 1906

[56] Müller K *et al* 2012 High-fidelity optical preparation and coherent Larmor precession of a single hole in an (In,Ga)As quantum dot molecule *Phys. Rev.* B **85** 241306

[57] Müller K *et al* 2013 Probing ultrafast carrier tunneling dynamics in individual quantum dots and molecules *Ann. Phys.* **525** 49–58

[58] Bayer M, Hawrylak P, Hinzer K, Fafard S, Korkusinski M, Wasilwski Z R, Stern O and Forchel A 2001 Coupling and

entangling of quantum states in quantum dot molecules *Science* **291** 451–3
[59] Solomon G S, Trezza J A, Marshall A F and Harris J S Jr 1996 Vertically aligned and electronically coupled growth induced InAs Islands in GaAs *Phys. Rev. Lett.* **76** 952–5
[60] Krenner H J, Sabathil M, Clark E C, Kress A, Schuh D, Bichler M, Abstreiter G and Finley J J 2005 Direct observation of controlled coupling in an individual quantum dot molecule *Phys. Rev. Lett.* **94** 57402
[61] Stinaff E A, Scheibner M, Bracker A S, Ponomarev I V, Korenev V L, Ware M E, Doty M F, Reinecke T L and Gammon D 2006 Optical signatures of coupled quantum dots *Science* **311** 636–9
[62] Krenner H J, Clark E C, Nakaoka T, Bichler M, Scheurer C, Abstreiter G and Finley J J 2006 Optically probing spin and charge interactions in a tunable artificial molecule *Phys. Rev. Lett.* **97** 76403
[63] Robledo L, Elzerman J, Jundt G, Atature M, Hogele A, Falt S and Imamoglu A 2008 Conditional dynamics of interacting quantum dots *Science* **320** 772–5
[64] Kim D, Carter S G, Greilich A, Bracker A S and Gammon D 2010 Ultrafast optical control of entanglement between two quantum-dot spins *Nat. Phys.* **7** 223–9
[65] Greilich A, Carter S G, Kim D, Bracker A S and Gammon D 2011 Optical control of one and two hole spins in interacting quantum dots *Nat. Photonics* **5** 702–8
[66] Lee H, Johnson J A, Speck J S and Petroff P M 2000 Controlled ordering and positioning of InAs self-assembled quantum dots *J. Vac. Sci. Technol.* B **18** 2193
[67] Mehta M, Reuter D, Melnikov A, Wieck A D and Remhof A 2007 Focused ion beam implantation induced site-selective growth of InAs quantum dots *Appl. Phys. Lett.* **91** 123108
[68] Schneider C, Heindel T, Huggenberger A, Weinmann P, Kistner C, Kamp M, Reitzenstein S, Höfling S and Forchel A 2009 Single photon emission from a site-controlled quantum dot-micropillar cavity system *Appl. Phys. Lett.* **94** 111111
[69] Songmuang R, Kiravittaya S and Schmidt O G 2003 Formation of lateral quantum dot molecules around self-assembled nanoholes *Appl. Phys. Lett.* **82** 2892–4
[70] Krause B, Metzger T H, Rastelli A, Songmuang R, Kiravittaya S and Schmidt O G 2005 Shape, strain, and ordering of lateral InAs quantum dot molecules *Phys. Rev.* B **72** 85339
[71] Beirne G J, Hermannstädter C, Wang L, Rastelli A, Schmidt O G and Michler P 2006 Quantum light emission of two lateral tunnel-coupled (In,Ga)As/GaAs quantum dots controlled by a tunable static electric field *Phys. Rev. Lett.* **96** 137401
[72] Purcell E M 1946 Spontaneous emission probabilities at radio frequencies *Phys. Rev.* **69** 681
[73] Gérard J, Sermage B, Gayral B, Legrand B, Costard E and Thierry-Mieg V 1998 Enhanced spontaneous emission by quantum boxes in a monolithic optical microcavity *Phys. Rev. Lett.* **81** 1110–3
[74] Yoshie T, Scherer A, Hendrickson J, Khitrova G, Gibbs H M, Rupper G, Ell C, Shchekin O B and Deppe D G 2004 Vacuum Rabi splitting with a single quantum dot in a photonic crystal nanocavity *Nature* **432** 200–3
[75] Reithmaier J P, Sek G, Loffler A, Hofmann C, Kuhn S, Reitzenstein S, Keldysh L V, Kulakovskii V D, Reinecke T L and Forchel A 2004 Strong coupling in a single quantum dot-semiconductor microcavity system *Nature* **432** 197–200
[76] Hennessy K, Badolato A, Winger M, Gerace D, Atatüre M, Gulde S, Fält S, Hu E L and Imamoğlu A 2007 Quantum nature of a strongly coupled single quantum dot–cavity system *Nature* **445** 896–9
[77] Volz T, Reinhard A, Winger M, Badolato A, Hennessy K J, Hu E L and Imamoğlu A 2012 Ultrafast all-optical switching by single photons *Nat. Photonics* **6** 607–11
[78] Bockelmann U and Bastard G 1990 Phonon scattering and energy relaxation in two-, one-, and zero-dimensional electron gases *Phys. Rev.* B **42** 8947–51
[79] Benisty H, Sotomayor-Torrès C M and Weisbuch C 1991 Intrinsic mechanism for the poor luminescence properties of quantum-box systems *Phys. Rev.* B **44** 10945–8
[80] Sugawara M, Mukai K and Shoji H 1997 Effect of phonon bottleneck on quantum-dot laser performance *Appl. Phys. Lett.* **71** 2791–3
[81] Ohnesorge B, Albrecht M, Oshinowo J, Forchel A and Arakawa Y 1996 Rapid carrier relaxation in self-assembled $InxGa_{1-x}As$/GaAs quantum dots *Phys. Rev.* B **54** 11532–8
[82] Heitz R, Veit M, Ledentsov N, Hoffmann A, Bimberg D, Ustinov V, Kop'ev P and Alferov Z 1997 Energy relaxation by multiphonon processes in InAs/GaAs quantum dots *Phys. Rev.* B **56** 10435–45
[83] Heitz R, Kalburge A, Xie Q, Grundmann M, Chen P, Hoffmann A, Madhukar A and Bimberg D 1998 Excited states and energy relaxation in stacked InAs/GaAs quantum dots *Phys. Rev.* B **57** 9050–60
[84] Trumm S, Wesseli M, Krenner H J, Schuh D, Bichler M, Finley J J and Betz M 2005 Spin-preserving ultrafast carrier capture and relaxation in InGaAs quantum dots *Appl. Phys. Lett.* **87** 153113
[85] Heitz R, Born H, Guffarth F, Stier O, Schliwa A, Hoffmann A and Bimberg D 2001 Existence of a phonon bottleneck for excitons in quantum dots *Phys. Rev.* B **64** 241305
[86] Urayama J, Norris T B, Singh J and Bhattacharya P 2001 Observation of phonon bottleneck in quantum dot electronic relaxation *Phys. Rev. Lett.* **86** 4930–3
[87] Ortner G, Oulton R, Kurtze H, Schwab M, Yakovlev D R, Bayer M, Fafard S, Wasilewski Z and Hawrylak P 2005 Energy relaxation of electrons in InAs/GaAs quantum dot molecules *Phys. Rev.* B **72** 165353
[88] Nakaoka T, Clark E C, Krenner H J, Sabathil M, Bichler M, Arakawa Y, Abstreiter G and Finley J J 2006 Direct observation of acoustic phonon mediated relaxation between coupled exciton states in a single quantum dot molecule *Phys. Rev.* B **74** 121305
[89] Sanguinetti S, Guzzi M, Grilli E, Gurioli M, Seravalli L, Frigeri P, Franchi S, Capizzi M, Mazzuccato S and Polimeni A 2008 Effective phonon bottleneck in the carrier thermalization of InAs/GaAs quantum dots *Phys. Rev.* B **78** 085313
[90] Krummheuer B, Axt V M and Kuhn T 2002 Theory of pure dephasing and the resulting absorption line shape in semiconductor quantum dots *Phys. Rev.* B **65** 195313
[91] Muljarov E A and Zimmermann R 2004 Dephasing in quantum dots: quadratic coupling to acoustic phonons *Phys. Rev. Lett.* **93** 237401
[92] Ramsay A J, Gopal A V, Gauger E M, Nazir A, Lovett B W, Fox A M and Skolnick M S 2010 Damping of exciton rabi rotations by acoustic phonons in optically excited InGaAs/GaAs quantum dots *Phys. Rev. Lett.* **104** 017402
[93] Vagov A, Croitoru M D, Axt V M, Kuhn T and Peeters F M 2007 Nonmonotonic field dependence of damping and reappearance of Rabi oscillations in quantum dots *Phys. Rev. Lett.* **98** 227403
[94] Lüker S, Gawarecki K, Reiter D E, Grodecka-Grad A, Axt V M, Machnikowski P and Kuhn T 2012 Influence of acoustic phonons on the optical control of quantum dots driven by adiabatic rapid passage *Phys. Rev.* B **85** 121302
[95] Liu F, Martins L M P, Brash A J, Barth A M, Quilter J H, Axt V M, Skolnick M S and Fox A M 2016 Ultrafast depopulation of a quantum dot by LA-phonon-assisted stimulated emission *Phys. Rev.* B **93** 161407

[96] Gustafsson M V, Aref T, Kockum A F, Ekstrom M K, Johansson G and Delsing P 2014 Propagating phonons coupled to an artificial atom *Science* **346** 207–11

[97] Schuetz M J A, Kessler E M, Giedke G, Vandersypen L M K, Lukin M D and Cirac J I 2015 Universal quantum transducers based on surface acoustic waves *Phys. Rev.* X **5** 031031

[98] Chu Y, Kharel P, Renninger W H, Burkhart L D, Frunzio L, Rakich P T and Schoelkopf R J 2017 Quantum acoustics with superconducting qubits *Science* **358** 199–202

[99] Manenti R, Kockum A F, Patterson A, Behrle T, Rahamim J, Tancredi G, Nori F and Leek P J 2017 Circuit quantum acoustodynamics with surface acoustic waves *Nat. Commun.* **8** 975

[100] Khaetskii A V and Nazarov Y V 2001 Spin-flip transitions between Zeeman sublevels in semiconductor quantum dots *Phys. Rev.* B **64** 125316

[101] Woods L M, Reinecke T L and Lyanda-Geller Y 2002 Spin relaxation in quantum dots *Phys. Rev.* B **66** 161318

[102] Golovach V N, Khaetskii A and Loss D 2004 Phonon-induced decay of the electron spin in quantum dots *Phys. Rev. Lett.* **93** 16601

[103] Thomsen C, Grahn H T, Maris H J and Tauc J 1986 Surface generation and detection of phonons by picosecond light pulses *Phys. Rev.* B **34** 4129–38

[104] Wright O B, Perrin B, Matsuda O and Gusev V E 2001 Ultrafast carrier diffusion in gallium arsenide probed with picosecond acoustic pulses *Phys. Rev.* B **64** 081202

[105] Akimov A V, Tanaka Y, Pevtsov A B, Kaplan S F, Golubev V G, Tamura S, Yakovlev D R and Bayer M 2008 Hypersonic modulation of light in three-dimensional photonic and phononic band-gap materials *Phys. Rev. Lett.* **101** 033902

[106] Fainstein A, Lanzillotti-Kimura N D, Jusserand B and Perrin B 2013 Strong optical-mechanical coupling in a vertical GaAs/AlAs microcavity for subterahertz phonons and near-infrared light *Phys. Rev. Lett.* **110** 037403

[107] Akimov A V, Poyser C L and Kent A J 2017 Review of microwave electro-phononics in semiconductor nanostructures *Semicond. Sci. Technol.* **32** 053003

[108] Brüggemann C, Akimov A V, Scherbakov A V, Bombeck M, Schneider C, Höfling S, Forchel A, Yakovlev D R and Bayer M 2011 Laser mode feeding by shaking quantum dots in a planar microcavity *Nat. Photonics* **6** 30–4

[109] Czerniuk T, Wigger D, Akimov A V, Schneider C, Kamp M, Höfling S, Yakovlev D R, Kuhn T, Reiter D E and Bayer M 2017 Picosecond control of quantum dot laser emission by coherent phonons *Phys. Rev. Lett.* **118** 133901

[110] Rayleigh L 1885 On waves propagated along the plane surface of an elastic solid *Proc. London Math. Soc.* **s1–17** 4–11

[111] Knuuttila J V, Tikka P T and Salomaa M M 2000 Scanning Michelson interferometer for imaging surface acoustic wave fields *Opt. Lett.* **25** 613

[112] de Lima M M Jr and Santos P V 2005 Modulation of photonic structures by surface acoustic waves *Rep. Prog. Phys.* **68** 1639–701

[113] Lew Yan Voon L C and Willatzen M 2011 Electromechanical phenomena in semiconductor nanostructures *J. Appl. Phys.* **109** 031101

[114] Völk S, Knall F, Schülein F J R, Truong T A, Kim H, Petroff P M, Wixforth A and Krenner H J 2011 Direct observation of dynamic surface acoustic wave controlled carrier injection into single quantum posts using phase-resolved optical spectroscopy *Appl. Phys. Lett.* **98** 23109

[115] Fuhrmann D A, Thon S M, Kim H, Bouwmeester D, Petroff P M, Wixforth A and Krenner H J 2011 Dynamic modulation of photonic crystal nanocavities using gigahertz acoustic phonons *Nat. Photonics* **5** 605–9

[116] Sogawa T, Sanada H, Gotoh H, Yamaguchi H, Miyashita S and Santos P V 2007 Photoluminescence dynamics of GaAs/AlAs quantum wells modulated by surface acoustic waves *Japan. J. Appl. Phys.* **46** L758–60

[117] Ruppert C, Förster F, Zrenner A, Kinzel J B, Wixforth A, Krenner H J and Betz M 2014 Radio frequency electromechanical control over a surface plasmon polariton coupler *ACS Photonics* **1** 91–5

[118] Weiß M, Hörner A L, Zallo E, Atkinson P, Rastelli A, Schmidt O G, Wixforth A and Krenner H J 2018 Multiharmonic frequency-chirped transducers for surface-acoustic-wave optomechanics *Phys. Rev. Appl.* **9** 014004

[119] Sauer W, Streibl M, Metzger T H, Haubrich A G C, Manus S, Wixforth A, Peisl J, Mazuelas A, Härtwig J and Baruchel J 1999 X-ray imaging and diffraction from surface phonons on GaAs *Appl. Phys. Lett.* **75** 1709–11

[120] Reusch T, Schülein F, Bömer C, Osterhoff M, Beerlink A, Krenner H J, Wixforth A and Salditt T 2013 Standing surface acoustic waves in $LiNbO_3$ studied by time resolved x-ray diffraction at Petra III *AIP Adv.* **3** 072127

[121] Nicolas J-D, Reusch T, Osterhoff M, Sprung M, Schülein F J R, Krenner H J, Wixforth A and Salditt T 2014 Time-resolved coherent x-ray diffraction imaging of surface acoustic waves *J. Appl. Crystallogr.* **47** 1596–605

[122] Reusch T, Schülein F J R, Nicolas J D, Osterhoff M, Beerlink A, Krenner H J, Müller M, Wixforth A and Salditt T 2014 Collective lipid bilayer dynamics excited by surface acoustic waves *Phys. Rev. Lett.* **113** 118102

[123] Foerster M *et al* 2017 Direct imaging of delayed magneto-dynamic modes induced by surface acoustic waves *Nat. Commun.* **8** 407

[124] Kapfinger S, Reichert T, Lichtmannecker S, Müller K, Finley J J, Wixforth A, Kaniber M and Krenner H J 2015 Dynamic acousto-optic control of a strongly coupled photonic molecule *Nat. Commun.* **6** 8540

[125] Couto O D D, Lazić S, Iikawa F, Stotz J A H, Jahn U, Hey R and Santos P V 2009 Photon anti-bunching in acoustically pumped quantum dots *Nat. Photonics* **3** 645–8

[126] Weiß M, Kapfinger S, Reichert T, Finley J J, Wixforth A, Kaniber M and Krenner H J 2016 Surface acoustic wave regulated single photon emission from a coupled quantum dot–nanocavity system *Appl. Phys. Lett.* **109** 033105

[127] Sogawa T, Sanada H, Gotoh H, Yamaguchi H, Miyashita S and Santos P V 2009 Spatial and temporal modulation of exciton photoluminescence properties in GaAs/AlAs dynamic quantum dots formed by surface acoustic waves *Phys. Rev.* B **80** 075304

[128] Gell J R, Ward M B, Young R J, Stevenson R M, Atkinson P, Anderson D, Jones G A C, Ritchie D A and Shields A J 2008 Modulation of single quantum dot energy levels by a surface-acoustic-wave *Appl. Phys. Lett.* **93** 81115

[129] Metcalfe M, Carr S M, Muller A, Solomon G S and Lawall J 2010 Resolved sideband emission of InAs/GaAs quantum dots strained by surface acoustic waves *Phys. Rev. Lett.* **105** 37401

[130] Kinzel J B, Rudolph D, Bichler M, Abstreiter G, Finley J J, Koblmüller G, Wixforth A and Krenner H J 2011 Directional and dynamic modulation of the optical emission of an individual GaAs nanowire using surface acoustic waves *Nano Lett.* **11** 1512–7

[131] Lazić S, Chernysheva E, Gačević Ž, van der Meulen H P, Calleja E and Calleja Pardo J M 2015 Dynamic control of the optical emission from GaN/InGaN nanowire quantum dots by surface acoustic waves *AIP Adv.* **5** 097217

[132] Villa B *et al* 2017 Surface acoustic wave modulation of a coherently driven quantum dot in a pillar microcavity *Appl. Phys. Lett.* **111** 011103

[133] Shilton J M, Talyanskii V I, Pepper M, Ritchie D A, Frost J E F, Ford C J B, Smith C G and Jones G A C 1996

High-frequency single-electron transport in a quasi-one-dimensional GaAs channel induced by surface acoustic waves *J. Phys.: Condens. Matter* **8** L531–9
[134] Talyanskii V, Shilton J, Pepper M, Smith C, Ford C, Linfield E, Ritchie D and Jones G 1997 Single-electron transport in a one-dimensional channel by high-frequency surface acoustic waves *Phys. Rev.* B **56** 15180–4
[135] Rocke C, Zimmermann S, Wixforth A, Kotthaus J P, Böhm G and Weimann G 1997 Acoustically driven storage of light in a quantum well *Phys. Rev. Lett.* **78** 4099–102
[136] Rocke C, Govorov A O, Wixforth A, Böhm G and Weimann G 1998 Exciton ionization in a quantum well studied by surface acoustic waves *Phys. Rev.* B **57** R6850–3
[137] Alsina F, Santos P V, Hey R, García-Cristóbal A and Cantarero A 2001 Dynamic carrier distribution in quantum wells modulated by surface acoustic waves *Phys. Rev.* B **64** 041304
[138] Alsina F, Santos P V, Schönherr H-P, Nötzel R and Ploog K H 2003 Real-time dynamics of the acoustically induced carrier transport in GaAs quantum wires *Phys. Rev.* B **67** 161305
[139] García-Cristóbal A, Cantarero A, Alsina F and Santos P V 2004 Spatiotemporal carrier dynamics in quantum wells under surface acoustic waves *Phys. Rev.* B **69** 205301
[140] Santos P V, Alsina F, Stotz J A H, Hey R, Eshlaghi S and Wieck A D 2004 Band mixing and ambipolar transport by surface acoustic waves in GaAs quantum wells *Phys. Rev.* B **69** 155318
[141] Wiele C, Haake F, Rocke C and Wixforth A 1998 Photon trains and lasing: the periodically pumped quantum dot *Phys. Rev.* A **58** R2680–3
[142] Michler P, Imamoğlu A, Mason M, Carson P, Strouse G and Buratto S 2000 Quantum correlation among photons from a single quantum dot at room temperature *Nature* **406** 968–70
[143] Völk S, Schülein F J R, Knall F, Reuter D, Wieck A D, Truong T A, Kim H, Petroff P M, Wixforth A and Krenner H J 2010 Enhanced sequential carrier capture into individual quantum dots and quantum posts controlled by surface acoustic waves *Nano Lett.* **10** 3399–407
[144] Goldstein L, Glas F, Marzin J Y, Charasse M N and Le Roux G 1985 Growth by molecular beam epitaxy and characterization of InAs/GaAs strained-layer superlattices *Appl. Phys. Lett.* **47** 1099–101
[145] He J, Krenner H J, Pryor C, Zhang J P, Wu Y, Allen D G, Morris C M, Sherwin M S and Petroff P M 2007 Growth, structural, and optical properties of self-assembled (In,Ga) As quantum posts on GaAs *Nano Lett.* **7** 802–6
[146] Li L H, Patriarche G, Rossetti M and Fiore A 2007 Growth and characterization of InAs columnar quantum dots on GaAs substrate *J. Appl. Phys.* **102** 033502
[147] Krenner H J, Pryor C E, He J and Petroff P M 2008 A semiconductor exciton memory cell based on a single quantum nanostructure *Nano Lett.* **8** 1750–5
[148] Krenner H J and Petroff P M 2009 Quantum posts with tailored structural, electronic and optical properties for optoelectronic and quantum electronic device applications *Solid State Commun.* **149** 1386–94
[149] Brunner K, Abstreiter G, Böhm G, Tränkle G and Weimann G 1994 Sharp-line photoluminescence and two-photon absorption of zero-dimensional biexcitons in a GaAs/AlGaAs structure *Phys. Rev. Lett.* **73** 1138–41
[150] Gammon D, Snow E, Shanabrook B, Katzer D and Park D 1996 Homogeneous linewidths in the optical spectrum of a single gallium arsenide quantum dot *Science* **273** 87–90
[151] Nötzel R, Niu Z, Ramsteiner M, Schönherr H-P, Tranpert A, Däweritz L and Ploog K H 1998 Uniform quantum-dot arrays formed by natural self-faceting on patterned substrates *Nature* **392** 56–9
[152] Sopanen M, Lipsanen H and Ahopelto J 1995 Strain-induced quantum dots by self-organized stressors *Appl. Phys. Lett.* **66** 2364–6
[153] Bödefeld C, Ebbecke J, Toivonen J, Sopanen M, Lipsanen H and Wixforth A 2006 Experimental investigation towards a periodically pumped single-photon source *Phys. Rev.* B **74** 035407
[154] Kinzel J B *et al* 2016 The native material limit of electron and hole mobilities in semiconductor nanowires *ACS Nano* **10** 4942–53
[155] Sakaki H, Noda T, Hirakawa K, Tanaka M and Matsusue T 1987 Interface roughness scattering in GaAs/AlAs quantum wells *Appl. Phys. Lett.* **51** 1934–6
[156] Babiński A, Borysiuk J, Kret S, Czyż M, Golnik A, Raymond S and Wasilewski Z R 2008 Natural quantum dots in the InAs/GaAs wetting layer *Appl. Phys. Lett.* **92** 171104
[157] Krenner H J, Völk S, Schülein F J R, Knall F, Wixforth A, Reuter D, Wieck A D, Kim H, Truong T A and Petroff P M 2012 Surface acoustic wave controlled carrier injection into self-assembled quantum dots and quantum posts *Phys. Status Solidi* c **9** 407–10
[158] Dekel E, Regelman D V, Gershoni D, Ehrenfreund E, Schoenfeld W V and Petroff P M 2000 Cascade evolution and radiative recombination of quantum dot multiexcitons studied by time-resolved spectroscopy *Phys. Rev.* B **62** 11038–45
[159] Moreau E, Robert I, Manin L, Thierry-Mieg V, Gérard J M and Abram I 2001 Quantum cascade of photons in semiconductor quantum dots *Phys. Rev. Lett.* **87** 183601
[160] Schülein F J R, Laucht A, Riikonen J, Mattila M, Sopanen M, Lipsanen H, Finley J J, Wixforth A and Krenner H J 2009 Cascaded exciton emission of an individual strain-induced quantum dot *Appl. Phys. Lett.* **95** 83122
[161] Schülein F J R, Müller K, Bichler M, Koblmüller G, Finley J J, Wixforth A and Krenner H J 2013 Acoustically regulated carrier injection into a single optically active quantum dot *Phys. Rev.* B **88** 085307
[162] Schülein F J R, Pustiowski J, Müller K, Bichler M, Koblmüller G, Finley J J, Wixforth A and Krenner H J 2012 Surface acoustic wave controlled charge dynamics in a thin InGaAs quantum well *JETP Lett.* **95** 575–80
[163] Lazić S, Hey R and Santos P V 2012 Mechanism of non-classical light emission from acoustically populated (3 1 1) A GaAs quantum wires *New J. Phys.* **14** 013005
[164] Hernández-Mínguez A *et al* 2012 Acoustically driven photon antibunching in nanowires *Nano Lett.* **12** 252–8
[165] Völk S, Knall F, Schülein F J R, Truong T A, Kim H, Petroff P M, Wixforth A and Krenner H J 2012 Surface acoustic wave mediated carrier injection into individual quantum post nano emitters *Nanotechnology* **23** 285201
[166] Pollak F H and Cardona M 1968 Piezo-electroreflectance in Ge, GaAs, and Si *Phys. Rev.* **172** 816–37
[167] Pustiowski J, Müller K, Bichler M, Koblmüller G, Finley J J, Wixforth A and Krenner H J 2015 Independent dynamic acousto-mechanical and electrostatic control of individual quantum dots in a $LiNbO_3$-GaAs hybrid *Appl. Phys. Lett.* **106** 013107
[168] Kaniber M, Huck M F, Müller K, Clark E C, Troiani F, Bichler M, Krenner H J and Finley J J 2011 Electrical control of the exciton–biexciton splitting in self-assembled InGaAs quantum dots *Nanotechnology* **22** 325202
[169] Weiß M *et al* 2014 Dynamic acoustic control of individual optically active quantum dot-like emission centers in heterostructure nanowires *Nano Lett.* **14** 2256–64

[170] Nysten E D S, Huo Y H, Yu H, Song G F, Rastelli A and Krenner H J 2017 Multi-harmonic quantum dot optomechanics in fused $LiNbO_3$-(Al)GaAs hybrids *J. Phys. D: Appl. Phys.* **50** 43LT01

[171] Matthiesen C, Vamivakas A N and Atatüre M 2012 Subnatural linewidth single photons from a quantum dot *Phys. Rev. Lett.* **108** 093602

[172] Aspelmeyer M, Kippenberg T J and Marquardt F 2014 Cavity optomechanics *Rev. Mod. Phys.* **86** 1391–452

[173] Schülein F J R, Zallo E, Atkinson P, Schmidt O G, Trotta R, Rastelli A, Wixforth A and Krenner H J 2015 Fourier synthesis of radiofrequency nanomechanical pulses with different shapes *Nat. Nanotechnol.* **10** 512–6

[174] Yablonovitch E, Gmitter T, Harbison J P and Bhat R 1987 Extreme selectivity in the lift-off of epitaxial GaAs films *Appl. Phys. Lett.* **51** 2222

[175] Yablonovitch E, Hwang D M, Gmitter T J, Florez L T and Harbison J P 1990 Van der Waals bonding of GaAs epitaxial liftoff films onto arbitrary substrates *Appl. Phys. Lett.* **56** 2419

[176] Hohkawa K, Suzuki H, Huang Q S and Noge S 1995 Fabrication of surface acoustic wave semiconductor coupled devices using epitaxial lift-off technology GaAs-$LiNbO_3$ structure *1995 IEEE Ultrasonics Symp. Proc. Int. Symp.* vol 1 (Piscataway, NJ: IEEE) pp 401–4

[177] Rotter M, Rocke C, Böhm S, Lorke A, Wixforth A, Ruile W and Korte L 1997 Single-chip fused hybrids for acousto-electric and acousto-optic applications *Appl. Phys. Lett.* **70** 2097–9

[178] Rotter M, Wixforth A, Ruile W, Bernklau D and Riechert H 1998 Giant acoustoelectric effect in GaAs/$LiNbO_3$ hybrids *Appl. Phys. Lett.* **73** 2128–30

[179] Rotter M, Kalameitsev A V, Govorov A O, Ruile W and Wixforth A 1999 Charge conveyance and nonlinear acoustoelectric phenomena for intense surface acoustic waves on a semiconductor quantum well *Phys. Rev. Lett.* **82** 2171–4

[180] Fuhrmann D A, Wixforth A, Curran A, Morrod J K, Prior K A, Warburton R J and Ebbecke J 2009 Surface acoustic wave mediated exciton dissociation in a ZnCdSe/$LiNbO_3$ hybrid *Appl. Phys. Lett.* **94** 193505

[181] Fuhrmann D A, Krenner H J, Wixforth A, Curran A, Prior K A, Warburton R J and Ebbecke J 2010 Noninvasive probing of persistent conductivity in high quality ZnCdSe/ZnSe quantum wells using surface acoustic waves *J. Appl. Phys.* **107** 093717

[182] Yablonovitch E, Sands T, Hwang D M, Schnitzer I, Gmitter T J, Shastry S K, Hill D S and Fan J C C 1991 Van der Waals bonding of GaAs on Pd leads to a permanent, solid-phase-topotaxial, metallurgical bond *Appl. Phys. Lett.* **59** 3159

[183] Heiss D, Jovanov V, Caesar M, Bichler M, Abstreiter G and Finley J J 2009 Selective optical charge generation, storage, and readout in a single self-assembled quantum dot *Appl. Phys. Lett.* **94** 72108

[184] Ramsay A J, Boyle S J, Kolodka R S, Oliveira J B B, Skiba-Szymanska J, Liu H Y, Hopkinson M, Fox A M and Skolnick M S 2008 Fast optical preparation, control, and readout of a single quantum dot spin *Phys. Rev. Lett.* **100** 197401

[185] Michaelis de Vasconcellos S, Gordon S, Bichler M, Meier T and Zrenner A 2010 Coherent control of a single exciton qubit by optoelectronic manipulation *Nat. Photonics* **4** 545–8

[186] Müller K *et al* 2012 Electrical control of interdot electron tunneling in a double InGaAs quantum-dot nanostructure *Phys. Rev. Lett.* **108** 197402

[187] Ebbecke J, Maisch S, Wixforth A, Calarco R, Meijers R, Marso M and Lüth H 2008 Acoustic charge transport in GaN nanowires *Nanotechnology* **19** 275708

[188] Roddaro S, Strambini E, Romeo L, Piazza V, Nilsson K, Samuelson L and Beltram F 2010 Charge pumping in InAs nanowires by surface acoustic waves *Semicond. Sci. Technol.* **25** 24013

[189] Büyükköse S, Hernández-Mínguez A, Vratzov B, Somaschini C, Geelhaar L, Riechert H, van der Wiel W G and Santos P V 2014 High-frequency acoustic charge transport in GaAs nanowires *Nanotechnology* **25** 135204

[190] Weiß M *et al* 2014 Radio frequency occupancy state control of a single nanowire quantum dot *J. Phys. D: Appl. Phys.* **47** 394011

[191] Hess H F, Betzig E, Harris T D, Pfeiffer L N and West K W 1994 Near-field spectroscopy of the quantum constituents of a luminescent system *Science* **264** 1740–5

[192] Bracker A *et al* 2005 Binding energies of positive and negative trions: from quantum wells to quantum dots *Phys. Rev.* B **72** 035332

[193] Lazić S, Chernysheva E, Hernández-Mínguez A, Santos P V and van der Meulen H P 2018 Acoustically regulated optical emission dynamics from quantum dot-like emission centers in GaN/InGaN nanowire heterostructures *J. Phys. D: Appl. Phys.* **51** 104001

[194] Demichel O, Heiss M, Bleuse J, Mariette H and i Morral A F 2010 Impact of surfaces on the optical properties of GaAs nanowires *Appl. Phys. Lett.* **97** 201907

[195] Mancini L *et al* 2014 Three-dimensional nanoscale study of Al segregation and quantum dot formation in GaAs/AlGaAs core-shell nanowires *Appl. Phys. Lett.* **105** 243106

[196] Jeon N, Loitsch B, Morkoetter S, Abstreiter G, Finley J, Krenner H J, Koblmueller G and Lauhon L J 2015 Alloy fluctuations act as quantum dot-like emitters in GaAs-AlGaAs core–shell nanowires *ACS Nano* **9** 8335–43

[197] Miller D A B, Chemla D S, Damen T C, Gossard A C, Wiegmann W, Wood T H and Burrus C A 1984 Band-edge electroabsorption in quantum well structures: the quantum-confined stark effect *Phys. Rev. Lett.* **53** 2173–6

[198] Schuegraf K F, King C C and Hu C 1992 Ultra-thin silicon dioxide leakage current and scaling limit *1992 Symp. on VLSI Technology Digest of Technical Papers* (Piscataway, NJ: IEEE) pp 18–9

[199] Heiss M *et al* 2013 Self-assembled quantum dots in a nanowire system for quantum photonics *Nat. Mater.* **12** 439–44

[200] Fox M 2006 *Quantum Optics* (Oxford: Oxford University Press)

[201] Vahala K J 2003 Optical microcavities *Nature* **424** 839–46

[202] Kiraz A, Michler P, Becher C, Gayral B, Imamoglu A, Zhang L, Hu E, Schoenfeld W V and Petroff P M 2001 Cavity-quantum electrodynamics using a single InAs quantum dot in a microdisk structure *Appl. Phys. Lett.* **78** 3932–4

[203] Santori C, Pelton M, Solomon G, Dale Y and Yamamoto Y 2001 Triggered single photons from a quantum dot *Phys. Rev. Lett.* **86** 1502–5

[204] Bayer M, Reinecke T L, Weidner F, Larionov A, McDonald A and Forchel A 2001 Inhibition and enhancement of the spontaneous emission of quantum dots in structured microresonators *Phys. Rev. Lett.* **86** 3168–71

[205] Strauf S, Stoltz N G, Rakher M T, Coldren L A, Petroff P M and Bouwmeester D 2007 High-frequency single-photon source with polarization control *Nat. Photonics* **1** 704–8

[206] Kress A, Hofbauer F, Reinelt N, Kaniber M, Krenner H, Meyer R, Böhm G and Finley J 2005 Manipulation of the spontaneous emission dynamics of quantum dots in two-dimensional photonic crystals *Phys. Rev.* B **71** 241304

[207] Chang W-H, Chen W-Y, Chang H-S, Hsieh T-P, Chyi J-I and Hsu T-M 2006 Efficient single-photon sources based on

low-density quantum dots in photonic-crystal nanocavities *Phys. Rev. Lett.* **96** 117401
[208] Aoki K, Guimard D, Nishioka M, Nomura M, Iwamoto S and Arakawa Y 2008 Coupling of quantum-dot light emission with a three-dimensional photonic-crystal nanocavity *Nat. Photonics* **2** 688–92
[209] Peter E, Senellart P, Martrou D, Lemaître A, Hours J, Gérard J M and Bloch J 2005 Exciton–photon strong-coupling regime for a single quantum dot embedded in a microcavity *Phys. Rev. Lett.* **95** 067401
[210] Srinivasan K and Painter O 2007 Linear and nonlinear optical spectroscopy of a strongly coupled microdisk-quantum dot system *Nature* **450** 862–5
[211] Englund D, Faraon A, Fushman I, Stoltz N, Petroff P and Vuckovic J 2007 Controlling cavity reflectivity with a single quantum dot *Nature* **450** 857–61
[212] Fischer K A, Müller K, Rundquist A, Sarmiento T, Piggott A Y, Kelaita Y, Dory C, Lagoudakis K G and Vučković J 2016 Self-homodyne measurement of a dynamic Mollow triplet in the solid state *Nat. Photonics* **10** 163–6
[213] Notomi M, Shinya A, Mitsugi S, Kuramochi E and Ryu H-Y 2004 Waveguides, resonators and their coupled elements in photonic crystal slabs *Opt. Express* **12** 1551
[214] Akahane Y, Asano T, Song B-S and Noda S 2003 High-Q photonic nanocavity in a two-dimensional photonic crystal *Nature* **425** 944–7
[215] Tadesse S A, Li H, Liu Q and Li M 2015 Acousto-optic modulation of a photonic crystal nanocavity with Lamb waves in microwave K band *Appl. Phys. Lett.* **107** 201113
[216] Li H, Tadesse S A, Liu Q and Li M 2015 Nanophotonic cavity optomechanics with propagating acoustic waves at frequencies up to 12 GHz *Optica* **2** 826
[217] Winger M *et al* 2009 Explanation of photon correlations in the far-off-resonance optical emission from a quantum-dot–cavity system *Phys. Rev. Lett.* **103** 207403
[218] Hohenester U 2010 Cavity quantum electrodynamics with semiconductor quantum dots: role of phonon-assisted cavity feeding *Phys. Rev.* B **81** 155303
[219] Florian M, Gartner P, Gies C and Jahnke F 2013 Phonon-mediated off-resonant coupling effects in semiconductor quantum-dot lasers *New J. Phys.* **15** 035019
[220] Florian M, Gartner P, Steinhoff A, Gies C and Jahnke F 2014 Coulomb-assisted cavity feeding in nonresonant optical emission from a quantum dot *Phys. Rev.* B **89** 161302
[221] Jaynes E T and Cummings F W 1963 Comparison of quantum and semiclassical radiation theories with application to the beam maser *Proc. IEEE* **51** 89–109
[222] Thon S M, Rakher M T, Kim H, Gudat J, Irvine W T M, Petroff P M and Bouwmeester D 2009 Strong coupling through optical positioning of a quantum dot in a photonic crystal cavity *Appl. Phys. Lett.* **94** 111115
[223] Laucht A, Hofbauer F, Hauke N, Angele J, Stobbe S, Kaniber M, Böhm G, Lodahl P, Amann M and Finley J J 2009 Electrical control of spontaneous emission and strong coupling for a single quantum dot *New J. Phys.* **11** 023034
[224] Blattmann R, Krenner H J, Kohler S and Hänggi P 2014 Entanglement creation in a quantum-dot–nanocavity system by Fourier-synthesized acoustic pulses *Phys. Rev.* A **89** 012327
[225] Landau L D 1932 Zur Theorie der Energieübertragung bei Stössen II *Phys. Z. Sowjetunion* **2** 46–51
[226] Zener C 1932 Non-adiabatic crossing of energy levels *Proc. R. Soc.* A **137** 696–702
[227] Stückelberg E C G 1932 Theorie der unelastischen Stösse zwischen Atomen *Helv. Phys. Acta* **5** 369
[228] Majorana E 1932 Atomi orientati in campo magnetico variabile *Nuovo Cim.* **9** 43–50
[229] Saito K, Wubs M, Kohler S, Hänggi P and Kayanuma Y 2006 Quantum state preparation in circuit QED via Landau–Zener tunneling *Europhys. Lett.* **76** 22–8
[230] Nomura M, Kumagai N, Iwamoto S, Ota Y and Arakawa Y 2010 Laser oscillation in a strongly coupled single-quantum-dot–nanocavity system *Nat. Phys.* **6** 279–83
[231] Eichenfield M, Chan J, Camacho R M, Vahala K J and Painter O 2009 Optomechanical crystals *Nature* **462** 78–82
[232] Pennec Y, Djafari Rouhani B, El Boudouti E H, Li C, El Hassouani Y, Vasseur J O, Papanikolaou N, Benchabane S, Laude V and Martinez A 2010 Simultaneous existence of phononic and photonic band gaps in periodic crystal slabs *Opt. Express* **18** 14301–10
[233] Chan J, Alegre T P M, Safavi-Naeini A H, Hill J T, Krause A, Gröblacher S, Aspelmeyer M and Painter O 2011 Laser cooling of a nanomechanical oscillator into its quantum ground state *Nature* **478** 89–92
[234] Psarobas I E, Papanikolaou N, Stefanou N, Djafari-Rouhani B, Bonello B and Laude V 2010 Enhanced acousto-optic interactions in a one-dimensional phoxonic cavity *Phys. Rev.* B **82** 174303
[235] Gomis-Bresco J *et al* 2014 A one-dimensional optomechanical crystal with a complete phononic band gap *Nat. Commun.* **5** 2441
[236] Riedinger R, Hong S, Norte R A, Slater J A, Shang J, Krause A G, Anant V, Aspelmeyer M and Gröblacher S 2016 Non-classical correlations between single photons and phonons from a mechanical oscillator *Nature* **530** 313–6
[237] Hong S, Riedinger R, Marinković I, Wallucks A, Hofer S G, Norte R A, Aspelmeyer M and Gröblacher S 2017 Hanbury Brown and Twiss interferometry of single phonons from an optomechanical resonator *Science* **358** 203–6
[238] Balram K C, Davanço M I, Song J D and Srinivasan K 2016 Coherent coupling between radiofrequency, optical and acoustic waves in piezo-optomechanical circuits *Nat. Photonics* **10** 346–52
[239] Balram K C, Davanço M I, Ilic B R, Kyhm J-H, Song J D and Srinivasan K 2017 Acousto-optic modulation and optoacoustic gating in piezo-optomechanical circuits *Phys. Rev. Appl.* **7** 024008
[240] Restrepo J, Ciuti C and Favero I 2014 Single-polariton optomechanics *Phys. Rev. Lett.* **112** 013601
[241] Restrepo J, Favero I and Ciuti C 2017 Fully coupled hybrid cavity optomechanics: quantum interferences and correlations *Phys. Rev.* A **95** 023832
[242] Volz S *et al* 2016 Nanophononics: state of the art and perspectives *Eur. Phys. J.* B **89** 15
[243] Wilson-Rae I, Zoller P and Imamoğlu A 2004 Laser cooling of a nanomechanical resonator mode to its quantum ground state *Phys. Rev. Lett.* **92** 075507
[244] Midolo L, Schliesser A and Fiore A 2018 Nano-opto-electro-mechanical systems *Nat. Nanotechnol.* **13** 11–8
[245] Bolgar A N, Zotova J I, Kirichenko D D, Besedin I S, Semenov A V, Shaikhaidarov R S and Astafiev O V 2017 Experimental demonstration of a two-dimensional phonon cavity in the quantum regime *Phys. Rev. Lett.* **120** 223603
[246] Moores B A, Sletten L R, Viennot J J and Lehnert K W 2017 Cavity quantum acoustic device in the multimode strong coupling regime *Phys. Rev. Lett.* **120** 227701
[247] Satzinger K J *et al* 2018 Quantum control of surface acoustic wave phonons (arXiv:1804.07308)
[248] Whiteley S J *et al* 2018 Coherent control of spins with Gaussian acoustics (arXiv:1804.10996)